SEISMOGRAM SYNTHESIS IN COMPLEX BOREHOLES WITH APPLICATION TO ATTENUATION ESTIMATION

A DISSERTATION
SUBMITTED TO THE DEPARTMENT OF GEOPHYSICS
AND THE COMMITTEE ON GRADUATE STUDIES
OF STANFORD UNIVERSITY
IN PARTIAL FULFILLMENT OF THE REQUIREMENTS
FOR THE DEGREE OF
DOCTOR OF PHILOSOPHY

Youli Quan

November 1996

(*This file was restored in 2009 from original Mac Word files. Some of the figures and equations could not be recovered correctly.*)

I certify that I have read this dissertation and that in my opinion it is fully adequate, in scope and quality, as a dissertation for the degree of Doctor of Philosophy.

Jerry M. Harris (Principal Adviser)

I certify that I have read this dissertation and that in my opinion it is fully adequate, in scope and quality, as a dissertation for the degree of Doctor of Philosophy.

Norman H. Sleep

I certify that I have read this dissertation and that in my opinion it is fully adequate, in scope and quality, as a dissertation for the degree of Doctor of Philosophy.

Gregory C. Beroza

I certify that I have read this dissertation and that in my opinion it is fully adequate, in scope and quality, as a dissertation for the degree of Doctor of Philosophy.

Daniel Moos

Approved for the University Committee on Graduate Studies:

ABSTRACT

Borehole related seismic measurements, such as acoustic logging, vertical seismic profiling, crosswell profiling, and single borehole profiling, provide high resolution data which are useful for reservoir characterization and locating new well sites. Study of elastic waves in boreholes is important for understanding and interpreting these borehole seismic data. Real boreholes are usually embedded in a layered formation, and may also have near borehole alterations, e.g., casing, cement, and invaded zones. In this thesis, two new semi-analytical approaches using the generalized reflection/transmission matrices method are developed to simulate these complicated boreholes. The first method simulates boreholes with radial layers; the second method deals with more realistic boreholes which have radial multi-layers with vertical variations in each layer.

Because of their efficiency, stability, and accuracy, these new approaches have many applications to borehole seismic problems. In this thesis, I apply them to the estimation of seismic attenuation from borehole data. Attenuation is important for the characterization of rock properties, e.g., porosity, permeability, saturation, and pore fluid viscosity. Measurements of both velocity and attenuation provide complementary information about rock properties. I propose a new method for estimating seismic attenuation based on frequency shift data. In comparison to many other methods of estimating attenuation, the frequency shift method is relatively insensitive to reflection and transmission effects, source and receiver coupling and radiation patterns, and instrument responses. In the frequency shift method, wave dispersion is used as the observed signal for the attenuation estimation. If we use purely numerical methods of simulation, grid dispersion could cause errors. The semi-analytical approaches

developed in this thesis do not have grid dispersion, and are appropriate for this attenuation study.

To show the validity and applicability, the modeling approaches are used to create synthetic data for a variety of complicated borehole models. The frequency shift method is applied to the synthetic data for attenuation tomography and attenuation logging. The synthetic study reveals the geometrical spreading property of waves in complicated boreholes. Field data examples are also presented. The results show that the estimated attenuation distribution has good correlation with the lithology.

ACKNOWLEDGMENTS

First, I wish to express my sincere gratitude to my advisor, Jerry Harris. His support, inspiration and stimulating advice are major factors for the successful completion of this dissertation. Jerry is always available for discussions. His physical insight and numerous interesting ideas makes the discussions fruitful and enjoyable. Jerry not only emphasizes theoretical research, but also encourages us make efforts to applied research.

I also wish to express my appreciation to Kiyoshi Yomogida. It was his help that made my study at Stanford University possible. Even after Kiyoshi left Stanford, he still gave me many useful suggestions on my work.

Special thanks to Xiaofei Chen of University of Southern California, my friend and college classmate. During last a few years, close cooperation between us led to several papers published regarding to the borehole wave simulation. Xiaofei provided extremely valuable help on the development of the wave propagation theory. Nick Smalley was my office-mate. Daily conversation between us gave the office life much pleasure. Nick edited many papers of mine. My attenuation tomography program was modified from a velocity tomography code originally written by Feng Yin. Feng gave me many help on the attenuation work. Thanks to Mark Van Schaack for the work he did on the computer system management and field data editing.

Dan Moos gave me many suggestions on sonic logging and wave modeling. Dan very carefully reviewed my dissertation and explained all comments to me in person. I also would like to thank Norm Sleep and Greg Beroza for reading this thesis. I had many discussions with Gary Mavko when I started to work on the attenuation project. He gave many stimulating suggestions.

Finally, I would like to thank my wife, Li, my daughter, Cindy, and my parents for their support. Without their support and encouragement, it would have been impossible to finish this dissertation.

Contents

List of Figures

List of Tables

Chapter 1

Introduction

Surface seismic surveys are extensively used for petroleum exploration and development. When wells are drilled, however, measurements in wells provide detailed information on the structure of the targeted reservoir. Acoustic logging, vertical seismic profiling (VSP), crosswell profiling, and single borehole profiling are examples of seismic measurements made from within the borehole. Acoustic logging and single borehole profiling have both sources and receivers in one borehole and measure rock properties around the borehole. Crosswell profiling has sources in one borehole and receivers in another borehole, and measures rock properties between boreholes. VSP places the sources on the surface and the receivers in a borehole, or *vice versa*. Borehole measurements eliminate the problem of high absorption near the earth's surface (in VSP the wave goes through the absorptive soil once). Therefore, it is possible to use high frequency sources to create high resolution seismograms which are very useful for reservoir characterization and locating new well sites.

When performing borehole measurements, we must consider the borehole effects on the seismic waves. Study of acoustic waves in boreholes is important for understanding and interpreting the borehole seismic data. Waves in a borehole are complicated. In acoustic logging, the direct *P* and *S* waves propagate along the borehole wall, while Stoneley and pseudo Rayleigh waves propagate within the borehole.

Seismogram synthesis can help us understand the properties of these waves and their relationship to the properties of the medium.

This thesis consists of two main parts: (a) elastic wave simulations in complicated boreholes using the method of generalized reflection/transmission matrices; (b) seismic attenuation estimation from crosswell profiling and acoustic logging based on the centroid frequency shift method and the normal mode method. These two parts are related. The motivation of the wave simulation is from the seismic attenuation study. The centroid frequency shift method proposed in this thesis is a new approach to seismic attenuation estimation. I need to do numerical simulations to analyze the problems arising from this new approach. I have developed two semi-analytical methods in this thesis for modeling the complete wave fields in two types of complicated boreholes.

In the real world, all kinds of rocks are absorptive media. When elastic waves propagate in the absorptive media, some wave energy is converted into heat. The attenuation coefficient is an important parameter to describe this absorption feature. Measurements of both attenuation coefficient and velocity provide complementary information for characterization of rock properties. Though the attenuation coefficient is very useful, its measurement is much more difficult than the wave velocity. Many efforts have been made to improve the attenuation measurement. In this thesis, I propose a new method for estimating attenuation based on the centroid frequency shift of a wave spectrum. In the frequency shift method, wave dispersion is used as the observed signal for the attenuation estimation. Compared with many other attenuation estimation methods, the frequency shift method is more robust especially for field data.

When we do simulation for the frequency shift method that uses the wave dispersion information as the signal, we have special requirements for the modeling techniques. The numerical modeling approaches to complex media, e.g., the finite difference and finite element methods, need to discretize a model into grids. The discretization can introduce grid dispersion which is a serious numerical error for the attenuation estimation. The semi-analytical approaches are suitable for this attenuation study, because there is no model discretization required. For these semi-analytical approaches, however, a model has to be radially symmetric.

Chapters 2 and 3 constitute wave modeling theory and implementation. In Chapter 2, boreholes that can be modeled as multi-layered media are studied. Chapter 3 deals with more complicated boreholes, which are composed of radially layered media with vertical variations. Chapters 4 – 6 constitute attenuation estimation theory and implementation. Chapter 4 introduces the concept of the centroid frequency shift, the way to use it for seismic attenuation estimation, and the application to crosswell attenuation tomography for real and synthetic data. Chapter 5 studies the acoustic attenuation logging based on the centroid frequency shift method. In Chapter 6, I explore the possibility of using tube waves for seismic attenuation estimation.

1.1 ACOUSTIC SIMULATION FOR COMPLICATED BOREHOLES

An open borehole is usually modeled as a simple fluid-filled cylinder embedded in a homogenous formation (e.g., Biot, 1952; White, 1962; Tsang and Rader, 1979; Cheng and Toksöz, 1981). More complicated boreholes, for example, simulating casing and invaded zones, are modeled as radially multi-layered media (see Figure 1.1). Tubman et al. (1984) and Baker (1984) used the Thomson-Haskell method to simulate these radially multi-layered media. If the formation becomes heterogeneous and the borehole has washouts, finite difference and finite element methods can be used to numerically calculate the wave fields (e.g., Stephen et al., 1985; Randall et al. 1991). The grid dispersion and inaccurate handling of the fluid-solid interface are problems with the accuracy of these numerical techniques. Moreover, if we consider the wave field at large distances in the formation, the scale difference between the small borehole diameter and the large formation extent also cause numerical difficulties, e.g., huge memory is then required for the numerical computation. If the heterogeneity of a borehole model exhibits certain symmetric features, analytical or semi-analytical approaches can be employed to simulate the wave propagation. Bouchon (1993) and Dong et al. (1995) used a boundary element-based technique for open and cased boreholes embedded in layered media. In this approach, we need to discretize the borehole wall. It can deal with reasonably complex models and also eliminate the large scale difference problem.

In the modeling part of this thesis (Chapters 2 and 3), the generalized reflection and transmission (R/T) coefficients method is introduced to analytically simulate complicated borehole models. The generalized R/T coefficients method is widely used in modeling the elastic waves in vertically layered media because of its computational stability and efficiency over the Thomson-Haskell method, especially for high frequency problems (see, e.g., Luco & Apsel, 1983; Kennett, 1983; Chen, 1993). In a wave propagation problem, if the characteristic wave-length is much smaller than the characteristic structure dimension (e.g. the thickness of a layer), we consider this to be a high frequency problem. Moreover, the normalized Hankel functions are introduced to further stabilize the numerical computation.

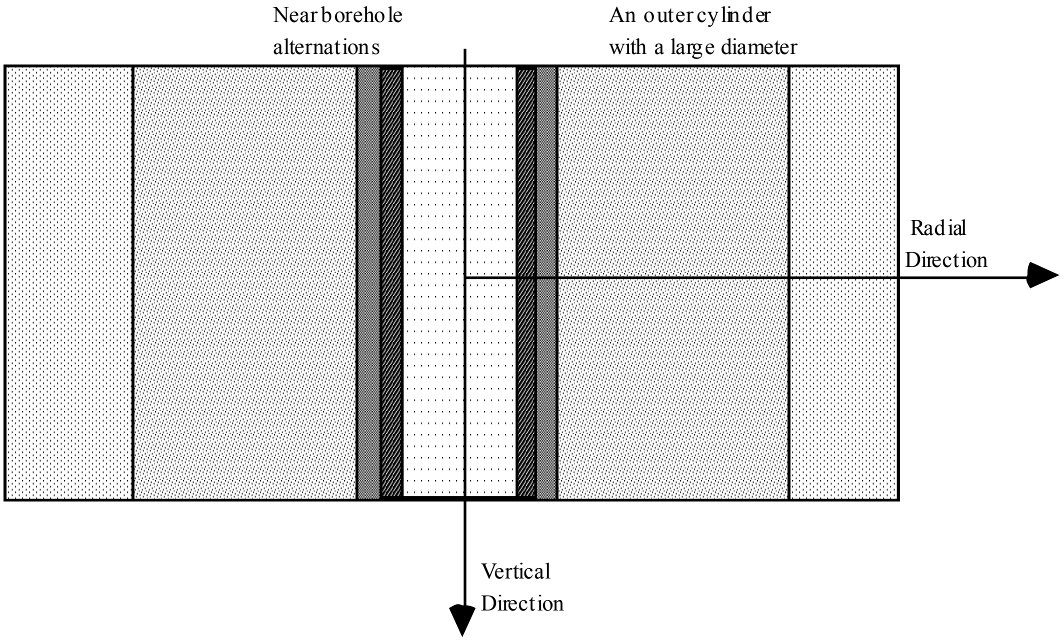

Figure 1.1 A radially layered model.

Chapter 2 introduces the generalized R/T coefficients method to simulate multi-layered media shown in Figure 1.1. The unique feature of this new modeling approach is its stability which makes it possible to simulate the high frequency problem. One example is an outer cylinder with a large diameter in the formation shown in Figure 1.1. This example is useful for single borehole profiling. Chapter 3 applies the generalized R/T coefficients method to the more realistic model shown in Figure 1.2. Although the model becomes complicated, it still exhibits radial symmetry. Taking advantage of this symmetry, a semi-analytical approach is developed. This method can simulate the cased borehole with perforations and the formation with faults, which are more realistic models than those in Bouchon (1993) and Dong et al. (1995). In this approach, we use ω-k integrals, and do not need to discretize the model at all. In this thesis, I applied these modeling techniques to crosswell seismic profiling, full waveform acoustic logging, single borehole profiling, and seismic attenuation estimation.

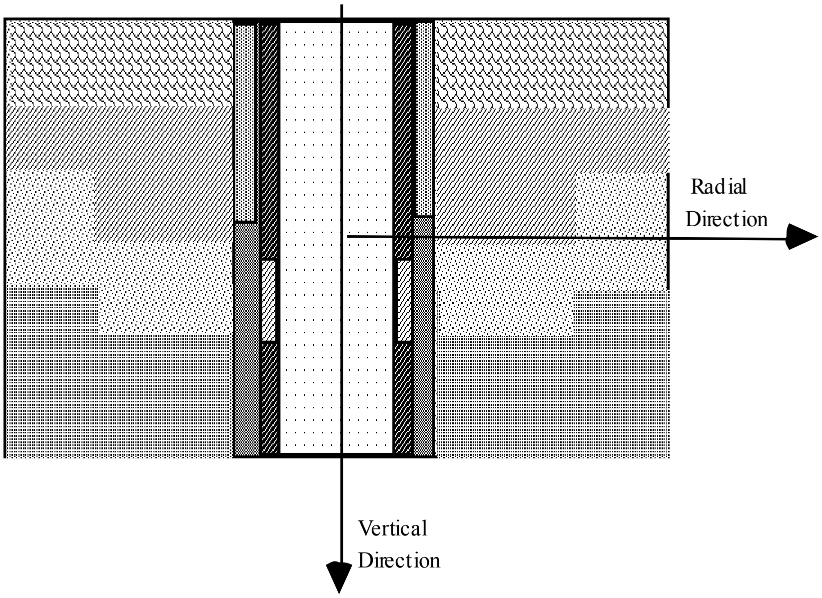

Figure 1.2 A radially layered model with vertical variations in each layer.

1.2 CENTROID FREQUENCY SHIFT AND SEISMIC ATTENUATION TOMOGRAPHY

It has long been believed that attenuation is important for the characterization of rock and fluid properties, e.g., saturation, porosity, permeability and viscosity, because attenuation is more sensitive to some of these rock properties than velocity (see, e.g., Best et al., 1994). Attempts at tomographically estimating attenuation have persisted for years. There are three typical methods used for seismic attenuation estimation: amplitude decay, pulse broadening, and spectral ratio methods (e.g., Toksöz and Johnston, 1981).

The amplitude decay method is simple and direct. However, amplitudes are easily contaminated by many factors such as scattering, geometric spreading, source and receiver coupling, radiation patterns and transmission/reflection losses; therefore, it is very difficult to obtain reliable attenuation estimates from the amplitude decay method. The pulse broadening and spectral ratio methods are more reliable, because they are not sensitive to transmission/reflection losses and far-field geometrical spreading. However, a precise and robust measurement of pulse broadening is difficult for field data, and the spectral ratio method needs a precise reference signal to calculate the ratio (this reference signal may not be available for attenuation tomography). We need to seek other approaches that are more suitable for attenuation estimation, especially for attenuation tomography. Chapter 4 presents a new approach, the centroid frequency shift method, for seismic attenuation estimation.

In most natural materials, the high frequency components of a seismic signal are attenuated more rapidly than the low frequency components as the wave propagates. As a result, the centroid of the signal's spectrum experiences a downshift during propagation. This phenomenon has been observed in VSP data (Hauge, 1981). I have observed the frequency downshift in crosswell data. In general, the frequency shift in crosswell data is greater than the VSP data, because crosswell data have broader frequency band. Under the assumption of a frequency-independent Q model, we can derive a simple formula that relates the frequency shift to the Q-value, showing that the frequency downshift is proportional to a path integral through the attenuation distribution. This relationship is appropriate for tomographic reconstruction of the attenuation distribution. In Chapter 4, I successfully applied the frequency shift method to crosswell attenuation tomography for both synthetic data and field data. The forward modeling method developed in Chapter 3 is used to calculate the synthetic data.

The frequency shift method is applicable in any seismic survey geometry where the signal bandwidth is broad enough and the attenuation is high enough to cause noticeable losses of high frequencies during propagation. Crosswell seismic profiling uses broad band high frequency sources, and therefore is especially suitable for the centroid frequency shift method.

1.3 ACOUSTIC ATTENUATION LOGGING

Many efforts have been made to estimate seismic attenuation from full waveform sonic logs. Existing methods include amplitude decay, spectral ratio, and full waveform inversion (e.g., Cheng, et al., 1982; Paillet and Cheng, 1991, Page 138). Since accuracy and robustness are still problems, the acoustic attenuation logging has not been used in the industry for routine interpretation as of now. More research work is needed. Acoustic full waveform logs seem to be another type of data suitable for applying the frequency shift method to estimate attenuation, because of the high frequency source with relatively broad bandwidth. I have also observed clear frequency shift in acoustic logs. In Chapter 5, I propose the use of the frequency shift method for attenuation estimation from acoustic logs.

In order to understand the attenuation properties of *P* waves in complex boreholes and provide a guide to in situ measurement, I used the generalized reflection and transmission coefficients method (Chapter 2; Chen, et al., 1996) to simulate waves in boreholes. Then, I applied the centroid frequency shift method to synthetic data for the attenuation estimation. After the synthetic test, I also applied the frequency shift method to field data for acoustic attenuation logging.

Geometrical spreading is a very important property of waves. It is also very important for the attenuation estimation. When measuring intrinsic attenuation of the formation, we must correct for the geometrical spreading of the wave. For a monopole source in a simple borehole, the geometrical spreading factor is approximately $1/z$ for the P wave (Roever et al., 1974; Winbow, 1980). However, in general the geometrical spreading factor is frequency-dependent (Paillet and Cheng, p144, 1991; Quan, et al., 1994). In Chapter 5, I propose an empirical formula to describe the frequency-dependent geometrical spreading of the P wave in a borehole. With the forward modeling method developed in Chapter 2, I investigated the effect of complex invaded zones on the frequency-dependent geometrical spreading and attenuation estimation for P waves. I find that the geometrical spreading $1/z$ is not true for boreholes with invaded zones.

It is difficult to estimate S wave attenuation from the direct S wave in acoustic logs. The S wave is immediately followed by tube waves. We may not extract the complete S wave train from a acoustic log. An alternative way, called partition coefficient method (Cheng, et al., 1982), can be used to estimate S wave attenuation from tube waves, or normal modes. The dispersion relation, which gives the phase velocities of normal modes, is very important for studying normal modes in acoustic logging. It has been studied by many authors, e.g., Biot (1952), Cheng and Toksöz (1981). Chen (1993) used the generalized R/T method to compute the normal modes in horizontal layers. In Chapter 6, the generalized R/T coefficients method is further developed to determine the dispersion relation of normal modes in radially multi-layered media. This approach can simultaneously determine both phase velocities and corresponding eigen functions for normal modes in a borehole with an arbitrary number of radial layers. Based on this new dispersion relation, a general formula which describes the attenuation property of each mode in absorptive media is derived. We may use this formula to estimate the *S* wave attenuation from tube waves.

Chapter 2

Elastic Waves in Radially Multi-layered Media

In this chapter, a new method based on generalized reflection and transmission coefficients is proposed to calculate synthetic seismograms in radially multi-layered media without vertical variation (media with vertical variation are considered in Chapter 3). This method can be used to efficiently simulate full waveform acoustic logging, crosswell seismic profiling, and single borehole profiling in situations where we need to consider borehole effects. The formulation is tested by comparing the numerical results with available previous work, showing excellent agreement. Because of the use of the normalized Hankel functions and the normalization factors, this new algorithm for computing seismograms is numerically stable even for the high frequency problem. Thus, we can simulate some models that can not be solved by other methods. An example of this is given in Section 2.5.1. In Chapter 5, I will apply this method for acoustic full waveform logging to investigate the effects of complex invaded zones on the geometrical spreading and attenuation estimation for *P* waves.

2.1 INTRODUCTION

Sonic logging in cased boreholes is useful for evaluating the quality of the cement job. Although acoustic logging in open boreholes is common, effort is also being made to measure formation properties from acoustic logs run in cased boreholes. A cased borehole and near borehole alterations, e.g., mudcake and invaded zones, can be modeled as a radially layered medium. A fluid-filed open borehole is also a radially layered medium. Thus, study of elastic waves in a radially layered medium is useful for understanding and interpreting full wave form sonic logs. Tubman et al. (1984) used the Thomson-Haskell method to study this problem. In this study we propose an alternative approach, i.e., the generalized reflection and transmission (R/T) coefficients method. The generalized R/T coefficients method is widely used in modeling elastic waves in vertically layered media because of its computational stability and efficiency over the Thomson-Haskell method, especially for high frequency problems (see, e.g., Luco & Apsel, 1983; Kennett, 1983; Chen, 1993). Yao & Zheng (1985) derived a set of formulas for computing synthetic seismograms in a radially layered borehole environment using the generalized R/T coefficients method, but they did not conduct numerical tests to check their formulation. A set of alternative formulations are derived in this chapter, which are more stable and efficient than the previous methods for numerical computation. In this chapter, I introduce the concepts of modified and generalized reflection and transmission matrices for radially layered media and derive a recursive scheme to calculate them; then, I determine wave fields using the R/T matrices. To check the formulation, I compare the calculated results with that of Tubman et al. (1984) for a four-layer cased borehole model and those of Baker (1984) for borehole models with invaded zones. As special applications, I give two numerical examples in single borehole profiling.

2.2 GOVERNING EQUATIONS AND THEIR GENERAL SOLUTIONS

The elastodynamic equation for isotropic media can be written as (see, e.g., Aki and Richards, 1980)

$$\rho \frac{\partial^2 \mathbf{u}(\mathbf{x},t)}{\partial t^2} = \mathbf{f} + (\lambda + 2\mu)\nabla\nabla \cdot \mathbf{u}(\mathbf{x},t) - \mu\nabla \times \nabla \times \mathbf{u}(\mathbf{x},t), \tag{2.1}$$

where $\mathbf{u}$ is displacement field; $\mathbf{f}$ is the body force or source; ρ, λ and μ are density and Lamé constants, respectively. Let us consider a radially multi-layered model as shown in Figure 2.1. The first layer ($r < r^{(1)}$) is fluid. A point explosion source $\Phi(t)$ is located at *r*=0 and *z*=0. For this radially symmetric medium, the cylindrical coordinates

Figure 2.1 A radially multi-layered model: cased borehole.

$\mathbf{x} = (r, z)$ are used. Since there exist only *P* and *SV* waves in this radially symmetric problem, the displacement $\mathbf{u}$ can be written as (see Appendix A-1)

$$\mathbf{u}(r, z, t) = \nabla\phi + \nabla\times(\mathbf{e}_\theta\psi), \qquad (2.2)$$

where ϕ and ψ are *P* wave and *S* wave potentials, respectively. Substituting equation (2.2) into the elastodynamic equation (2.1) we obtain (see Appendix A-2)

$$(\lambda + 2\mu)\nabla^2\phi - \rho\ddot{\phi} = \Phi\frac{\delta(r)\delta(z)}{\pi r}, \qquad (2.3a)$$

$$\mu(\nabla^2\psi - \frac{\psi}{r^2}) - \rho\ddot{\psi} = 0. \qquad (2.3b)$$

Equations (2.3a) and (2.3b) apply to each separate layer. These equations plus the application of boundaries at each interface constitute our mathematical problem. It is easier to solve this problem in $k-\omega$ domain, because partial differential equations (2.3a) and (2.3b) in $k-\omega$ domain become ordinary differential equations in *r*. Through the Fourier transform pair

$$\tilde{f}(r, k, \omega) = \int_{-\infty}^{\infty}\int_{-\infty}^{\infty} f(r, z, t)e^{i\omega t - ikz}\,dtdz,$$

$$f(r, z, t) = \frac{1}{4\pi^2}\int_{-\infty}^{\infty}\int_{-\infty}^{\infty}\tilde{f}(r, k, \omega)e^{-(i\omega t - ikz)}\,d\omega dk,$$

we can transform a function from $z-t$ domain to $k-\omega$ domain and *vice versa*. From equation (2.3) we obtain the elastodynamic equations in $k-\omega$ domain as

$$\frac{d^2\tilde{\phi}^{(j)}}{dr^2} + \frac{1}{r}\frac{d\tilde{\phi}^{(j)}}{dr} + (k_\alpha^{(j)2} - k^2)\tilde{\phi}^{(j)} = F(\omega)\frac{\delta(r)}{(\lambda^{(j)} + 2\mu^{(j)})\pi r}, \qquad (2.4a)$$

$$\frac{d^2\hat{\psi}^{(j)}}{dr^2} + \frac{1}{r}\frac{d\hat{\psi}^{(j)}}{dr} - \frac{\hat{\psi}^{(j)}}{r^2} + (k_\beta^{(j)^2} - k^2)\hat{\psi}^{(j)} = 0\,, \tag{2.4b}$$

for $r^{(j-1)} < r < r^{(j)}$, where the cylindrical coordinate expression for differential operator ∇^2 and the derivative theorem for Fourier transform were used. Here, *j* denotes the layer index and $j = 1, 2, \ldots, N$ (define $r^{(0)} = 0$). In equation (2.4), $k_\alpha^{(j)} = \omega / \alpha^{(j)}$, $k_\beta^{(j)} = \omega / \beta^{(j)}$, $F(\omega)$ is the spectrum of source function $\Phi(t)$, and $\alpha^{(j)} = \sqrt{(\lambda^{(j)} + 2\mu^{(j)}) / \rho^{(j)}}$ and $\beta^{(j)} = \sqrt{\mu^{(j)} / \rho^{(j)}}$ are the velocities of the *P* wave and *S* wave in the *j*th layer, respectively.

The general solutions of equations (2.4a) and (2.4b) are

$$\hat{\phi}^{(j)}(r,k,\omega) = c_{p-}^{(j)} e^{i\nu_\alpha^{(j)}(r^{(j)}-r)}\,\overline{H}_o^{(2)}(\nu_\alpha^{(j)} r) + c_{p+}^{(j)} e^{i\nu_\alpha^{(j)}(r-r^{(j-1)})}\,\overline{H}_o^{(1)}(\nu_\alpha^{(j)} r)\,, \tag{2.5a}$$

$$\hat{\psi}^{(j)}(r,k,\omega) = c_{s-}^{(j)} e^{i\nu_\beta^{(j)}(r^{(j)}-r)}\,\overline{H}_1^{(2)}(\nu_\beta^{(j)} r) + c_{s+}^{(j)} e^{i\nu_\beta^{(j)}(r-r^{(j-1)})}\,\overline{H}_1^{(1)}(\nu_\beta^{(j)} r)\,, \tag{2.5b}$$

where $\nu_\alpha^{(j)} = \sqrt{k_\alpha^{(j)^2} - k^2}$, $\mathrm{Im}\{\nu_\alpha^{(j)}\} > 0$, $\nu_\beta^{(j)} = \sqrt{(k_\beta^{(j)})^2 - k^2}$, $\mathrm{Im}\{\nu_\beta^{(j)}\} > 0$, and *j* =2, 3, ..., *N*. Coefficients $c_{p-}^{(j)}$, $c_{p+}^{(j)}$, $c_{s-}^{(j)}$ and $c_{s+}^{(j)}$ are unknowns, where subscript "*p*" refers to the *P* wave, "*s*" refers to the *S* wave, "+" refers to outgoing waves and "-" refers to incoming waves. In the outer most layer (*j*=*N*+1), there exist only outward-going waves, i.e., $c_{p-}^{(N+1)} = 0$, $c_{s-}^{(N+1)} = 0$, and

$$\hat{\phi}^{(N+1)}(r,k,\omega) = c_{p+}^{(N+1)} e^{i\nu_\alpha^{(N+1)}(r-r^{(N)})}\,\overline{H}_o^{(1)}(\nu_\alpha^{(N+1)} r)\,, \tag{2.6a}$$

$$\hat{\psi}^{(N+1)}(r,k,\omega) = c_{s+}^{(N+1)} e^{i\nu_\beta^{(N+1)}(r-r^{(N)})}\,\overline{H}_1^{(1)}(\nu_\beta^{(N+1)} r)\,, \tag{2.6b}$$

where $\nu_\alpha^{(N+1)} = \sqrt{k_\alpha^{(N+1)^2} - k^2}$, Im{$\nu_\alpha^{(N+1)}$}>0, $\nu_\beta^{(N+1)} = \sqrt{k_\beta^{(N+1)^2} - k^2}$ and Im{$\nu_\beta^{(N+1)}$}. Here, $\overline{H}_n^{(1)}(x) = e^{-ix} H_n^{(1)}(x)$ and $\overline{H}_n^{(2)}(x) = e^{ix} H_n^{(2)}(x)$ are the first and second kind normalized Hankel functions of n^{th} order, respectively. It should be emphasized that the normalized Hankel functions are used instead of the ordinary Hankel functions ($H_n^{(1)}(x)$ and $H_n^{(2)}(x)$). For a large argument x, the ordinary Hankel functions are approximated as

$$H_n^{(1)}(x) \approx \sqrt{\frac{2}{\pi x}}\, e^{i(x - \frac{\pi n}{2} - \frac{\pi}{4})},$$
$$H_n^{(2)}(x) \approx \sqrt{\frac{2}{\pi x}}\, e^{-i(x - \frac{\pi n}{2} - \frac{\pi}{4})}.$$

When the argument x is complex, the imaginary part of x causes the exponential to increase or decay, making the numerical procedure unstable (computer may overflow or underflow). If we normalize them by multiplying factors e^{-ix} and e^{+ix}, respectively, their asymptotic behavior will be much improved. I will use the normalized Hankel functions ($\overline{H}_n^{(1)}(x)$ and $\overline{H}_n^{(2)}(x)$) to express the solutions. Therefore, the algorithm is numerically stable even for large argument (the high frequency problem). Section 2.5.1 gives an example to show this.

In the fluid-filled borehole (j = 1), the solution is

$$\begin{aligned}\tilde{\phi}^{(1)}(r,k,\omega) &= cJ_o(\nu_\alpha^{(1)} r) + s_+ H_o^{(1)}(\nu_\alpha^{(1)} r)\\ &= c_{p-}^{(1)} e^{i\nu_\alpha^{(1)}(r^{(1)} - r)}\, \overline{H}_o^{(2)}(\nu_\alpha^{(1)} r) + (c_{p+}^{(1)} + s_+) e^{i\nu_\alpha^{(1)} r}\, \overline{H}_o^{(1)}(\nu_\alpha^{(1)} r)\end{aligned} \tag{2.7a}$$

where

$$c_{p+}^{(1)} = c_{p-}^{(1)} e^{i\nu_\alpha^{(1)} r^{(1)}} = \frac{c}{2}, \tag{2.7b}$$

and (see Appendix A-3)

$$s_+ = -\frac{i}{4(\lambda^{(1)} + 2\mu^{(1)})} F(\omega);$$

where J_o is Bessel function of the zero order.

Using the potential solutions [equations (2.5) – (2.7)], the radial and vertical components of the displacements ($\hat{u}_r^{(j)}$ and $\hat{u}_z^{(j)}$) and the stresses ($\hat{\sigma}^{(j)}$ and $\tau^{(j)}$) in the cylindrical solid layers (*j* >1) are expressed as

$$\hat{u}_r^{(j)} = \frac{\partial \hat{\phi}^{(j)}}{\partial r} - \frac{\partial \hat{\psi}^{(j)}}{\partial z},$$

$$\hat{u}_z^{(j)} = \frac{\partial \hat{\phi}^{(j)}}{\partial z} + \frac{\partial (r\hat{\psi}^{(j)})}{r\partial r},$$

$$\hat{\sigma}^{(j)} = -\lambda^{(j)} k_\alpha^{(j)^2} \hat{\phi}^{(j)} + 2\mu^{(j)} \left(\frac{\partial^2 \hat{\phi}^{(j)}}{\partial r^2} - ik \frac{\partial \hat{\psi}^{(j)}}{\partial r}\right),$$

and

$$\hat{\tau}^{(j)} = \mu^{(j)} [i2k \frac{\partial \hat{\phi}^{(j)}}{\partial r} + (2k^2 - k_\beta^{(j)^2}) \hat{\psi}^{(j)}].$$

Substituting equations (2.5–2.7) into these formulas, we obtain the expressions for displacements and stresses in the *j*th solid layer as

$$\begin{bmatrix} \hat{u}_r^{(j)}(r) \\ \hat{u}_z^{(j)}(r) \\ \hat{\sigma}^{(j)}(r) \\ \hat{\tau}^{(j)}(r) \end{bmatrix} = \begin{bmatrix} e_{11}^{(j)}(r) & e_{12}^{(j)}(r) & e_{13}^{(j)}(r) & e_{14}^{(j)}(r) \\ e_{21}^{(j)}(r) & e_{22}^{(j)}(r) & e_{23}^{(j)}(r) & e_{24}^{(j)}(r) \\ e_{31}^{(j)}(r) & e_{32}^{(j)}(r) & e_{33}^{(j)}(r) & e_{34}^{(j)}(r) \\ e_{41}^{(j)}(r) & e_{42}^{(j)}(r) & e_{43}^{(j)}(r) & e_{44}^{(j)}(r) \end{bmatrix} \begin{bmatrix} c_{p_-}^{(j)} \\ c_{s_-}^{(j)} \\ c_{p_+}^{(j)} \\ c_{s_+}^{(j)} \end{bmatrix}. \qquad (2.8)$$

For the first layer (i.e., *j*=1, the liquid layer), the displacement and the stress are

$$\begin{bmatrix} \tilde{u}_r^{(1)}(r) \\ \tilde{\sigma}^{(1)}(r) \end{bmatrix} = \begin{bmatrix} e_{11}^{(1)}(r) & e_{12}^{(1)}(r) \\ e_{21}^{(1)}(r) & e_{22}^{(1)}(r) \end{bmatrix} \begin{bmatrix} c_{p-}^{(1)} \\ c_{p+}^{(1)} + s_+ \end{bmatrix}. \tag{2.9}$$

Here, the explicit expressions of the elements $\{e_{nm}^{(j)}\}$ in equations (2.8) and (2.9) are given in the Appendix A-4. The unknown coefficients, $c_{p\pm}^{(j)}$ and $c_{s\pm}^{(j)}$, can be determined by imposing the boundary conditions at interfaces.

The jth layer has an outer radius of $r^{(j)}$ and an inner radius of $r^{(j-1)}$. (define $r^{(0)} = 0$). At the outer radius of the first layer (j=1), which is a liquid-solid boundary, the boundary conditions are

$$\begin{bmatrix} \tilde{u}_r^{(1)}(r^{(1)}) \\ \tilde{\sigma}^{(1)}(r^{(1)}) \\ 0 \end{bmatrix} = \begin{bmatrix} \tilde{u}_r^{(2)}(r^{(1)}) \\ \tilde{\sigma}^{(2)}(r^{(1)}) \\ \tilde{\tau}^{(2)}(r^{(1)}) \end{bmatrix}. \tag{2.10}$$

The shear stress in the liquid is zero. At the outer radius of the jth layer (j = 2, 3,..., N), which is a solid-solid boundary, the boundary conditions are

$$\begin{bmatrix} \tilde{u}_r^{(j)}(r^{(j)}) \\ \tilde{u}_z^{(j)}(r^{(j)}) \\ \tilde{\sigma}^{(j)}(r^{(j)}) \\ \tilde{\tau}^{(j)}(r^{(j)}) \end{bmatrix} = \begin{bmatrix} \tilde{u}_r^{(j+1)}(r^{(j)}) \\ \tilde{u}_z^{(j+1)}(r^{(j)}) \\ \tilde{\sigma}^{(j+1)}(r^{(j)}) \\ \tilde{\tau}^{(j+1)}(r^{(j)}) \end{bmatrix}. \tag{2.11}$$

2.3 GENERALIZED R/T MATRICES AND SOLUTION SYNTHESIS

In Section 2.2, I obtained the general solutions with unknown coefficients, $c_{p\pm}^{(1)}$, and $c_{p_-}^{(j)}$, $c_{p_+}^{(j)}$, $c_{s_-}^{(j)}$, and $c_{s_+}^{(j)}$ for j =2, 3, ..., N+1. To derive an effective algorithm for solving these unknown coefficients, the generalized reflection and transmission matrices are introduced. The generalized R/T matrices can be obtained through modified R/T matrices. Therefore, let us first introduce the modified reflection and transmission matrices.

2.3.1 Modified R/T matrices

The modified R/T coefficients (matrices) are the same as the ordinary R/T coefficients, except for the normalization factors $e^{i\nu_{\alpha,\beta}^{(j)} r^{(j)}}$ and $e^{-i\nu_{\alpha,\beta}^{(j)} r^{(j-1)}}$ [see equation (2.5)]. The modified R/T matrices, $\mathbf{R}_{+-}^{(j)}$, $\mathbf{R}_{-+}^{(j)}$, $\mathbf{T}_{+}^{(j)}$, and $\mathbf{T}_{-}^{(j)}$, for solid-solid interfaces are defined by the relations

$$\begin{cases} \mathbf{c}_{-}^{(j)} = \mathbf{R}_{+-}^{(j)} \mathbf{c}_{+}^{(j)} + \mathbf{T}_{-}^{(j)} \mathbf{c}_{-}^{(j+1)} \\ \mathbf{c}_{+}^{(j+1)} = \mathbf{T}_{+}^{(j)} \mathbf{c}_{+}^{(j)} + \mathbf{R}_{-+}^{(j)} \mathbf{c}_{-}^{(j+1)} \end{cases}, \qquad \text{for } j = 2, 3, \ldots, N, \tag{2.12a}$$

where $\mathbf{c}_{\pm}^{(j)} = [c_{p\pm}^{(j)}, c_{s\pm}^{(j)}]^{\mathrm{T}}$, and the modified R/T matrices, $\mathbf{R}_{+-}^{(j)}$, $\mathbf{R}_{-+}^{(j)}$, $\mathbf{T}_{+}^{(j)}$ and $\mathbf{T}_{-}^{(j)}$, are 2x2 matrices. For the first interface (liquid-solid), the modified R/T matrices, $R_{+-}^{(1)}$, $\mathbf{T}_{-}^{(1)}$, $\mathbf{T}_{+}^{(1)}$, and $\mathbf{R}_{-+}^{(1)}$ are defined by

$$\begin{cases} c_{-}^{(1)} = R_{+-}^{(1)} (c_{+}^{(1)} + s_{+}) + \mathbf{T}_{-}^{(1)} \mathbf{c}_{-}^{(2)} \\ \mathbf{c}_{+}^{(2)} = \mathbf{T}_{+}^{(1)} (c_{+}^{(1)} + s_{+}) + \mathbf{R}_{-+}^{(1)} \mathbf{c}_{-}^{(2)} \end{cases}, \tag{2.12b}$$

where $c_{\pm}^{(1)} = c_{p\pm}^{(1)}$, $R_{+-}^{(1)}$ is a scalar, and $\mathbf{T}_{-}^{(1)}$, $\mathbf{T}_{+}^{(1)}$ and $\mathbf{R}_{-+}^{(1)}$ are 1x2, 2x1 and 2x2 matrices, respectively.

Figure 2.2 Pictorial explanation of the modified reflection and transmission coefficients.

The modified R/T matrices describe the reflection and transmission at the current interface excluding the effects of multiple reflections and transmissions due to other existing interfaces (see Figure 2.2 for a pictorial explanation).

Substituting equation (2.5) into equation (2.11), then comparing with equation (2.12a) we obtain (see Appendix A-5)

$$\begin{bmatrix} \mathbf{R}_{+-}^{(j)} & \mathbf{T}_{-}^{(j)} \\ \mathbf{T}_{+}^{(j)} & \mathbf{R}_{-+}^{(j)} \end{bmatrix} = \begin{bmatrix} e_{11}^{(j)}(r^{(j)}) & e_{12}^{(j)}(r^{(j)}) & -e_{13}^{(j+1)}(r^{(j)}) & -e_{14}^{(j+1)}(r^{(j)}) \\ e_{21}^{(j)}(r^{(j)}) & e_{22}^{(j)}(r^{(j)}) & -e_{23}^{(j+1)}(r^{(j)}) & -e_{24}^{(j+1)}(r^{(j)}) \\ e_{31}^{(j)}(r^{(j)}) & e_{32}^{(j)}(r^{(j)}) & -e_{33}^{(j+1)}(r^{(j)}) & -e_{34}^{(j+1)}(r^{(j)}) \\ e_{41}^{(j)}(r^{(j)}) & e_{42}^{(j)}(r^{(j)}) & -e_{43}^{(j+1)}(r^{(j)}) & -e_{44}^{(j+1)}(r^{(j)}) \end{bmatrix}^{-1}$$

$$\times \begin{bmatrix} -e_{13}^{(j)}(r^{(j)}) & -e_{14}^{(j)}(r^{(j)}) & e_{11}^{(j+1)}(r^{(j)}) & e_{12}^{(j+1)}(r^{(j)}) \\ -e_{23}^{(j)}(r^{(j)}) & -e_{24}^{(j)}(r^{(j)}) & e_{21}^{(j+1)}(r^{(j)}) & e_{22}^{(j+1)}(r^{(j)}) \\ -e_{33}^{(j)}(r^{(j)}) & -e_{34}^{(j)}(r^{(j)}) & e_{31}^{(j+1)}(r^{(j)}) & e_{32}^{(j+1)}(r^{(j)}) \\ -e_{43}^{(j)}(r^{(j)}) & -e_{44}^{(j)}(r^{(j)}) & e_{41}^{(j+1)}(r^{(j)}) & e_{42}^{(j+1)}(r^{(j)}) \end{bmatrix}, \qquad (2.13)$$

for $j = 2, 3, ..., N$. Similarly, from equations (2.7), (2.9), (2.10) and (2.12b), we find

$$\begin{bmatrix} R_{+-}^{(1)} & \mathbf{T}_{-}^{(1)} \\ \mathbf{T}_{+}^{(1)} & \mathbf{R}_{-+}^{(1)} \end{bmatrix} = \begin{bmatrix} e_{11}^{(1)}(r^{(1)}) & -e_{13}^{(2)}(r^{(1)}) & -e_{14}^{(2)}(r^{(1)}) \\ e_{21}^{(1)}(r^{(1)}) & -e_{33}^{(2)}(r^{(1)}) & -e_{34}^{(2)}(r^{(1)}) \\ 0 & -e_{43}^{(2)}(r^{(1)}) & -e_{44}^{(2)}(r^{(1)}) \end{bmatrix}^{-1} \times \begin{bmatrix} -e_{12}^{(1)}(r^{(1)}) & e_{11}^{(2)}(r^{(1)}) & e_{12}^{(2)}(r^{(1)}) \\ -e_{22}^{(1)}(r^{(1)}) & e_{31}^{(2)}(r^{(1)}) & e_{32}^{(2)}(r^{(1)}) \\ 0 & e_{41}^{(2)}(r^{(1)}) & e_{42}^{(2)}(r^{(1)}) \end{bmatrix}, \tag{2.14}$$

for j=1. Equations (2.13) and (2.14) provide the formulas for computing the modified R/T matrices for each layer.

2.3.2 Generalized R/T matrices

The purpose of introducing the generalized R/T matrices is to derive an effective recursive algorithm for solving coefficients $\mathbf{c}_{\pm}^{(j+1)}$. The generalized R/T matrices, $\hat{\mathbf{R}}_{+-}^{(j)}$ and $\hat{\mathbf{T}}_{+}^{(j)}$, are defined through the following relations:

$$\begin{cases} \mathbf{c}_{+}^{(j+1)} = \hat{\mathbf{T}}_{+}^{(j)}\mathbf{c}_{+}^{(j)} \\ \mathbf{c}_{-}^{(j)} = \hat{\mathbf{R}}_{+-}^{(j)}\mathbf{c}_{+}^{(j)} \end{cases} \qquad \text{for } j = 2, 3, ..., N; \tag{2.15a}$$

and

$$\begin{cases} \mathbf{c}_{+}^{(2)} = \hat{\mathbf{T}}_{+}^{(1)}(c_{+}^{(1)} + s_{+}) \\ c_{-}^{(1)} = \hat{R}_{+-}^{(1)}(c_{+}^{(1)} + s_{+}) \,. \end{cases} \tag{2.15b}$$

The generalized R/T matrices describe the overall reflections and transmissions at an interface. Figure 2.3 gives an illustration of the generalized R/T coefficients. At the interface between layer j and layer j+1, the generalized reflection coefficient represents the primary reflection and all multiples back to layer j; and the generalized transmission coefficient represents the primary transmission and all multiples away from the interface in layer j+1.

Figure 2.3 Pictorial explanation of the generalized reflection and transmission coefficients.

Substituting equation (2.15) into equation (2.12) and rearranging terms, we obtain a recursive relation (see Appendix A-6)

$$\begin{cases} \tilde{\mathbf{T}}_{+}^{(j)} = [\mathbf{I} - \mathbf{R}_{-+}^{(j)} \tilde{\mathbf{R}}_{+-}^{(j+1)}]^{-1} \mathbf{T}_{+}^{(j)} \\ \tilde{\mathbf{R}}_{+-}^{(j)} = \mathbf{R}_{+-}^{(j)} + \mathbf{T}_{-}^{(j)} \tilde{\mathbf{R}}_{+-}^{(j+1)} \tilde{\mathbf{T}}_{+}^{(j)} \end{cases}, \quad \text{for } j = N, N\text{-}1, \ldots, 2, 1, \tag{2.16}$$

where **I** is the unit matrix, $\tilde{\mathbf{R}}_{+-}^{(j)}$ and $\tilde{\mathbf{T}}_{+}^{(j)}$ are 2x2 matrices for $j > 1$, $\tilde{\mathbf{T}}_{+}^{(1)}$ is a 2x1 matrix, and $\tilde{\mathbf{R}}_{+-}^{(1)} = \tilde{R}_{+-}^{(1)}$ is a scalar. In the outer most layer ($j = N$+1), there exist only outward-going waves, i.e., $\mathbf{c}_{-}^{(N+1)} = \mathbf{0}$. Therefore, from equation (2.15a) we know

$$\tilde{\mathbf{R}}_{+-}^{(N+1)} = \mathbf{0} \ . \tag{2.17}$$

Equation (2.16) along with the initial condition given by equation (2.17) provides an efficient recursive scheme to calculate the generalized R/T matrices from the modified R/T matrices given in equations (2.13) and (2.14). These formulas for computing the R/T matrices are numerically stable because of the use of the normalized Hankel functions and the normalization factors $e^{i\nu_{\alpha,\beta}^{(j)}r^{(j)}}$ and $e^{-i\nu_{\alpha,\beta}^{(j)}r^{(j-1)}}$ in the potential solutions.

2.3.3 Solution synthesis

Having the generalized R/T matrices, we can compute the unknowns $\mathbf{c}_{\pm}^{(j)}$ for any layer. Therefore, we can determine the displacements and stresses for any layer. From equations (2.7b) and (2.15b) we obtain

$$\begin{cases} c_{p+}^{(1)} + s_{+} = (1 - \hat{R}_{+-}^{(1)} e^{i\nu_{\alpha}^{(1)} r^{(1)}})^{-1} s_{+} \\ c_{p-}^{(1)} = \hat{R}_{+-}^{(1)} (1 - \hat{R}_{+-}^{(1)} e^{i\nu_{\alpha}^{(1)} r^{(1)}})^{-1} s_{+} \end{cases} . \tag{2.18a}$$

Then, from equations (2.15a), (2.15b) and (2.18a) we obtain the relations for calculating the coefficients $\mathbf{c}_{\pm}^{(j)}$ as

$$\begin{cases} \mathbf{c}_{+}^{(j)} = \hat{\mathbf{T}}_{+}^{(j-1)} \hat{\mathbf{T}}_{+}^{(j-2)} \ldots \hat{\mathbf{T}}_{+}^{(1)} (1 - \hat{R}_{+-}^{(1)} e^{i\nu_{\alpha}^{(1)} r^{(1)}})^{-1} s_{+} \\ \mathbf{c}_{-}^{(j)} = \hat{\mathbf{R}}_{+-}^{(j)} \mathbf{c}_{+}^{(j)} \end{cases} , \tag{2.18b}$$

where $j = 2, 3, ..., N, N+1$. Incorporating $\mathbf{c}_{\pm}^{(j)}$ into equation (2.8) for $j = 2, 3, ..., N, N+1$, or equation (2.9) for $j = 1$, we can obtain the solutions for displacements and stresses in any layer.

In the sonic logging problem we are interested in the stress wave in the fluid-filled borehole where the normal stress is

$$
\begin{aligned}
\hat{\sigma}^{(1)}(r) &= e_{11}^{(1)}(r)c_{p-}^{(1)} + e_{12}^{(1)}(r)(c_{p+}^{(1)} + s_{+}) \\
&= \lambda^{(1)} k_{\alpha}^{(1)^2} \left[\frac{2J_o(\nu_{\alpha}^{(1)} r)e^{i\nu_{\alpha}^{(1)} r^{(1)}} \hat{R}_{+-}^{(1)}}{\hat{R}_{+-}^{(1)} e^{i\nu_{\alpha}^{(1)} r^{(1)}} - 1} - H_o^{(1)}(\nu_{\alpha}^{(1)} r) \right] s_{+} .
\end{aligned}
\tag{2.19}
$$

By taking inverse Fourier transforms over k and ω ($k-\omega$ domain), we finally obtain the complete solution in the spatial and time domain ($z-t$ domain) as

$$
\sigma^{(1)}(r,z,t) = \frac{\rho^{(1)}}{2(\lambda^{(1)} + 2\mu^{(1)})} \int_{-\infty}^{+\infty} \omega^2 F(\omega) e^{-i\omega t} \left\{ \int_{-\infty}^{+\infty} i \frac{J_o(\nu_{\alpha}^{(1)} r) e^{i\nu_{\alpha}^{(1)} r^{(1)}} \hat{R}_{+-}^{(1)}}{1 - e^{i\nu_{\alpha}^{(1)} r^{(1)}} \hat{R}_{+-}^{(1)}} e^{ikz} dk + \frac{1}{R} e^{ik_{\alpha}^{(1)} R} \right\} d\omega ,
\tag{2.20}
$$

where, $R = \sqrt{r^2 + z^2}$ and $\hat{R}_{+-}^{(1)}$ is the generalized reflection coefficient on the first interface (fluid-solid interface).

2.4 IMPLEMENTATION AND VERIFICATION TESTS

The elastodynamic solutions [equations (2.8) and (2.9)] are in terms of radius r, wavenumber k and angular frequency ω, i.e., they are in $k-\omega$ domain. we should transform them from $k-\omega$ domain to $z-t$ domain. The transformation from wavenumber (k) domain to spatial (z) domain can be achieved by using any numerical integral approach. Due to the physical clarity and simplicity, I here use the discrete wave-number technique (Bouchon & Aki, 1977) to evaluate the integral over wavenumber k. The transformation from angular frequency ω to time t is calculated using an FFT algorithm. Moreover, the complex frequency ($\omega=\omega_R+i\ \omega_I$) introduced in the discrete wavenumber method makes the calculation fast and stable (Chen, 1991, Page 89). To check the validity of the formulation, I compare the numerical results with available previous work.

2.4.1 Discrete wavenumber integration

We can numerically evaluate the integral over wavenumber k in equation (2.20) by discretizing k along the real axis. To remove the singularities from the real k-axis, we can introduce a small positive imaginary frequency ω_I, that is, let

$$\omega = \omega_R + i \ \omega_I. \tag{2.21}$$

An integral as equation (2.20) can be generally written as

$$\sigma(r,z,t) = \int_{-\infty}^{+\infty} \int_{-\infty}^{+\infty} f(r,k,\omega) e^{ikz} e^{-i\omega t} dk d\omega \ . \tag{2.22}$$

Using equation (2.21) and numerically integrating equation (2.22), we get

$$\sigma(r,z,t) = e^{\omega_I t} \int_{-\infty}^{+\infty} e^{-i\omega_R t} \{ \sum_{n=-M(\omega)}^{M(\omega)} f(r, n\Delta k, \omega_R + i\omega_I) \exp(n\Delta kz)\Delta k \} d\omega_R \ . \tag{2.23}$$

The effect of introducing the imaginary frequency ω_I is removed by the multiplying factor $e^{\omega_I t}$ in the time domain result. Integration interval Δk is equivalent to an infinite distribution of sources separated by a distance $L = 2\pi/\Delta k$ from each other along the z-axis. L should be large enough (or Δk small enough) so that first arrivals from neighboring sources are out of the time window under consideration. The introduction of imaginary angular frequency ω_I also makes it possible to choose a larger Δk , and therefore makes the calculation faster (Chen, 1991, Page 89). Let T_{max} be the time window length, V_{max} be the maximum velocity in the study area. Then we choose $L = 1.5V_{max}T_{max}$, $\Delta k = 2\pi/L$, so that the first arrivals from other artificial sources are beyond the time window selected. A proper choice of imaginary frequency is $\omega_I = \pi/T_{max}$. The smaller ω_I is, the smaller distortion of the waveform will be. However, if ω_I is too small, some numerical artifacts caused by discrete Fourier transform may show up at the beginning of a wave trace. To make the numerical integral convergent, the summation upper limit $M(\omega)$ should be large enough (e.g., $M(\omega) > B\,|\omega|/V_{\min}$, B=1.5 ~ 3).

2.4.2 Cased borehole

The first verification test is a four-layer cased borehole model chosen from Tubman et al. (1984), (see Figure 2.1). The model parameters are listed in Table 2.1. The spectrum of the source function is described by

$$F(\omega) = \frac{1}{\omega^2}\frac{8\alpha\omega_o(\alpha - i\omega)}{[(\alpha - i\omega)^2 + \omega_o^2]^2}, \tag{2.25}$$

where $\omega_o = 2\pi \times$ 13 KHz and $\alpha = 0.5\omega_o/\pi$. The source-receiver separation is 3.048 m. Attenuation is introduced through the complex velocity defined by (see, e.g., Aki and Richards, 1980)

$$V(\omega) = V(\omega_{ref})[1 + \frac{1}{\pi Q}\log(\frac{\omega}{\omega_{ref}}) - \frac{i}{2Q}], \tag{2.26}$$

where Q is the quality factor for either P waves or S waves, and V is either the P wave velocity or S wave velocity. The imaginary term in equation (2.26) is determined from the desired Q and added to the elastic velocity. It is this imaginary term that causes an exponential decay into the waveform as the wave propagates. The decay or attenuation is proportional to the frequency. To retain causality, the real part of the velocity is modified by introducing velocity dispersion. The second term in equation (2.26) gives this velocity dispersion.

Table 2.1 Model parameters used for Figures 4a and 4b.

Layer	r (cm)	α (km/s)	β (km/s)	ρ (g/cm^3)	Q_p	Q_s
Fluid	4.7	1.68	–	1.2	20	–
Casing	5.72	6.1	3.35	7.5	1000	1000
Cement	10.2	2.82	1.73	1.92	40	30
Formation	∞	4.88	2.6	2.16	60	60

Figure 2.4 (a) Seismogram calculated by the generalized R/T coefficient method for a four-layer cased borehole model; (b) Seismogram taken from Page 1055 in Tubman (1984) for comparison with figure 2a.

Figure 2.4a is the seismogram calculated by the generalized R/T coefficient method, and Figure 2.4b is the result of Tubman et al. (1984). It can be seen that the travel times of all phases are the same. The waveforms are the similar too, except that the waveform around 1.8 ms is slightly different. The comparison shows an overall good agreement. I will give more comparisons in the next section.

2.4.3 Boreholes with invaded zones

I choose two invaded zone models from Baker (1984) for comparison. There are two typical invaded zones: the damaged zone and the flushed zone. In Baker's terminology, a damaged zone has a velocity slower than the unperturbed formation velocity, and a flushed zone has a velocity faster than the unperturbed formation velocity. The source function is a Ricker wavelet whose spectrum is

$$F(\omega) = 4\sqrt{\pi}\,\frac{\omega^2}{\omega_o^3}\exp\left[-\left(\frac{\omega}{\omega_o}\right)^2\right], \tag{2.27}$$

where $\omega_o = 2\pi \times 10$ KHz. There is no attenuation introduced in this example.

Figures 2.5 and 2.6 show the comparisons of the seismograms calculated by generalized R/T coefficients method with those calculated by the Thomson-Haskell method (Baker, 1984). The model parameters used to calculate the seismograms in Figures 2.5 and 2.6 are given in Tables 2.2 and 2.3, respectively. Travel times, phases and waveforms in the seismograms are the same for these two methods. The comparisons show excellent agreement.

Figure 2.5 (a) Seismograms calculated by R/T method for the models given in Table 2; (b) Seismograms taken from Baker (1984, Page 800, Figure 7) for comparison with (a).

Figure 2.6 (a) Seismograms calculated by R/T method for the models given in Table 3; (b) Seismograms taken from Baker (1984, Page 801, Figure 10) for comparison with (a).

Table 2.2a Model parameters of a simple borehole.

Layer	*r* (cm)	α (km/s)	β (km/s)	ρ (g/cm^3)
Fluid	15.24	1.524	–	1.02
Formation	∞	4.876	2.743	2.25

Table 2.2b Model parameters of a damaged borehole.

Layer	*r* (cm)	α (km/s)	β (km/s)	ρ (g/cm^3)
Fluid	15.24	1.524	–	1.02
Damaged zone	30.48	4.876	2.743	2.25
Formation	∞	5.364	2.895	2.25

Table 2.3a Model parameters of a simple borehole.

Layer	r (cm)	α (km/s)	β (km/s)	ρ (g/cm^3)
Fluid	12.20	1.524	–	1.02
Formation	∞	3.962	1.828	2.14

Table 2.3b. Model parameters of a flushed borehole.

Layer	r (cm)	α (km/s)	β (km/s)	ρ (g/cm^3)
Fluid	12.20	1.524	–	1.02
Flushed zone	27.43	3.962	1.828	2.14
Formation	∞	3.048	2.133	1.734

2.5 SPECIAL APPLICATIONS

Single borehole profiling is a relatively new measurement. In single borehole profiling, the source and receiver(s) are in the same borehole. It can be viewed as acoustic logging with low frequency source (~1 KHz) and large source-receiver offsets (~100 m). Single borehole profiling attempts to fill the frequency gap between conventional VSP (~0.1 KHz) and acoustic logging (~10 KHz). Chen (1993) and Chen et al. (1994) developed a single borehole profiling tool and collected some field data. The low frequency and large offset allow the waves to penetrate the invaded zones and casing. Therefore, we can measure the velocity and attenuation for undisturbed formation. It may also detect the reflection from a fault or a salt dome near the borehole. I present two numerical examples to investigate the near borehole reflection and deeper penetration features of the single borehole profiling. The simulation is done by the generalized R/T coefficient method.

2.5.1 Reflection due to a large outer-cylindrical structure

Let us first consider a scattering problem due to an outer-cylindrical formation. The physical configuration of this model is shown in Figure 2.7a in which a simple open borehole is surrounded by a two-cylindrical-layer composite formation. Receivers are clamped to the borehole wall, and the source-receiver offset ranges from 10m to 150m. Other model parameters are listed in Table 2.4. This model is useful in the study of single borehole imaging, i.e., reflection imaging of reflectors near a borehole. From this simulation, we can understand what and where reflections would appear on a seismogram, what are the relative amplitudes of these reflections, and how much the tube wave energy has to be attenuated in order to observe the reflections.

The calculated seismograms are shown in Figure 2.7b which are the displacement component in r-direction. To more clearly indicate the scattering phases (i.e., reflections from the interface between formation I and formation II), I normalized each trace by using its maximum value rather than a global scale for all traces. We can see from Figure 2.7b that phases show up as expected. It should be emphasized that I set an extremely low Q-value ($Q_f = 3$) for the fluid in the borehole to reduce the tube wave energy. If Q_f is not low enough, we can only see tube waves on the seismograms. Therefore, the attenuation of tube waves is one of the key problems for single borehole profiling. Chen et al. (1994) gave an example of field study on the single borehole profiling.

In this calculation, the peak frequency of the Ricker wavelet is 800 Hz, thus the corresponding characteristic wave-length is about 2m to 3.5m. The thickness of formation I is about 100m and is much greater than the characteristic wavelength. Therefore, this is a typical high-frequency scattering problem. As mentioned earlier, the use of the normalized

Hankel functions makes the algorithm numerically stable even for very high frequencies. I also tried this model with ordinary Hankel functions, but the calculation failed because of the arithmetic overflow. This is a good example showing why we need the normalized formulation.

Table 2.4 Parameters of a scattering model

Layer	r (m)	α (km/s)	β (km/s)	Q_p	Q_s	ρ (g/cm^3)
Fluid	0.11	1.6	–	3	–	1.0
Formation I	100	3.0	1.85	200	120	2.1
Formation II	∞	1.9	1.4	50	40	1.8

Figure 2.7 (a) Configuration of the model; (b) Seismograms of horizontal displacement *u*. Each trace is scaled by its maximum. Here, "P" indicates the direct *P* wave; "S" the direct *S* wave; "P-P, S-S, P-S and S-P" are primary reflections; "P-P-P-P" is a *P* wave multiple reflection.

2.5.2 Low frequency acoustic logging

The rock properties near a borehole wall is often altered during drilling, forming an invaded zone. The altered depth is usually 0.2 to 0.8 meters. Baker (1984) studied the effects of invaded zones on conventional acoustic logging. For conventional acoustic logging, the first arrival could only penetrate a few inches into the formation depending on the frequency and source to receiver spacing. Low frequency logging (or single borehole profiling) can penetrate deeper. In low frequency logging, however, tube waves become very strong in comparison with direct waves. We have to suppress tube waves to make the direct waves observable.

This section gives a numerical simulation on the low frequency acoustic logging. Table 2.5 lists the model parameters used. Figure 2.8a shows the model configuration. Figure 2.8b shows the seismograms with short source-receiver offsets and high source frequency (Ricker wavelet with peak frequency = 10 KHz). Each trace is normalized to unity by using each trace's maximum value. The direct *P* wave in this case propagates with a velocity of 5 km/s which is the velocity of the invaded zone. In this model, the invaded zone has a higher velocity than the formation. Thus, according to the ray theory, there are only refracted waves at the fluid/invaded zone interface, and no refracted waves at the invaded zone/formation interface. When we reduce the source frequency and/or increase the source to receiver spacing, the wave energy can leak through the invaded zone and propagate in the undisturbed formation. Figure 2.8c shows an example with the source frequency of 1 KHz, and source to receiver offsets of 20-80 m. In this example, the first arrival is direct *P* wave whose propagating velocity is 4 km/s which is the formation velocity. Therefore, we can say that the frequency and source-receiver offset used in this test have the capability of penetrating the invaded zone to measure the formation velocity. If the invaded zone becomes thicker, we may need larger source-receiver offsets and/or lower source frequency to have a deeper penetration.

Table 2.5 Model parameters for low frequency logging simulation

Layer	*r* (m)	Vp (km/s)	Vs (km/s)	Q_p	Q_s	ρ (g/cm^3)
Fluid	0.1	1.6	–	3	–	1.1
Invaded zone	0.3	5.0	3.0	300	150	2.7
Formation	∞	4.0	2.2	200	120	2.6

Figure 2.8a An invaded zone model used for low frequency logging simulation. V_f, V_{p1} and V_{p2} are *P* wave velocities for borehole fluid, invaded zone and formation, respectively.

Figure 2.8b Conventional acoustic simulation with peak frequency of 10 KHz and small source-receiver offsets. The first arrival corresponds to the *P* wave velocity (5 km/s) in the invaded zone.

Figure 2.8c Low frequency acoustic logging with peak frequency of 1 KHz and large source-receiver offsets. The direct wave propagates at the formation *P* wave velocity (4 km/s)

2.6 CONCLUSIONS

A method based on generalized reflection and transmission coefficients is developed to calculate synthetic seismograms in radially layered media. This approach can be used to simulate borehole related seismic measurements, such as, acoustic logging, vertical seismic profiling, crosswell seismic profiling, and single borehole profiling. The normalized Hankel functions and the recursive scheme are introduced to make the numerical procedure more stable and efficient. This provides an algorithm to simulate the reflection from an outer-cylinder with a large diameter, a typical high frequency problem. The validity of this new approach has been confirmed by comparing with previous available results for a four-layer cased borehole model (Tubman et al., 1984), and for invaded zone models (Baker, 1984).

Two special examples for single borehole profiling are presented in this chapter. Single borehole profiling is a relatively new borehole measurement. Simulations performed in this chapter are helpful for understanding the events which are expected to appear in the records, and what frequency are suitable for measuring the formation velocities through the near borehole alternations. In these simulations, the calculated wave fields are exact and complete solutions, but the model is highly simplified as radially multi-layered media. Obviously, use of a cylindrical layer to simulate a salt dome or a plane layer is a very rough approximation.

This method is extensively used for seismic attenuation study in Chapters 5 and 6. In Chapter 3, this method is further developed to simulate radial layers with vertical variations. However, when a radially layered medium has vertical variations, the computation will largely increase.

Chapter 3

Elastic Waves in Complex Radially Symmetric Media

The generalized reflection and transmission coefficients method with normal mode expansion is developed to calculate the elastic wave field for acoustic logging and crosswell seismic simulation in complex radially symmetric media. This method simulates models which consist of arbitrary cylindrical layers with each cylindrical layer having arbitrary layers in the vertical direction. In practical applications, boreholes that have casing with perforations, source arrays, and boreholes embedded in layered media can be treated as models of this type. Faults can be approximated as symmetric structures. The simulation based on this method gives direct waves, reflections, transmissions, tube waves, tube wave conversions generated at casing perforations or horizontal interfaces, and the radiation pattern of a source in a complicated borehole. This method is semi-analytical. Compared with purely numerical approaches, such as finite difference and finite element methods, this semi-analytical method is faster and avoids the grid dispersion and inaccurate handling of fluid-solid interfaces. Moreover, this method can calculate the wave field at large distances in the formation. The scale difference between the small borehole diameter and a large formation extent, which causes numerical difficulties in purely numerical methods, is not a problem in this approach. Examples are presented to verify the formulation and show the applicability of this method. In Chapter 4, this simulation method is applied to test a new attenuation measurement technique: seismic attenuation tomography using the frequency shift method.

3.1 INTRODUCTION

For most borehole simulations (Chen et al., 1996; Tubman et al., 1984; Baker, 1984; Chapter 2 of this thesis), a borehole is modeled as cylindrical layers. In an actual borehole, however, the medium within a cylindrical layer usually is not homogeneous. Its elastic parameters often change with depth. Pai et al. (1993) simulated the electromagnetic induction logging for models of this kind. In acoustic logging problems we have to solve the elastodynamic equation considering both P and S waves. Therefore, the solutions for the elastic problem are more complex. For the elastic wave simulation, Bouchon (1993) and Dong et al. (1995) used a boundary element method for open and cased boreholes embedded in layered media, respectively. In this chapter, the generalized reflection and transmission coefficient method is further developed to calculate more realistic models, such as multi-layered boreholes (casing and invaded zones) embedded in multi-layered formation, symmetric faults in the formation, and a perforation or joint in a casing. Though this semi-analytical approach can only handle radially symmetric models, it is more efficient (less memory and computing time) than purely numerical approaches.

A general configuration of the problem considered in this chapter is shown in Figure 3.1, where the formation consists of several vertically heterogeneous cylinders, the source is located at the center of the borehole, and receivers are located either inside or outside the borehole. Although this model looks complicated, it still exhibits axial symmetry. Taking advantage of this symmetry we can derive a set of formulas to simulate the elastic wave propagation in this complex borehole-formation model. The key points in the formulation are (1) solving an eigenvalue problem for horizontal layers in a cylinder, (2) expanding the solution of the elastodynamic equation into the eigenfunctions, and (3) using the generalized reflection and transmission coefficient method to solve the boundary value problem for cylindrical layers. Because of the existence of horizontal layers, the wave numbers, *k*, are coupled. We must solve a system of equations for each frequency to simultaneously compute the wave field for all wave numbers. Therefore, the computational time is longer and the memory is larger than the algorithm presented in Chapter 2, where the model only has radial layers.

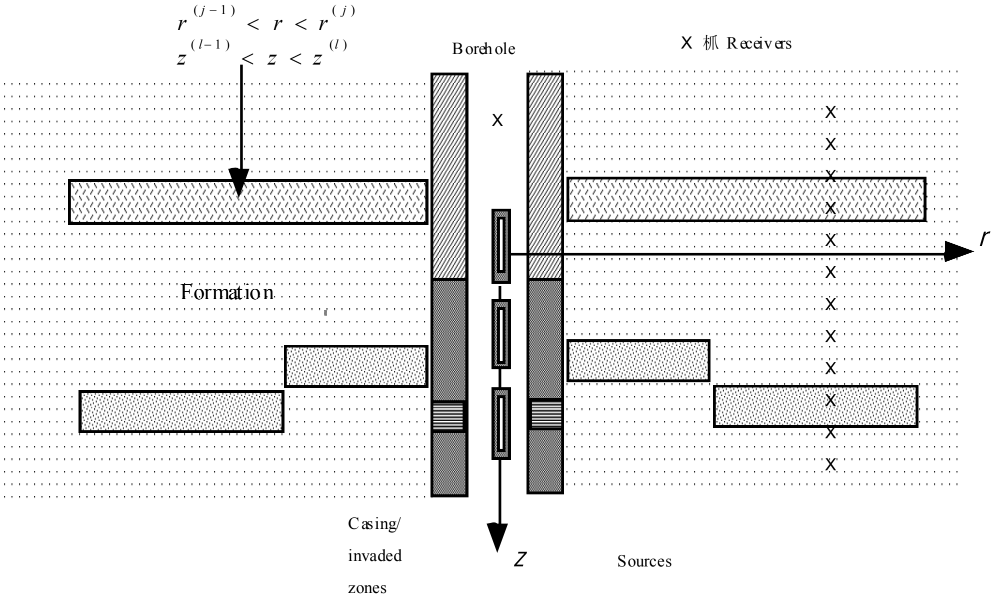

Figure 3.1 A complex radially symmetric model.

3.2 GOVERNING EQUATIONS

Let us start with the elastodynamic equation for isotropic media:

$$\rho \ddot{\mathbf{u}}(\mathbf{x},t) = \mathbf{f} + (\lambda + 2\mu)\nabla\nabla \cdot \mathbf{u}(\mathbf{x},t) - \mu\nabla \times \nabla \times \mathbf{u}(\mathbf{x},t) .$$

The potential method (Appendix A-2) is again used to solve this elastodynamic equation for the radially symmetric model shown in Figure 3.1. Since the model is radially symmetric, i.e., independent of θ in cylindrical coordinates, we can write the displacement for the j^{th} cylindrical layer as (Appendix A-1)

$$\mathbf{u}^{(j)} = \nabla \phi^{(j)} + \nabla \times (\mathbf{e}_\theta \psi^{(j)}) ,$$

where the P wave potential $\phi^{(j)}$ and S wave potential $\psi^{(j)}$ satisfy

$$\frac{\partial^2 \hat{\phi}^{(j)}(r,z)}{\partial r^2} + \frac{1}{r}\frac{\partial \hat{\phi}^{(j)}(r,z)}{\partial r} + \frac{\partial^2 \hat{\phi}^{(j)}(r,z)}{\partial z^2} + k_\alpha^{(j)^2}(z)\hat{\phi}^{(j)}(r,z) = F(\omega)\frac{\delta(r)\delta(z-z_s)}{(\lambda^{(j)} + 2\mu^{(j)})\pi r} , \tag{3.1a}$$

$$\frac{\partial^2 \hat{\psi}^{(j)}(r,z)}{\partial r^2} + \frac{1}{r}\frac{\partial \hat{\psi}^{(j)}(r,z)}{\partial r} - \frac{\hat{\psi}^{(j)}(r,z)}{r^2} + \frac{\partial^2 \hat{\psi}^{(j)}(r,z)}{\partial z^2} + k_\beta^{(j)^2}(z)\hat{\psi}^{(j)}(r,z) = 0 . \tag{3.1b}$$

for $r^{(j-1)} < r < r^{(j)}$ (define $r^{(0)}$=0), where, *F(ω)* is a source function in frequency domain, (*r, z*) = (0, z_S) are the coordinates of the source location, $k_\alpha^{(j)^2}(z) = \omega^2 / [\alpha^{(j)}(z)]^2$ and $k_\beta^{(j)^2}(z) = \omega^2 / [\beta^{(j)}(z)]^2$. Here, α and β are *P* and *S* velocities, respectively.

Note that $k_\alpha^{(j)}$ and $k_\beta^{(j)}$ are functions of coordinate *z*, we can not simply apply Fourier integral to transform potentials $\hat{\phi}^{(j)}(r,z)$ and $\hat{\psi}^{(j)}(r,z)$ from *z* domain to *k* domain, as we did in equation 2.4. To solve equations (3.1a) and (3.1b), let us expand the potentials in jth radial layer by a set of eigen-functions, $\{f_n^{(j)}(z),\ g_n^{(j)}(z);\ n = 1,2,\ \ldots,\ N\}$, as

$$\overset{?}{\phi}^{(j)}(r,z) = \sum_{n=1}^{N} \overset{?}{\phi}_n^{(j)}(r) f_n^{(j)}(z), \tag{3.2a}$$

$$\overset{?}{\psi}^{(j)}(r,z) = \sum_{n=1}^{N} \overset{?}{\psi}_n^{(j)}(r) g_n^{(j)}(z). \tag{3.2b}$$

where the eigenfunctions $f_n^{(j)}(z)$ and $g_n^{(j)}(z)$ satisfy

$$\begin{cases} \dfrac{d^2 f_n^{(j)}(z)}{dz^2} + [k_\alpha^{(j)}(z)]^2 f_n^{(j)}(z) = [\gamma_n^{(j)}]^2 f_n^{(j)}(z), & (3.3a) \\[2ex] \dfrac{d^2 g_n^{(j)}(z)}{dz^2} + [k_\beta^{(j)}(z)]^2 g_n^{(j)}(z) = [\nu_n^{(j)}]^2 g_n^{(j)}(z), & (3.3b) \end{cases}$$

$\gamma_n^{(j)}$ and $\nu_n^{(j)}$ are the corresponding eigenvalues to be determined. Solving equation (3.3) is an eigenvalue problem. The detailed procedures of solving equation (3.3) will be described in Section 3.6. I here give its solutions as follows:

$$f_n^{(j)}(z) = \sum_{l=1}^{2N+1} a_p^{(j)}(l,n) \exp\,[ik_l z], \tag{3.4a}$$

$$g_n^{(j)}(z) = \sum_{l=1}^{2N+1} a_s^{(j)}(l,n) \exp\,[ik_l z], \tag{3.4b}$$

where, $k_l = 2\pi(l - N - 1)/L$ is lth vertical wavenumber ($l = 1,2,\ldots,2N+1$); L is the periodic length (see Section 3.6); $\{a_p^{(j)}(l,n)\}$ and $\{a_s^{(j)}(l,n)\}$ are normalized by imposing the following constrains:

$$\int_{-L/2}^{L/2} \left\{f_n^{(j)}(z) f_m^{(j)^*}(z)\right\} dz = \delta_{nm}, \tag{3.5a}$$

$$\int_{-L/2}^{L/2} \left\{g_n^{(j)}(z) g_m^{(j)^*}(z)\right\} dz = \delta_{nm}. \tag{3.5b}$$

Substituting equation (3.2) into equation (3.1), we obtain

$$\sum_{n=1}^{2N+1}[\frac{d^2\tilde{\phi}_n^{(j)}(r)}{dr^2}+\frac{1}{r}\frac{d\tilde{\phi}_n^{(j)}(r)}{dr}+(\gamma_n^{(j)})^2\phi_n^{(j)}(r)]f_n^{(j)}(z)=F(\omega)\frac{\delta(r)\delta(z-z_s)}{(\lambda^{(j)}+2\mu^{(j)})\pi r}, \tag{3.6a}$$

$$\sum_{n=1}^{2N+1}[\frac{d^2\tilde{\psi}_n^{(j)}(r)}{dr^2}+\frac{1}{r}\frac{d\tilde{\psi}_n^{(j)}(r)}{dr}-\frac{\tilde{\psi}_n^{(j)}(r)}{r^2}+(\nu_n^{(j)})^2\tilde{\psi}_n^{(j)}(r)]g_n^{(j)}(z)=0\ . \tag{3.6b}$$

Multiplying $f_n^{(j)^*}$ on the both sides of equation 3.6, integrating from -*L*/2 to +*L*/2, and using equation(3.5), we obtain

$$\frac{d^2\tilde{\phi}_n^{(j)}(r)}{dr^2}+\frac{1}{r}\frac{d\tilde{\phi}_n^{(j)}(r)}{dr}+(\gamma_n^{(j)})^2\phi_n^{(j)}(r)=F(\omega)\frac{\delta(r)f_n^{(1)^*}(z_s)}{(\lambda^{(j)}+2\mu^{(j)})\pi r}, \tag{3.7a}$$

$$\frac{d^2\tilde{\psi}_n^{(j)}(r)}{dr^2}+\frac{1}{r}\frac{d\tilde{\psi}_n^{(j)}(r)}{dr}-\frac{\tilde{\psi}_n^{(j)}(r)}{r^2}+(\nu_n^{(j)})^2\tilde{\psi}_n^{(j)}(r)=0, \tag{3.7b}$$

where sign "*" denotes conjugate. The general solutions of equation (3.7) are

$$\tilde{\phi}_n^{(j)}=c_{p+}^{(j)}(n)H_o^{(1)}(\gamma_n^{(j)}r)+c_{p-}^{(j)}(n)H_o^{(2)}(\gamma_n^{(j)}r), \tag{3.8a}$$

$$\tilde{\psi}_n^{(j)}=c_{s+}^{(j)}(n)H_1^{(1)}(\nu_n^{(j)}r)+c_{s-}^{(j)}(n)H_1^{(2)}(\nu_n^{(j)}r), \tag{3.8b}$$

for $j > 1$, and

$$\tilde{\phi}_n^{(1)}=c^{(1)}(n)J_o(\gamma_n^{(1)}r)-\frac{iF(\omega)}{4(\lambda^{(1)}+2\mu^{(1)})\pi}f_n^{(1)^*}H_o^{(1)}(\gamma_n^{(j)}r), \tag{3.8c}$$

$$\tilde{\psi}_n^{(1)}=0\ , \tag{3.8d}$$

for *j* = 1 (fluid layer). Here, sign "+" refers to the wave going outward, and "-" refers to the wave coming inward. Coefficients $a_p^{(j)}(l,n)$ and $a_s^{(j)}(l,n)$ are orthonormal eigenvectors corresponding to eigenvalues $\gamma_n^{(j)}$ and $\nu_n^{(j)}$, respectively, and are given in Section 3.6. Coefficients $c_{p\pm}$ and $c_{s\pm}$ are determined by imposing boundary conditions at $r = r^{(j)}$, *j*=1,2, ..., *J*. Using these potential solutions, we can obtain the displacements and stresses in solid cylindrical layers (*j* > 1) as,

$$\begin{aligned}\hat{u}_r^{(j)}(r,z) &= \frac{\partial \hat{\phi}^{(j)}(r,z)}{\partial r} - \frac{\partial \hat{\psi}^{(j)}(r,z)}{\partial z} \\ &= \sum_{n=1}^{2N+1} \sum_{l=1}^{2N+1} [E_{11}^{(j)}(r;l,n)c_{p-}^{(j)}(n) + E_{12}^{(j)}(r;l,n)c_{s-}^{(j)}(n) \\ &\qquad + E_{13}^{(j)}(r;l,n)c_{p+}^{(j)}(n) + E_{14}^{(j)}(r;l,n)c_{s+}^{(j)}(n)] \exp(ik_l z)\,,\end{aligned} \tag{3.9a}$$

$$\begin{aligned}\hat{u}_z^{(j)}(r,z) &= \frac{\partial \hat{\phi}^{(j)}(r,z)}{\partial z} + \frac{1}{r}\frac{\partial [r\hat{\psi}^{(j)}(r,z)]}{\partial r} \\ &= \sum_{n=1}^{2N+1} \sum_{l=1}^{2N+1} [E_{21}^{(j)}(r;l,n)c_{p-}^{(j)}(n) + E_{22}^{(j)}(r;l,n)c_{s-}^{(j)}(n) \\ &\qquad + E_{23}^{(j)}(r;l,n)c_{p+}^{(j)}(n) + E_{24}^{(j)}(r;l,n)c_{s+}^{(j)}(n)] \exp(ik_l z)\,,\end{aligned} \tag{3.9b}$$

$$\begin{aligned}\hat{\sigma}^{(j)}(r,z) &= \lambda^{(j)}(z)\nabla^2 \hat{\phi}^{(1)}(r,z) + 2\mu^{(j)}(z)[\frac{\partial^2 \hat{\phi}^{(j)}}{\partial r^2} - \frac{\partial^2 \hat{\psi}^{(j)}}{\partial r \partial z}] \\ &= \sum_{n=1}^{2N+1} \sum_{l=1}^{2N+1} [E_{31}^{(j)}(r;l,n)c_{p-}^{(j)}(n) + E_{32}^{(j)}(r;l,n)c_{s-}^{(j)}(n) \\ &\qquad + E_{33}^{(j)}(r;l,n)c_{p+}^{(j)}(n) + E_{34}^{(j)}(r;l,n)c_{s+}^{(j)}(n)] \exp(ik_l z)\,,\end{aligned} \tag{3.9c}$$

$$\begin{aligned}\hat{\tau}^{(j)}(r,z) &= \mu^{(j)}(z)\{2\frac{\partial^2 \hat{\phi}^{(j)}}{\partial r \partial z} + \frac{\partial}{\partial r}[\frac{1}{r}\frac{\partial (r\hat{\psi}^{(j)})}{\partial r}] - \frac{\partial^2 \hat{\psi}^{(j)}}{\partial z^2}\} \\ &= \sum_{n=1}^{2N+1} \sum_{l=1}^{2N+1} [E_{41}^{(j)}(r;l,n)c_{p-}^{(j)}(n) + E_{42}^{(j)}(r;l,n)c_{s-}^{(j)}(n) \\ &\qquad + E_{43}^{(j)}(r;l,n)c_{p+}^{(j)}(n) + E_{44}^{(j)}(r;l,n)c_{s+}^{(j)}(n)] \exp(ik_l z)\,,\end{aligned} \tag{3.9d}$$

where $\{E_{pq}^{(j)}(r;l,n)$; p, q = 1, 2, 3, 4} are given in the Appendix B-1.

In the fluid-filled borehole (j=1), the displacements and stresses are

$$\tilde{u}_r^{(1)}(r,z)=\frac{\partial\tilde{\phi}^{(1)}(r,z)}{\partial r}$$
$$=\sum_{n=1}^{2N+1}\sum_{l=1}^{2N+1}\left\{E_{11}^{(1)}(r;l,n)c_{p-}^{(1)}(n)+E_{12}^{(1)}(r;l,n)[c_{p+}^{(1)}(n)+s_+(n)]\right\}\exp(ik_lz)\,, \tag{3.10a}$$

$$\tilde{u}_z^{(1)}(r,z)=\frac{\partial\tilde{\phi}^{(1)}(r,z)}{\partial z}$$
$$=\sum_{n=1}^{2N+1}\sum_{l=1}^{2N+1}\left\{E_{21}^{(1)}(r;l,n)c_{p-}^{(1)}(n)+E_{22}^{(1)}(r;l,n)[c_{p+}^{(1)}(n)+s_+(n)]\right\}\exp(ik_lz)\,, \tag{3.10b}$$

$$\tilde{\sigma}^{(1)}(r,z)=\lambda^{(1)}(z)\nabla^2\tilde{\phi}^{(1)}(r,z)$$
$$=\sum_{n=1}^{2N+1}\sum_{l=1}^{2N+1}\left\{E_{31}^{(1)}(r;l,n)c_{p-}^{(1)}(n)+E_{32}^{(1)}(r;l,n)[c_{p+}^{(1)}(n)+s_+(n)]\right\}\exp(ik_lz)\,, \tag{3.10c}$$

$$\tilde{\tau}^{(1)}(r,z)=0\,, \tag{3.10d}$$

with

$$s_+(n)=-\frac{i}{4(\lambda^{(1)}+2\mu^{(1)})}F(\omega)f_n^{(1)^*}(z_s)\,,$$

where, and $\{E_{pq}^{(1)}(r;l,n)$; p=1,2,3 and q=1,2} are given in the Appendix B-1. There are totally 4x(J+1)x(2N+1) unknown coefficients $c_{p\pm}^{(j)}(n)$ and $c_{s\pm}^{(j)}(n)$, which are determined by imposing boundary conditions at $r=r^{(j)}$, j=1, 2, ..., J .

It has been demonstrated in Chapter 2 that the generalized reflection and transmission (R/T) coefficients method is an effective tool for solving the problem of elastic wave propagation and excitation in cylindrically layered medium. In this chapter, the generalized R/T coefficients method is further developed to solve wave propagation problem in a complex radially symmetric medium. It should be pointed out that in the radially layered medium case studied in Chapter 2, all cylindrical layers are homogeneous which leads the vertical component of wavenumber to be conserved for all cylindrical layers, i.e., there is no coupling among different vertical wavenumbers. Thus the wave field can be solved separately for each single vertical wave-number. In the complex radially symmetric medium case, however, the radially layers generally are heterogeneous in vertical direction, so that there exists coupling among different vertical wave-numbers. Consequently, the corresponding wave field must be solved simultaneously for all vertical wave-numbers, and larger reflection and transmission matrices must be introduced to describe such coupling process. Thus, much larger memory and longer time are needed than the radially layered medium case when computing the wave field.

3.3 REFLECTION AND TRANSMISSION MATRICES

For the *j*-th interface $r = r^{(j)}$, the reflection and transmission (R/T) matrices, $\mathbf{R}_{-+}^{(j)}$, $\mathbf{R}_{+-}^{(j)}$, $\mathbf{T}_{+}^{(j)}$ and $\mathbf{T}_{-}^{(j)}$, are defined through relations

$$\begin{cases} \mathbf{C}_{+}^{(j+1)} = \mathbf{T}_{+}^{(j)}\mathbf{C}_{+}^{(j)} + \mathbf{R}_{-+}^{(j)}\mathbf{C}_{-}^{(j+1)} \\ \mathbf{C}_{-}^{(j)} = \mathbf{R}_{+-}^{(j)}\mathbf{C}_{+}^{(j)} + \mathbf{T}_{-}^{(j)}\mathbf{C}_{-}^{(j+1)} \end{cases} \qquad \text{for } j>1, \qquad (3.11\text{a})$$

where, $\mathbf{C}_{\pm}^{(j)} = [c_{p\pm}^{(j)}(1),\ c_{p\pm}^{(j)}(2),\ \ldots,\ c_{p\pm}^{(j)}(2N+1),\ c_{s\pm}^{(j)}(1),\ c_{s\pm}^{(j)}(2)\ \ldots\ c_{s\pm}^{(j)}(2N+1)]^T$ is a vector with (4*N*+2) elements; $\mathbf{T}_{+}^{(j)}$, $\mathbf{T}_{-}^{(j)}$, $\mathbf{R}_{-+}^{(j)}$ and $\mathbf{R}_{+-}^{(j)}$ are (4*N*+2)x(4*N*+2) matrices. Equation (3.11a) looks like equation (2.12a), but the matrices in these two equations have much different dimensions. Moreover, $\mathbf{R}_{-+}^{(j)}$, $\mathbf{R}_{+-}^{(j)}$, $\mathbf{T}_{+}^{(j)}$ and $\mathbf{T}_{-}^{(j)}$ in equation (3.11a) are ordinary R/T matrices, because there are no normalization factors in this formulation. For the liquid-solid boundary (*j*=1), the R/T matrices are defined by

$$\begin{cases} \mathbf{C}_{+}^{(2)} = \mathbf{T}_{+}^{(1)}(\mathbf{C}_{+}^{(1)} + \mathbf{s}_{+}) + \mathbf{R}_{-+}^{(1)}\mathbf{C}_{-}^{(2)} \\ \mathbf{C}_{-}^{(1)} = \mathbf{R}_{+-}^{(1)}(\mathbf{C}_{+}^{(1)} + \mathbf{s}_{+}) + \mathbf{T}_{-}^{(1)}\mathbf{C}_{-}^{(2)} \end{cases}, \tag{3.11b}$$

where, $\mathbf{C}_{\pm}^{(1)} = [c_{p\pm}^{(1)}(1),\ c_{p\pm}^{(1)}(2),\ldots,\ c_{p\pm}^{(1)}(2N+1)]^{T}$ is a vector with (2*N*+1) elements; $\mathbf{T}_{-}^{(1)}$, $\mathbf{T}_{+}^{(1)}$, $\mathbf{R}_{+-}^{(1)}$ and $\mathbf{R}_{-+}^{(1)}$ are (2*N*+1)x(4*N*+2), (4*N*+2)x(2*N*+1), (2*N*+1)x(2*N*+1) and (4*N*+2)x(4*N*+2) matrices, respectively. These R/T matrices for *j*=1, 2, ..., *J* can be determined by imposing the boundary conditions at each radial boundary $r = r^{(j)}$.

The continuous conditions of displacements and stresses at a solid-solid interface $r = r^{(j)}$ (*j*>1) are:

$$\tilde{u}_{r}^{(j)}(r^{(j)}, z) = \tilde{u}_{r}^{(j+1)}(r^{(j)}, z), \tag{3.12a}$$

$$\tilde{u}_{z}^{(j)}(r^{(j)}, z) = \tilde{u}_{z}^{(j+1)}(r^{(j)}, z), \tag{3.12b}$$

$$\tilde{\sigma}^{(j)}(r^{(j)}, z) = \tilde{\sigma}^{(j+1)}(r^{(j)}, z), \tag{3.12c}$$

$$\tilde{\tau}^{(j)}(r^{(j)}, z) = \tilde{\tau}^{(j+1)}(r^{(j)}, z)\ . \tag{3.12d}$$

Substituting equation (3.9) into equation (3.12) and operating $\int_{-L/2}^{+L/2} \exp(-ik_{l}z)\,dz$ on both sides, we obtain

$$\begin{bmatrix} \mathbf{D}_{11}^{(j)} & \mathbf{D}_{12}^{(j)} \\ \mathbf{D}_{21}^{(j)} & \mathbf{D}_{22}^{(j)} \end{bmatrix} \begin{bmatrix} \mathbf{C}_{-}^{(j)} \\ \mathbf{C}_{+}^{(j)} \end{bmatrix} = \begin{bmatrix} \mathbf{D}_{11}^{(j+1)} & \mathbf{D}_{12}^{(j+1)} \\ \mathbf{D}_{21}^{(j+1)} & \mathbf{D}_{22}^{(j+1)} \end{bmatrix} \begin{bmatrix} \mathbf{C}_{-}^{(j+1)} \\ \mathbf{C}_{+}^{(j+1)} \end{bmatrix}; \tag{3.13}$$

where

$$\mathbf{D}_{11}^{(j)} = \begin{bmatrix} \mathbf{E}_{11}^{(j)} & \mathbf{E}_{12}^{(j)} \\ \mathbf{E}_{21}^{(j)} & \mathbf{E}_{22}^{(j)} \end{bmatrix}, \qquad \mathbf{D}_{12}^{(j)} = \begin{bmatrix} \mathbf{E}_{13}^{(j)} & \mathbf{E}_{14}^{(j)} \\ \mathbf{E}_{23}^{(j)} & \mathbf{E}_{24}^{(j)} \end{bmatrix},$$

$$\mathbf{D}_{21}^{(j)} = \begin{bmatrix} \mathbf{E}_{31}^{(j)} & \mathbf{E}_{32}^{(j)} \\ \mathbf{E}_{41}^{(j)} & \mathbf{E}_{42}^{(j)} \end{bmatrix}, \qquad \mathbf{D}_{22}^{(j)} = \begin{bmatrix} \mathbf{E}_{33}^{(j)} & \mathbf{E}_{34}^{(j)} \\ \mathbf{E}_{43}^{(j)} & \mathbf{E}_{44}^{(j)} \end{bmatrix};$$

$\mathbf{E}_{pq}^{(j)} = \left\{ E_{pq}^{(j)}(r^{(j)}; m, n) \mid m, n = 1, 2, \ldots, 2N+1 \right\}$, and $\mathbf{E}_{pq}^{(j+1)} = \left\{ E_{pq}^{(j+1)}(r^{(j)}; m, n) \mid m, n = 1, 2, \ldots, 2N+1 \right\}$ are (2N+1)x(2N+1) matrices. Comparing equations (3.11a) and (3.13) we can obtain (see Appendix B-2)

$$\begin{bmatrix} \mathbf{R}_{+-}^{(j)} & \mathbf{T}_{-}^{(j)} \\ \mathbf{T}_{+}^{(j)} & \mathbf{R}_{-+}^{(j)} \end{bmatrix} = \begin{bmatrix} \mathbf{E}_{11}^{(j)} & \mathbf{E}_{12}^{(j)} & -\mathbf{E}_{13}^{(j+1)} & -\mathbf{E}_{14}^{(j+1)} \\ \mathbf{E}_{21}^{(j)} & \mathbf{E}_{22}^{(j)} & -\mathbf{E}_{23}^{(j+1)} & -\mathbf{E}_{24}^{(j+1)} \\ \mathbf{E}_{31}^{(j)} & \mathbf{E}_{32}^{(j)} & -\mathbf{E}_{33}^{(j+1)} & -\mathbf{E}_{34}^{(j+1)} \\ \mathbf{E}_{41}^{(j)} & \mathbf{E}_{42}^{(j)} & -\mathbf{E}_{43}^{(j+1)} & -\mathbf{E}_{44}^{(j+1)} \end{bmatrix}^{-1} \begin{bmatrix} -\mathbf{E}_{13}^{(j)} & -\mathbf{E}_{14}^{(j)} & \mathbf{E}_{11}^{(j+1)} & \mathbf{E}_{12}^{(j+1)} \\ -\mathbf{E}_{23}^{(j)} & -\mathbf{E}_{24}^{(j)} & \mathbf{E}_{21}^{(j+1)} & \mathbf{E}_{22}^{(j+1)} \\ -\mathbf{E}_{33}^{(j)} & -\mathbf{E}_{34}^{(j)} & \mathbf{E}_{31}^{(j+1)} & \mathbf{E}_{32}^{(j+1)} \\ -\mathbf{E}_{43}^{(j)} & -\mathbf{E}_{44}^{(j)} & \mathbf{E}_{41}^{(j+1)} & \mathbf{E}_{42}^{(j+1)} \end{bmatrix}_{r = r^{(j)}}, \tag{3.14}$$

for *j*>1. The boundary conditions at liquid-solid interface $r = r^{(1)}$ are

$$\tilde{u}_r^{(1)}(r^{(1)}, z) = \tilde{u}_r^{(2)}(r^{(1)}, z) \tag{3.15a}$$

$$\tilde{\sigma}^{(1)}(r^{(1)}, z) = \tilde{\sigma}^{(2)}(r^{(1)}, z) \tag{3.15b}$$

$$0 = \tilde{\tau}^{(2)}(r^{(1)}, z) \tag{3.15c}$$

Similarly, using equations (3.10), (3.11b) and (3.15) we obtain the reflection and transmission matrices for the first layer as

$$\begin{bmatrix} \mathbf{R}_{+-}^{(1)} & \mathbf{T}_{-}^{(1)} \\ \mathbf{T}_{+}^{(1)} & \mathbf{R}_{-+}^{(1)} \end{bmatrix} = \begin{bmatrix} \mathbf{E}_{11}^{(1)} & -\mathbf{E}_{13}^{(2)} & -\mathbf{E}_{14}^{(2)} \\ \mathbf{E}_{31}^{(1)} & -\mathbf{E}_{33}^{(2)} & -\mathbf{E}_{34}^{(2)} \\ \mathbf{0} & -\mathbf{E}_{43}^{(2)} & -\mathbf{E}_{44}^{(2)} \end{bmatrix}^{-1} \begin{bmatrix} -\mathbf{E}_{13}^{(1)} & \mathbf{E}_{11}^{(2)} & \mathbf{E}_{12}^{(2)} \\ -\mathbf{E}_{33}^{(1)} & \mathbf{E}_{31}^{(2)} & \mathbf{E}_{32}^{(2)} \\ \mathbf{0} & \mathbf{E}_{41}^{(2)} & \mathbf{E}_{42}^{(2)} \end{bmatrix}_{r = r^{(1)}}. \tag{3.16}$$

3.4 GENERALIZED REFLECTION AND TRANSMISSION MATRICES

The generalized reflection and transmission matrices, $\overset{?}{\mathbf{R}}{}_{+-}^{(j)}$ and $\overset{?}{\mathbf{T}}{}_{+}^{(j)}$, are introduced via relations

$$\begin{cases} \mathbf{C}_{+}^{(j+1)} = \overset{?}{\mathbf{T}}{}_{+}^{(j)}\mathbf{C}_{+}^{(j)} \\ \mathbf{C}_{-}^{(j)} = \overset{?}{\mathbf{R}}{}_{+-}^{(j)}\mathbf{C}_{+}^{(j)} \end{cases}, \tag{3.17a}$$

for $j>1$, and

$$\begin{cases} \mathbf{C}_{+}^{(2)} = \overset{?}{\mathbf{T}}{}_{+}^{(1)}(\mathbf{C}_{+}^{(1)} + \mathbf{s}_{+}) \\ \mathbf{C}_{-}^{(1)} = \overset{?}{\mathbf{R}}{}_{+-}^{(1)}(\mathbf{C}_{+}^{(1)} + \mathbf{s}_{+}) \end{cases} \tag{3.17b}$$

for $j=1$. The generalized R/T matrices describe the overall reflections and transmissions at an interface (see Figure 2.3 for the pictorial explanation). Substituting equation (3.17) into equation (3.11) and rearranging terms, we obtain a recursive relation (see Appendix B-3):

$$\begin{cases} \overset{?}{\mathbf{T}}{}_{+}^{(j)} = [\mathbf{I} - \mathbf{R}_{-+}^{(j)}\overset{?}{\mathbf{R}}{}_{+-}^{(j+1)}]^{-1}\mathbf{T}_{+}^{(j)} \\ \overset{?}{\mathbf{R}}{}_{+-}^{(j)} = \mathbf{R}_{+-}^{(j)} + \mathbf{T}_{-}^{(j)}\overset{?}{\mathbf{R}}{}_{+-}^{(j+1)}\overset{?}{\mathbf{T}}{}_{+}^{(j)} \end{cases}, \qquad \text{for } j = N, N\text{-}1, \ldots, 2, 1, \tag{3.18}$$

where **I** is the unit matrix, $\overset{?}{\mathbf{R}}{}_{+-}^{(j)}$ and $\overset{?}{\mathbf{T}}{}_{+}^{(j)}$ are (4*N*+2)x(4*N*+2) matrices (for $j > 1$), $\overset{?}{\mathbf{T}}{}_{+}^{(1)}$ is a (4*N*+2)x(2*N*+1) matrix, and $\overset{?}{\mathbf{R}}{}_{+-}^{(1)}$ is a (2*N*+1)x(2*N*+1) matrix. In the outer most layer ($j = N+1$), there exist only outward-going waves, i.e., $\mathbf{C}_{-}^{(N+1)} = \mathbf{0}$. Therefore, the initial condition for the iteration is

$$\overset{?}{\mathbf{R}}{}_{+-}^{(N+1)} = \mathbf{0}\ . \tag{3.19}$$

Using equation (3.18) with initial condition (3.19), we can recursively calculate the generalized R/T matrices $\overset{?}{\mathbf{R}}{}^{(j)}_{+-}$ and $\overset{?}{\mathbf{T}}{}^{(j)}_{+}$ for all interfaces from reflection and transmission matrices $\mathbf{T}^{(j)}_{+}$, $\mathbf{T}^{(j)}_{-}$, $\mathbf{R}^{(j)}_{-+}$ and $\mathbf{R}^{(j)}_{+-}$ that are calculated by equations (3.14) and (3.16).

3.5 SOLUTION SYNTHESIS IN FREQUENCY DOMAIN

Using the generalized R/T matrices we can easily obtain the coefficient vectors $\mathbf{C}^{(j)}_{\pm}$. Inside the first layer (*j*=1) we have

$$\mathbf{C}^{(1)}_{+} = \mathbf{C}^{(1)}_{-}, \tag{3.20}$$

where the relation $J_o = \frac{1}{2}(H^{(2)}_o + H^{(1)}_o)$ is used. Substituting (3.20) into (3.17b) yields

$$\mathbf{C}^{(1)}_{+} + \mathbf{s}_{+} = (\mathbf{I} - \mathbf{R}^{(1)}_{+-})^{-1}\mathbf{s}_{+}\,. \tag{3.21}$$

Then, from (3.17a), (3.17b) and (3.21) we have

$$\begin{cases} \mathbf{C}^{(j)}_{+} = \overset{?}{\mathbf{T}}{}^{(j-1)}_{+}\overset{?}{\mathbf{T}}{}^{(j-2)}_{+}\ldots\overset{?}{\mathbf{T}}{}^{(1)}_{+}(\mathbf{I} - \overset{?}{\mathbf{R}}{}^{(1)}_{+-})^{-1}\mathbf{s}_{+} \\ \mathbf{C}^{(j)}_{-} = \overset{?}{\mathbf{R}}{}^{(j)}_{+-}\mathbf{C}^{(j)}_{+} \end{cases}. \tag{3.22}$$

Once having the coefficients $\mathbf{C}^{(j)}_{\pm}$ we can calculate the frequency domain solutions (displacements and stresses) using equations (3.9) and (3.10). The corresponding time domain solution can be obtained by performing inverse Fourier transform. The numerical implementation is given in Section 3.7 (also see Section 2.4.1).

3.6 DETERMINATION OF EIGEN FUNCTIONS

Let us now solve equation (3.3), namely, determine the eigenvalues $\{\gamma_n^{(j)},\ \nu_n^{(j)}\}$ in equation (3.3) and eigenvectors $\{a_p^{(j)}(l,n),\ a_s^{(j)}(l,n)\}$ in equation (3.4). Substituting equation (3.4) into equation (3.3), we have

$$\sum_{l=1}^{2N+1} \{-(k_l)^2 + [k_\alpha^{(j)}(z)]^2 - (\gamma_n^{(j)})^2\} a_p^{(j)}(l,n) \exp(ik_l z) = 0 , \tag{3.23a}$$

$$\sum_{l=1}^{2N+1} \{-(k_l)^2 + [k_\beta^{(j)}(z)]^2 - (\nu_n^{(j)})^2\} a_s^{(j)}(l,n) \exp(ik_l z) = 0 . \tag{3.23b}$$

To solve this eigenvalue problem, I assume that the vertically heterogeneity of each cylinder can be described by Fourier series as

$$[k_\alpha^{(j)}(z)]^2 \approx \frac{1}{2\pi} \sum_{m=1}^{2N+1} w_\alpha^{(j)}(m) \exp(ik_m z) , \tag{3.24a}$$

$$[k_\beta^{(j)}(z)]^2 \approx \frac{1}{2\pi} \sum_{m=1}^{2N+1} w_\beta^{(j)}(m) \exp(ik_m z) , \tag{3.24b}$$

with

$$w_\alpha^{(j)}(m) = \int_{-L/2}^{+L/2} [k_\alpha^{(j)}(z)]^2 \exp(-ik_m z)\, dz , \tag{3.25a}$$

$$w_\beta^{(j)}(m) = \int_{-L/2}^{+L/2} [k_\beta^{(j)}(z)]^2 \exp(-ik_m z)\, dz . \tag{3.25b}$$

Here, $k_l = 2\pi(l - N - 1)/L = \Delta k(l - N - 1)$, and $L = z_M - z_o$ is the periodic length that is as the distance between two artificial boundaries (see Figure 3.2). L should be large enough (or the increment Δk is small enough) so that the reflections from these artificial boundaries are out of the time window. Equation (3.23) can be rewritten as the following compact matrix forms:

$$\begin{cases} [\mathbf{A}^{(j)} - (\gamma_n^{(j)})^2 \mathbf{I}]\mathbf{a}_p^{(j)}(n) = 0 \\ [\mathbf{B}^{(j)} - (\nu_n^{(j)})^2 \mathbf{I}]\mathbf{a}_s^{(j)}(n) = 0 \end{cases} \tag{3.26}$$

where,

$$\mathbf{a}_p^{(j)}(n) = [a_p^{(j)}(1,n), a_p^{(j)}(2,n), \ldots, a_p^{(j)}(2N+1,n)]^T ,$$

$$\mathbf{a}_s^{(j)}(n) = [a_s^{(j)}(1,n), a_s^{(j)}(2,n), \ldots, a_s^{(j)}(2N+1,n)]^T ,$$

$$A_{ml}^{(j)} = -(k_m)^2 \delta_{lm} + w_\alpha^{(j)}(m-l) ,$$

$$B_{ml}^{(j)} = -(k_m)^2 \delta_{lm} + w_\beta^{(j)}(m-l) .$$

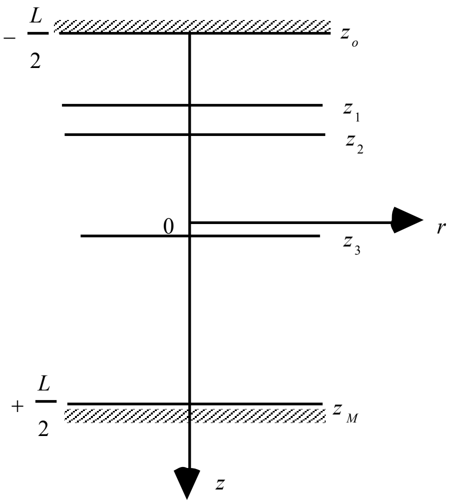

Figure 3.2 A model of vertically layered media. In order to treat it as an eigenvalue problem, two artificial boundaries at z_o and z_M are added.

Eigenvalues $(\gamma_n^{(j)})^2$ and $(\nu_n^{(j)})^2$, and the corresponded eigenvectors $\mathbf{a}_p^{(j)}(n)$ and $\mathbf{a}_s^{(j)}(n)$ in equation (2.26) can be calculated by using standard linear algebra programs, for example, LAPACK.

If there are M horizontal vertical layers, and $k_{\alpha_p}^{(j)}(z) = k_{\alpha_p}^{(j)}$ and $k_{\beta_p}^{(j)}(z) = k_{\beta_p}^{(j)}$ are constant for $z_p^{(j-1)} < z < z_p^{(j)}$, $p = 1, 2, \ldots, M$), then equation (3.25) can be written as

$$w_\alpha^{(j)}(m - l) = 2\sum_{p=1}^{M} (k_{\alpha_p}^{(j)})^2 e^{i(k_l - k_m)(z_{p-1} + d_p)} \frac{\sin[(k_l - k_m) d_p]}{k_l - k_m}, \tag{3.28a}$$

$$w_\beta^{(j)}(m - l) = 2\sum_{p=1}^{M} (k_{\beta_p}^{(j)})^2 e^{i(k_l - k_m)(z_{p-1} + d_p)} \frac{\sin[(k_l - k_m) d_p]}{k_l - k_m}, \tag{3.28b}$$

where $d_p = (z_p - z_{p-1})/2$. It should be pointed out that solutions above are obtained based on Fourier series expansion given in equation (3.24). When the vertical heterogeneity is continuous, the solutions are precise. Otherwise, if there is discontinuity in the vertical direction, the solutions are approximated, i.e., the *P-S* and *S-P* conversions at *horizontal* interfaces may not be included in this case. This is a major limitation of this method.

3.7 IMPLEMENTATION AND VALIDATIONS

The discrete wavenumber method is used for implementation (Section 2.4.1 of this thesis; Bouchon & Aki, 1977; Chen, 1991). In the numerical computation, the following criteria are applied to select the parameters: $k_{\max} > 1.5\,|\omega|/V_{\min}$, $L > T_{\max} V_{\max}$, $\Delta k = 2\pi / L$ and $k_m = -k_{\max} + m\Delta k$, $\omega_I = \pi / T_{\max}$, where $k_{\max}$ is the upper limit of wavenumber *k* in equations (3.9), (3.10) and (3.24); *L* is the periodic length or the distance of the two artificial boundaries; Δk is the increment of wavenumber; $T_{\max}$ is the trace length of a seismogram; $V_{\min}$ is the lowest velocity in a given model; and ω_I is the imaginary part of the frequency used in the discrete wavenumber method.

To examine the validity of this method, let us first consider an extreme case in which all cylindrical layers are homogeneous in the vertical direction. This problem has been well studied by several authors as summarized by Paillet and Cheng (1991). The more general algorithm in this chapter should provide an identical solution to the one which is directly solved for this special case (see Chapter 2). In fact, the more general solution obtained in this chapter can be analytically reduced to the solution directly derived for this extreme case in Chapter 2. Let $k_\alpha^{(j)}(z) = k_\alpha^{(j)}$ and $k_\beta^{(j)}(z) = k_\beta^{(j)}$ be constants, then from equations (3.25) and (3.26) we obtain

$$\begin{cases} (\gamma_n^{(j)})^2 = (k_\alpha^{(j)})^2 - k_n^2 \\ a_p^{(j)}(l,n) = \delta_{ln} \end{cases}, \tag{3.27a}$$

and

$$\begin{cases} (\nu_n^{(j)})^2 = (k_\beta^{(j)})^2 - k_n^2 \\ a_s^{(j)}(l,n) = \delta_{ln} \end{cases}. \tag{3.27b}$$

Substituting these special solutions into equations (3.9) and (3.10), we can obtain identical formulas with the solutions in Chapter 2.

Bouchon (1993) used the boundary element method to calculate an open borehole embedded in a layered medium. For comparison, I here use the generalized R/T matrices method to solve the same problem. Figure 3.4a shows the model configuration and parameters. The low velocity layer is 1 meter thick. The source is located 2 meters above the layer interface. The source function is a Ricker wavelet (equation 2.27) with peak frequency 1KHz. Figures 3.4b gives the seismograms calculated by the generalized R/T matrices method presented in this chapter. Figure 3.4c is taken from Bouchon (1993) for comparison. It can be seen that main features of Figures 3.4b and 3.4c are the same. Figure 3.4b (generalized R/T matrices method) seems have less numerical noise than Figure 3.4c (boundary element method), especially for the later arrivals. As mentioned earlier, if there is discontinuity in the vertical direction, the solution given in this chapter is approximated, i.e., the *P-S* and *S-P* conversions at horizontal interfaces are not included in this case. Considering this approximation, the agreement of the comparison is fair. The low velocity layer exhibits a significant influence on the wave field. The tube wave converts to *P* and *S* waves at the boundaries. The wave field within the low velocity zone is very complicated.

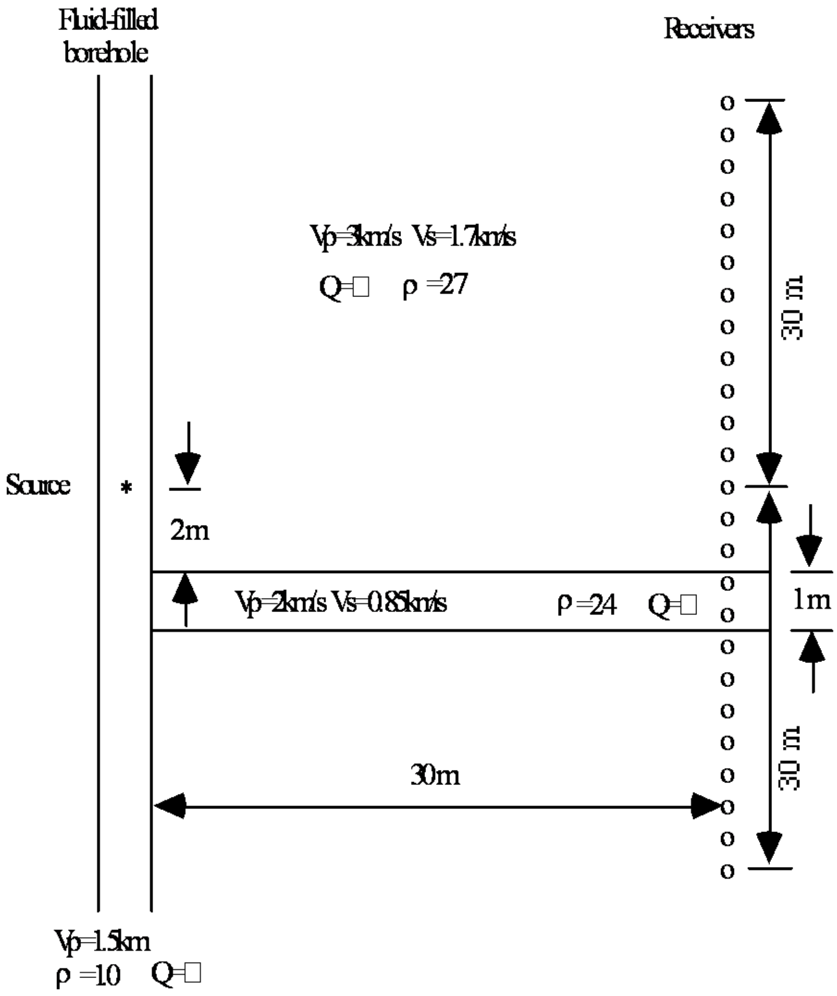

Figure. 3.4a Model geometry and parameters used for (b) and (c).

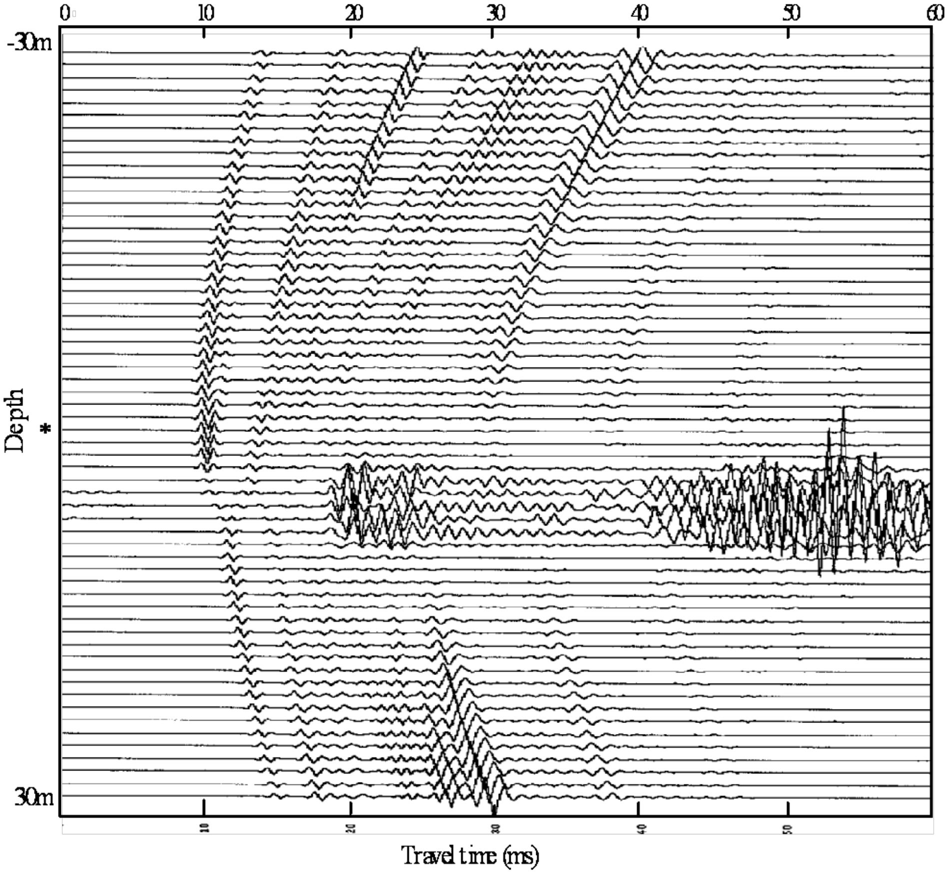

Figure 3.4b A common source gather of crosswell profiling calculated using the generalized R/T matrix method.

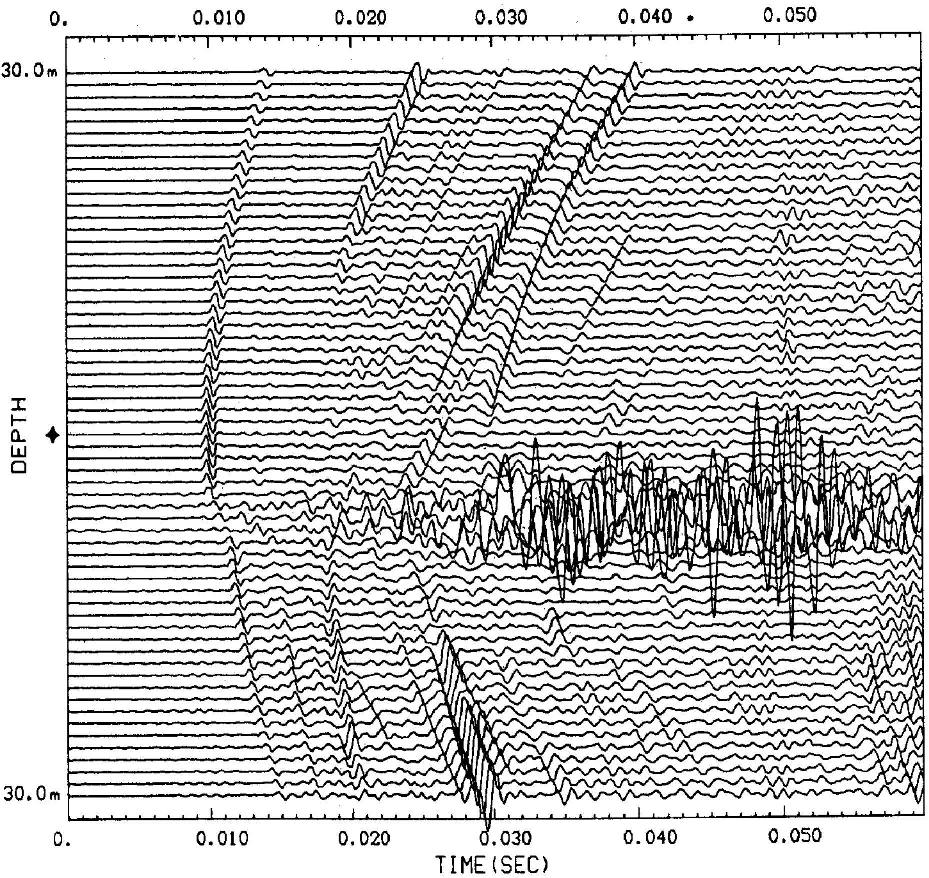

Figure 3.4c A common source gather of crosswell profiling calculated using the boundary element method. This is taken from Bouchon (1993) for comparison with (b).

3.8 EXAMPLES

In this section I present four examples to show the applicability of this method for various complex borehole-formation models. The first example simulates acoustic logging shown in Figure 3.5. There is a low velocity layer in the formation (see Figure

3.5b). Figure 3.5a shows the synthetic acoustic log. It can be seen that the moveout of the *P* and *S* waves changes when receivers pass through the interface. The change in the moveout indicates the location of the interface. This example shows that the source frequency can be up to 20 KHz (the peak frequency is 10 KHz) in the simulation. Source function is given by

$$F(\omega) = \frac{1}{\omega^2} \frac{8\alpha\omega_o(\alpha - i\omega)}{[(\alpha - i\omega)^2 + \omega_o^2]^2}$$

with $\omega_o = 2\pi \times$ 10 KHz and $\alpha = 0.5\omega_o / \pi$.

Figures 3.6–3.8 are crosswell profiling examples. In crosswell profiling, sources are located in a borehole, and receivers in another borehole. To remain the radial symmetry, only a source borehole is involved in this modeling method. Receivers are placed in the formation. If fixing a source and changing receiver locations, we obtain seismograms as a common source gather. To the contrary, if fixing a receiver and changing source locations, we obtain a common receiver gather. Wave events may exhibit very different appearances in different gathers. In these examples the seismograms are displacements of U_r component. Figures 3.6 and 3.7 are common source gathers. Figure 3.8 is a common receiver gather. To calculate a common receiver gather or a common source gather, the computing time only increases a little comparing with only calculating a single seismogram trace. The source function used in these examples is Ricker wavelet described by equation (2.27).

Figure 3.6 gives an example of cased borehole. A low velocity layer is placed in the casing to simulate tube conversions generated by a velocity anomaly (e.g., a joint or perforation) in a casing. Tube waves mainly propagate within a borehole, and their amplitudes exponentially decays as the distance increases from the borehole wall. However, when the tube waves reach a heterogeneity on the borehole wall, they can be converted into *P* and *S* waves. Tube waves to *P* and *S* wave conversions clearly show up in this example. Figure 3.6 also shows the radiation pattern due to a point source.

Figure 3.7 is a cased borehole embedded in a multi-layered formation. There are a low velocity layer and a high velocity layer. Though the low velocity zone is only 1 m thick, its effects, e.g., the guided wave, on the wave field can be clearly seen.

Figure 3.8 is a common receiver gather sorted from a complete synthetic crosswell data set. There are 50 sources and 50 receivers. Both of the source interval and receiver interval are 2 m. Sources are placed in a cased borehole. Tube waves are converted into body waves at an interface near the borehole. The moveout of the tube wave conversions in a common receiver gather is very different from that in a common source gather as shown in Figure 3.6. Such a synthetic data set can be used to test tomography techniques and other inversion methods. In Chapter 4, a similar synthetic data set is used to test seismic attenuation tomography.

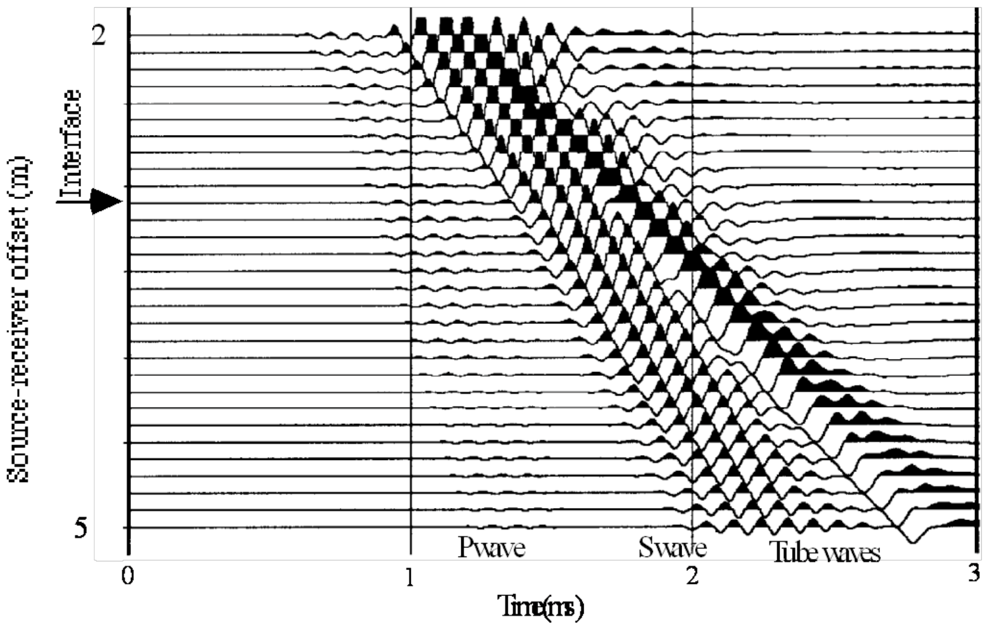

(a) Synthetic full waveform sonic log. The peak frequency of the source wavelet is 10 KHz.

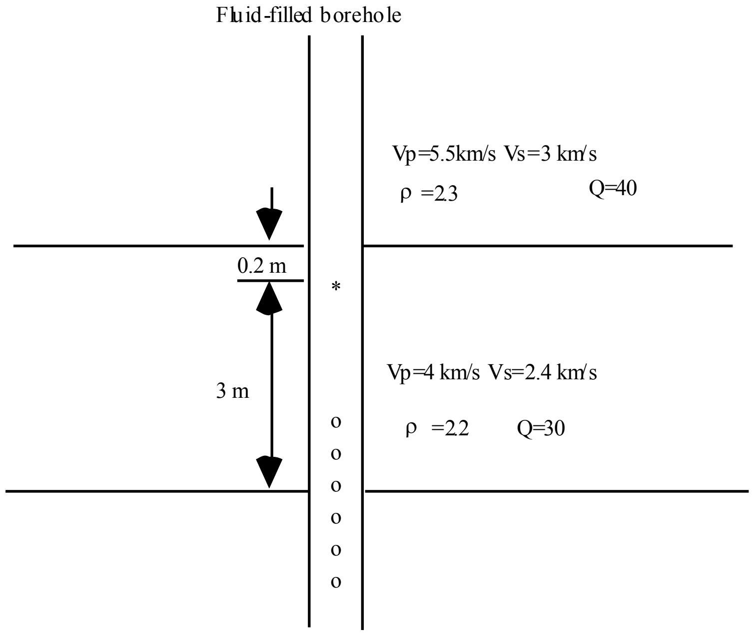

(b) Model used to calculate the sonic log shown in (a).

Figure 3.5 Simulation of acoustic logging in a layered medium.

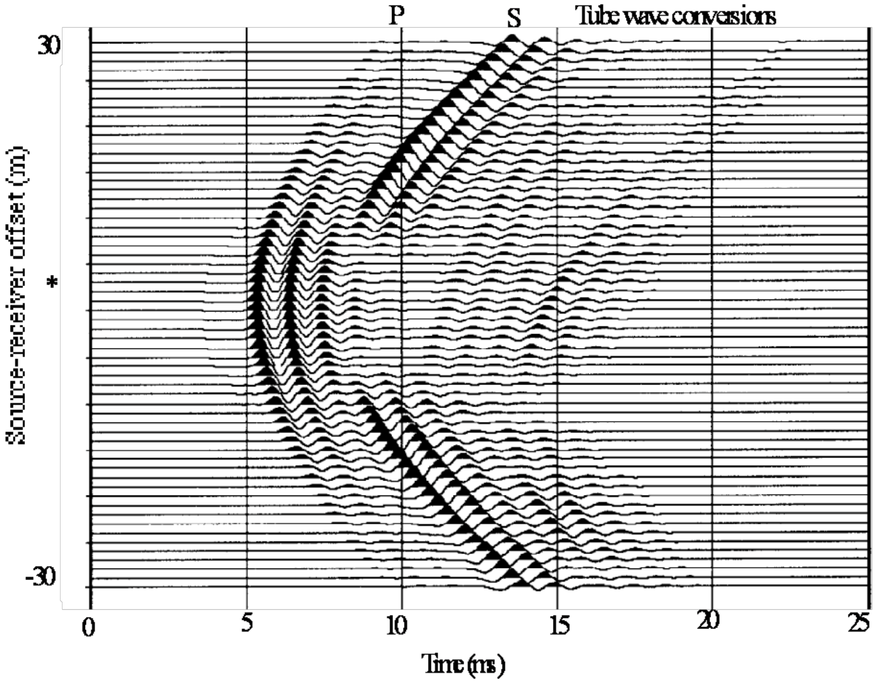

(a) Seismograms. The peak frequency of the source wavelet is 1 KHz.

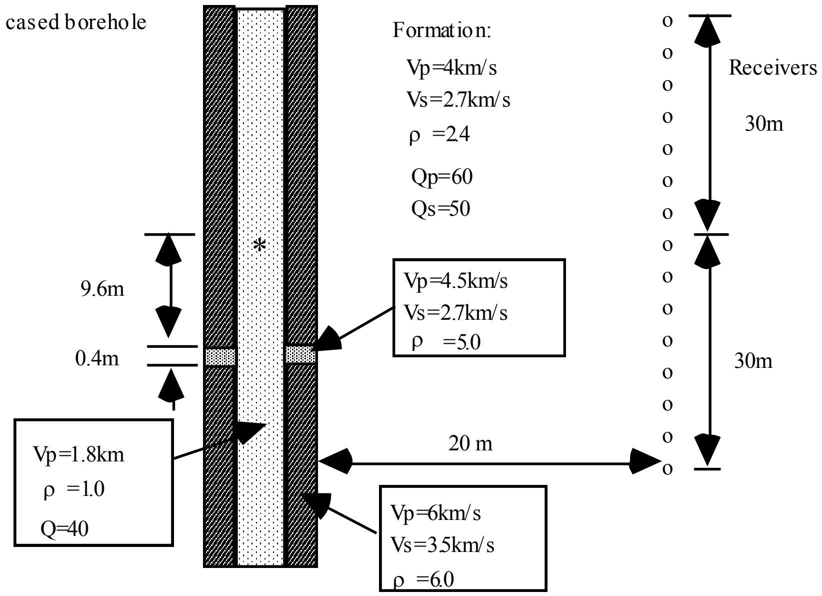

(b) Model geometry and parameters.

Figure 3.6 Test on the effect of a velocity anomaly in casing. It can be seen that the tube wave converts to *P* and *S* waves at a velocity anomaly.

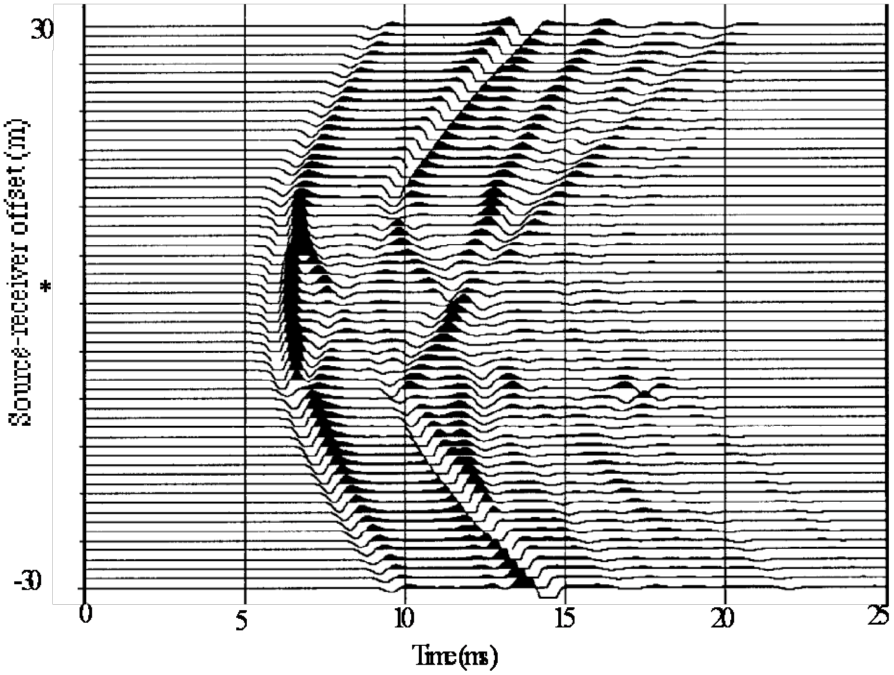

(a) Seismograms. The peak frequency of the source wavelet is 1 KHz.

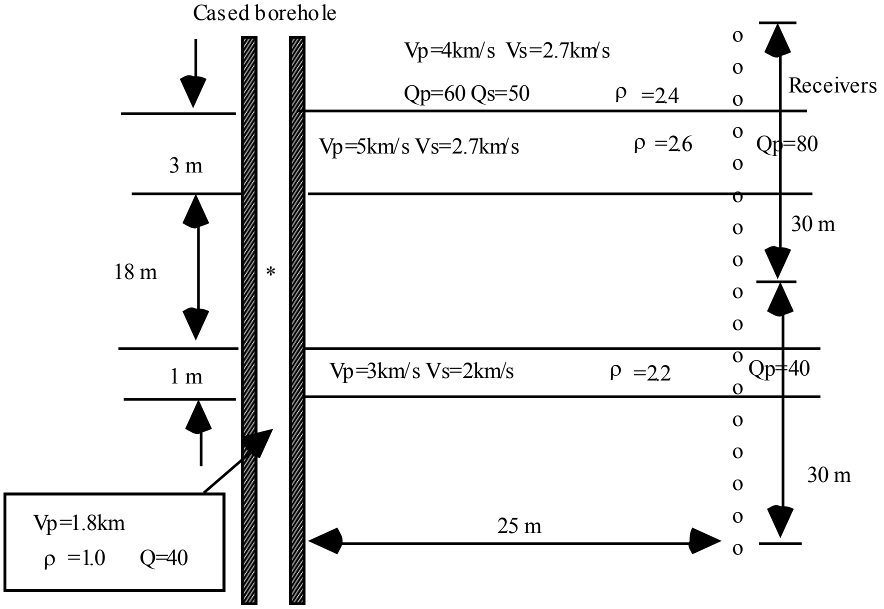

(b) Model geometry and parameters used for (a).

Figure 3.7 Simulation for a cased borehole embeds in a formation with multi-layers.

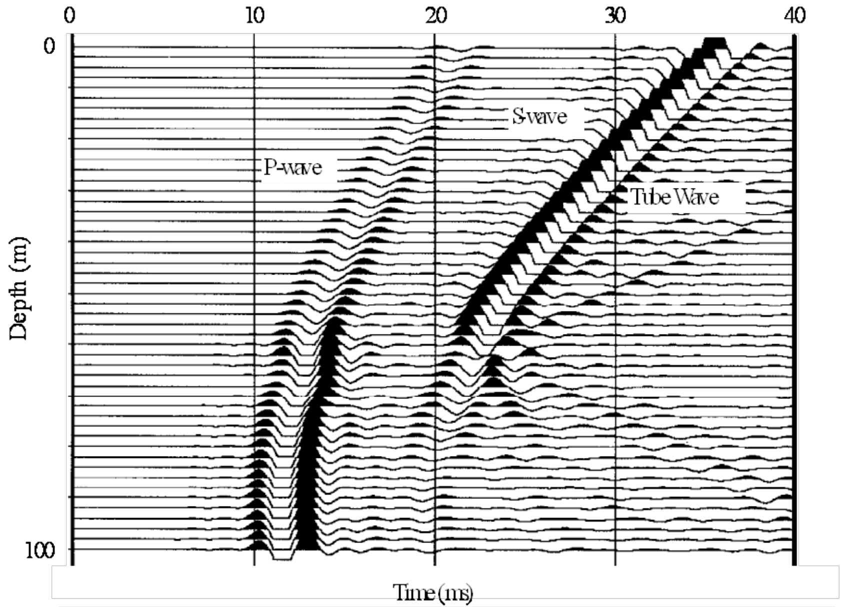

(a) seismograms. The peak frequency is 300 Hz

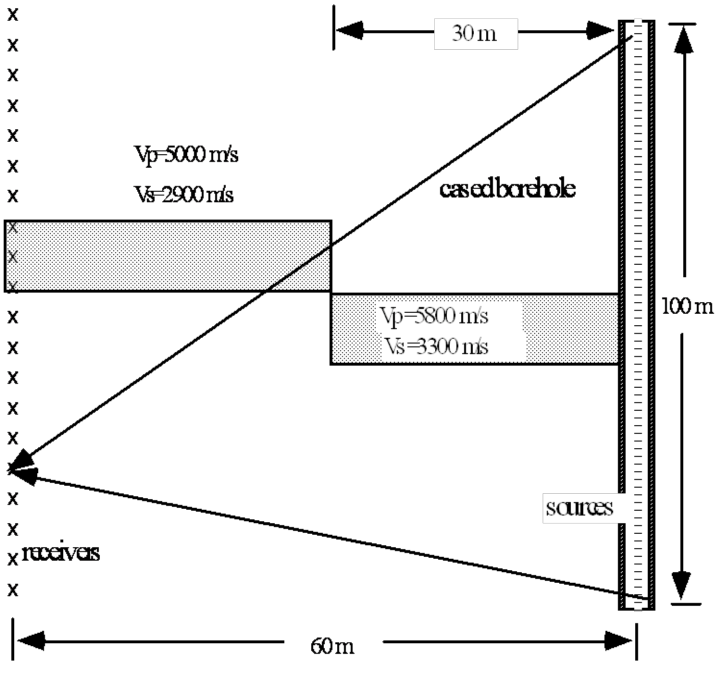

(b) Model geometry and parameters used for (a).

Figure 3.8 A common receiver gather sorted from a complete synthetic data set.

3.9 CONCLUSIONS

A semi-analytical approach is developed to simulate the waves in a complex borehole-formation model in which there exist both radial and vertical layers. In this approach, I first calculate the eigenfunctions of vertical layers for each cylindrical layer. Then, I expand the wave equation solutions into these eigenfunctions and apply the generalized reflection and transmission matrices method to solve the boundary problem for radial layers. Since we neglect the *P*-*S* and *S*-*P* conversions due to the *horizontal interfaces,* this approach is valid for the cases in which those conversions do not exist or are not important, for example, continuous or slow variation in vertical direction. It seems that direct waves are least affected by this *P*-*S*/*S*-*P* conversion problem.

Numerical examples show that this approach provides an effective tool to simulate complex models which are found in sonic logging and crosswell seismic profiling. This simulation method is especially useful for synthetic studies on crosswell profiling, because there is no difficulty to deal with the small borehole diameter and a large formation extent problem in this semi-analytical technique. We can design a heterogeneous model, and calculate a complete synthetic data set as the forward modeling. Then the synthetic data can be used to test inversion techniques, such as velocity tomography and attenuation tomography.

Chapter 4

Attenuation Estimation Using the Centroid Frequency Shift Method

In the previous two chapters, two forward modeling methods are developed to simulate elastic waves in complex boreholes. Because of their efficiency, stability, and accuracy, these new approaches have many applications to borehole seismic problems. In the following chapters, I apply these methods to investigate seismic attenuation estimation from borehole seismic data.

It has long been believed that attenuation is important for the characterization of rock and fluid properties, e.g., saturation, porosity, permeability and viscosity, because attenuation is more sensitive than velocity to some of these properties (e.g., Best et. al., 1994). Measurements of both velocity and attenuation provide complementary information about rock properties. Although attenuation is important, its reliable measurement is much more difficult than the velocity, since attenuation information in seismic data is easily contaminated by many factors. In this chapter I present a new method for estimating seismic attenuation based on frequency shift data. In comparison to some other methods of estimating attenuation, the frequency shift method is relatively insensitive to geometrical spreading, reflection and transmission effects, source and receiver coupling, radiation patterns, and instrument responses.

Seismic wave attenuation includes intrinsic attenuation and scattering attenuation. Both of them can cause wave dispersion. Scattering transfers wave energy to later arrivals or to other directions. Intrinsic attenuation transfers wave energy to heat. In the frequency shift method, wave dispersion is used as the observed signal for the attenuation estimation. In this study I concentrate to the intrinsic attenuation and try to reduce the influence of the scattering attenuation. In the situation when the scattering attenuation can not be ignored, the estimated attenuation is an combination of intrinsic and scattering effects.

In this chapter I first introduce the basic theory of the frequency shift method and then apply it to seismic attenuation tomography. Synthetic and real examples of 1-D and 2-D geological structures are presented to test this attenuation measurement technique. The wave modeling method introduced in Chapter 3 is used to calculate the synthetic seismograms for the 2-D attenuation tomography. In Chapter 5, I will use the basic theory of this method and the modeling tool given in Chapter 2 for numerical simulations on acoustic attenuation logging.

4.1 INTRODUCTION

In most natural materials, the high frequency components of the seismic signal are attenuated more rapidly than the low frequency components as waves propagate. As a result, the centroid of the signal's spectrum experiences a downshift during propagation. Under the assumption of a frequency-independent Q model, this downshift is proportional to a path integral through the attenuation distribution, and can be used as observed data to tomographically reconstruct the attenuation distribution. The frequency shift method is applicable to any seismic survey geometry where the signal bandwidth is broad enough and the attenuation is high enough to cause noticeable losses of high frequencies during propagation.

Recent improvements of seismic data quality, especially crosswell data, make it possible to estimate the heterogeneous distribution of seismic attenuation. For example, Brzostowski and McMechan (1992) used the change in seismic amplitude as observed data. However, amplitudes are easily contaminated by many factors such as scattering, geometrical spreading, source and receiver coupling, radiation patterns, and transmission/reflection effects. Therefore, it is often difficult to obtain reliable attenuation estimates from the amplitude decay method. In this chapter, I propose a method which is related to the pulse broadening phenomena. As a seismic pulse propagates in a medium, the shape of the pulse broadens because of dispersion due to intrinsic attenuation. The rise time associated with this broadening effect has been used to estimate attenuation (e.g., Kjartansson, 1979; Zucca, et al., 1994). However, a precise and robust measurement of the rise time is difficult for field data. Therefore, I use a related quantity, the estimated shift in the centroid of the pulse spectrum. The frequency shift or pulse broadening for wave packets is not affected by far-field geometrical spreading and transmission/reflection losses. Therefore, measurements based on the frequency shift appear to be more reliable than the amplitude decay method. It should be pointed out that the frequency shift method, measures the pulse broadening in frequency domain, while the rise time method measures a pulse broadening in time domain. The measurement in the frequency domain usually is more convenient and stable, but the spectral measurement is affected by the windowing.

Experiments indicate that the quality factor Q for many rocks is independent of frequency (e.g., Johnston, 1981). This is usually considered as the constant Q-model.

Under this model, the high frequency components of an incident wave are more attenuated during wave propagation than the low frequency components. If we examine the shape of the frequency spectrum, we find that its centroid experiences a downshift in frequency as the wave propagates, since the high frequency part of the spectrum decreases faster than the low frequency part. This phenomenon has been observed in VSP data, e.g. Hauge (1981). In this chapter, I propose an approach to estimate seismic attenuation based on this frequency shift. Since we want to quantitatively measure the attenuation from the centroid frequency shift, we need to derive a relationship which links the frequency shift to the attenuation parameters describing the medium. I use a method that is similar to the approach proposed by Dines and Kak (1979), and later used by Parker, et. al. (1988) for medical attenuation tomography. This method requires the data be broad band so that the frequency shift can be easily estimated. High frequency crosswell surveys provide good examples of such data.

In this chapter I first present the basic theory of the frequency shift method. Then I apply it to crosswell attenuation tomography for both synthetic and field data. I will give two field data examples: one is for 1-D geological structures and another is for 2-D geological structures.

In order to simulate 2-D attenuation tomography, we need to calculate viscoelastic waves in 2-D media. Purely numerical methods, e.g., finite difference and finite element methods, may not be used for this purpose. The frequency shift approach uses the dispersion information to measure the attenuation. The grid dispersion of these purely numerical methods could cause dispersion errors on the attenuation estimation. The wave modeling method introduced in Chapter 3 provides a very useful technique to simulate viscoelastic waves in complex media. This method is a semi-analytical approach. We do not need to discretize the model into grids. Therefore, there is not grid dispersion involved, and the calculation is faster and more accurate. I will give two synthetic data examples: one is for 1-D geological structures and another is for 2-D geological structures.

4.2 ATTENUATION COEFFICIENT AND CENTROID FREQUENCY SHIFT

Since we want a quantitative estimate of the attenuation from the centroid frequency shift phenomenon, we need an equation which links the frequency shift to the attenuation parameters describing the medium. To do this, we need a model that describes the attenuation feature of a materiel, and a parameter that defines the frequency shift of a signal.

4.2.1 Attenuation model

For the purpose of estimating attenuation, I assume that the process of wave propagation is described by the linear system theory. If the amplitude spectrum of an incident wave is $S(f)$ and the medium/instrument response is $G(f)H(f)$, then the received amplitude spectrum $R(f)$ may be, in general, expressed as (see Figure 4.1)

$$R(f) = G(f)H(f)S(f) \tag{4.1}$$

where the factor $G(f)$ includes geometrical spreading, instrument response, source/receiver coupling, radiation patterns, reflection and transmission coefficients, and the phase accumulation due to propagation; and $H(f)$ describes the attenuation effect on the amplitude. In this study, I concentrate on the absorption property of the medium, and call

Figure 4.1 Linear system model for attenuation.

H(f) the attenuation filter. Experiments indicate the attenuation is usually proportional to frequency, that is, we may write

$$H(f) = \exp\left(-f\int_{ray} \alpha_o dl\right), \tag{4.2}$$

where the integral is taken along the ray path, and α_o is attenuation coefficient defined by

$$\alpha_o = \frac{\pi}{Qv}, \tag{4.3}$$

i.e., attenuation is linearly proportional to frequency, where Q is medium's quality factor, and v is wave propagation velocity. Note that the attenuation factor α_o is different from the usually defined attenuation coefficient $\alpha = \alpha_o f$. This linear frequency model is useful in demonstrating the frequency shift method. More complex models, for example with higher power dependence on frequency, e.g.,

$$H(f) = \exp\left(-f^{p} \int_{ray} \alpha_{o}\, dl\right)$$

with $p \neq 1$ can be considered in a similar way (Narayana and Ophir, 1983).

Our goal is to estimate medium response *H(f)*, or more specifically, the attenuation coefficient α_o, from knowledge of the input spectrum *S(f)* and the output spectrum *R(f)*. A direct approach is to solve equation (4.1) by taking the logarithm and obtaining

$$\int_{ray} \alpha_{o}\, dl = \frac{1}{f} \ln\left[\frac{GS(f)}{R(f)}\right]. \tag{4.4}$$

Equation (4.4) may be used to estimate the integrated attenuation at each frequency and could be called an amplitude ratio method. However, as described above the factor *G* lumps together many complicated processes, and is very difficult to determine. Furthermore, the calculation of attenuation based on individual frequencies is not robust because of poor individual signal-to-noise. To overcome these difficulties, I propose a statistics-based method which estimates the attenuation coefficient α_o from the spectral centroid downshift over a range of frequencies.

4.2.2 Spectral centroid and variance

Let us define the centroid frequency of the amplitude spectrum of the input signal *S(f)* to be

$$f_S = \frac{\int_0^\infty f S(f)\, df}{\int_0^\infty S(f)\, df}, \tag{4.5}$$

and the variance to be

$$\sigma_S^2 = \frac{\int_0^\infty (f - f_S)^2 S(f) df}{\int_0^\infty S(f) df} . \tag{4.6}$$

Similarly, the centroid frequency of the received signal *R(f)* is

$$f_R = \frac{\int_0^\infty f R(f) df}{\int_0^\infty R(f) df} , \tag{4.7}$$

and its variance to be

$$\sigma_R^2 = \frac{\int_0^\infty (f - f_R)^2 R(f) df}{\int_0^\infty R(f) df} , \tag{4.8}$$

where *R(f)* is given by equation (4.1). If we take the factor *G* to be independent of frequency *f*, f_R and σ_R^2 will be independent of *G*. This is the major advantage of using the spectral centroid and variance rather than the actual amplitudes.

4.2.3 Relationships between Attenuation Coefficient and Spectral centroid

Consider the special case where the incident spectrum *S(f)* is Gaussian, i.e., given by the equation

$$S(f) = \exp\ [-\frac{(f - f_o)^2}{2\sigma_S^2}] . \tag{4.9}$$

From equations (4.5) and (4.7), we obtain (see Appendix C-1)

$$f_S = f_o , \tag{4.10a}$$

and

$$f_R = f_S - \sigma_S^2 \int_{ray} \alpha_o dl . \tag{4.10b}$$

By substituting equation (4.10a) into (4.10b) we may rewrite equation (4.10b) as a line integral suitable for tomographical inversion:

$$\int_{ray} \alpha_o dl = (f_o - f_R) / \sigma_S^2 . \tag{4.11}$$

Figure 2 gives a pictorial description of Gaussian spectra. Using the values of f_S, f_R and σ_S^2 given with Figure 4.2, we get the inversion result exactly matching the value ($\int \alpha_o dl = 0.0008$) used in computing the filter *H(f)* for the example of Figure 4.2.

A similar derivation (see Appendix C-2) for non-Gaussian spectra (boxcar and triangular) leads to the following results. Numerical results for these special case spectra are summarized in Table 4.1. For the boxcar spectrum with bandwidth *B*, we obtain an approximate formula

$$\int \alpha_o dl \approx 12 (f_S - f_R) / B^2 . \qquad \text{for } B \int \alpha_o dl << 1 . \tag{4.12}$$

Figure 4.3 gives a pictorial description of frequency shift for the boxcar spectrum. Plugging the values of f_o, f_R and *B* shown in Figure 4.3 into equation (4.12), we obtain the inversion result $\int \alpha_o dl = 0.000797$ which is very close to the given value of 0.0008. For a triangular spectrum with bandwidth *B*, we obtain another approximate formula (see Appendix C-3)

$$\int \alpha_o dl \approx 18 (f_S - f_R) / B^2 , \qquad \text{for } B \int \alpha_o dl << 1 . \qquad (4.13)$$

Under the assumption of a constant *Q*-model I have derived tomographic equations (4.11), (4.12), and (4.13) for Gaussian, rectangular and triangular spectra, respectively. These equations show that the attenuation coefficient for an inhomogeneous medium $\alpha_o(x,z)$ can be obtained by measuring the centroid frequency downshift $(f_S - f_R)$ between the incident and transmitted signals. The integrated attenuation equals this frequency downshift multiplied by a scaling factor. From equations (4.11) – (4.13) we find that a broader input bandwidth (larger σ_S or *B*) leads to a larger frequency change. Therefore, a broad input frequency band is important for a robust estimation of $\alpha_o(x,z)$. Crosswell seismic profiling with a high frequency downhole source provides a good opportunity to test attenuation tomography using this frequency shift method.

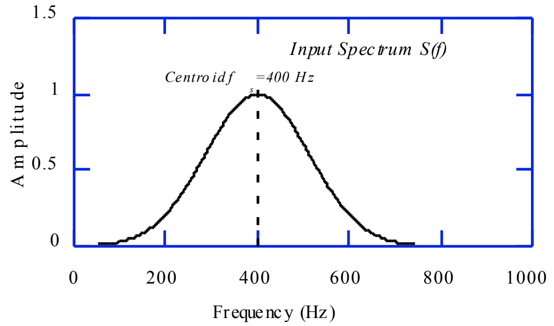

Figure 4.2a An input spectrum of Gaussian shape with center frequency (spectral centroid) of 400 Hz and variance of 12730 Hz^2.

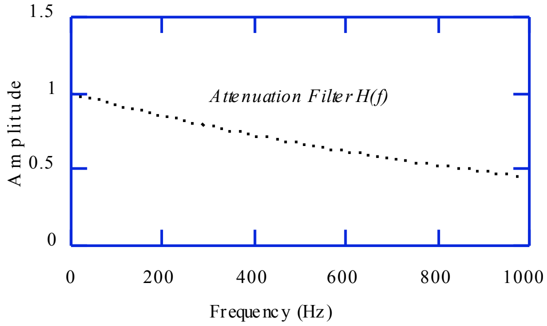

Figure 4.2b Medium response for $\int \alpha_o dl = 0.0008$.

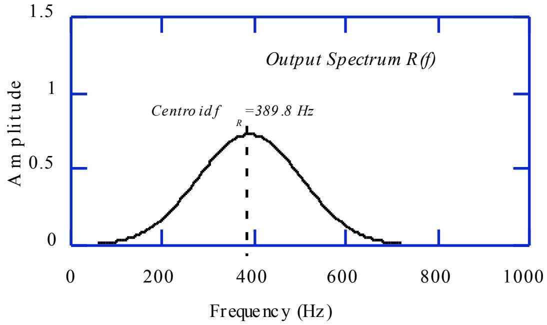

Figure 4.2c The output spectrum remains Gaussian shape with a variance of 12730 Hz^2, but the spectral centroid is shifted to 389.8 Hz.

The tomographic formula relating frequency shift with the attenuation projection is exact only for Gaussian spectra, i.e., equation (4.11). Nevertheless, the approximate formulae, equations (4.12) and (4.13), are useful in practical situations where Gaussian spectra can not be assumed. Although equations (4.11), (4.12), and (4.13) are derived from spectra of different shapes, they are somewhat similar. This similarity implies the robustness of this method, that is, the estimate of relative attenuation is not sensitive to a small change in spectrum shapes.

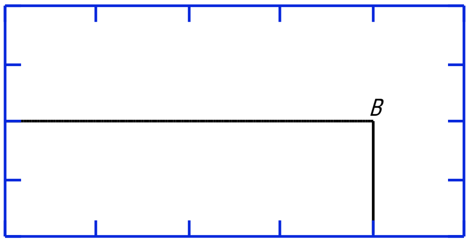

Figure 4.3a A boxcar input spectrum with spectral centroid of 400 Hz and band width is 800 Hz.

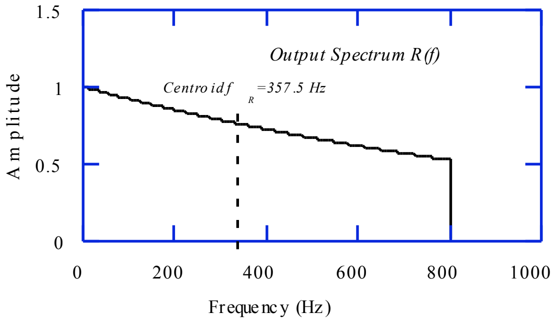

Figure 4.3b The spectral centroid of the output spectrum shifts to 357.5 Hz. The medium response is the same as Figure 2b.

Table 4.1 Numerical results for three special spectra

Spectrum Shape	Model $\int \alpha_o dl$	Estimated $\int \alpha_o dl$	f_S (Hz)	σ_S^2 or B^2 (Hz^2)	f_R (Hz)	σ_R^2 or B^2 (Hz^2)
Gaussian	0.0008	0.0008	400	12730	389.8	12730
Boxcar	0.0008	0.000797	400	800^2	357.5	800^2

Triangular	0.0008	0.000765	266.3	800^2	239.1	800^2

4.3 VALIDATION TEST

Before using equation (4.11), let us first examine its validity by considering an ideal synthetic example in the zero offset VSP geometry. For this geometry both input and output centroid frequencies f_S and f_R are measurable since signals in two successive receivers can be viewed as the incident and transmitted spectra. In this case, we write equation (4.11) as

$$\alpha_{oi} = \frac{1}{\sigma_i^2} \frac{\Delta f_i}{\Delta z_i}, \tag{4.14}$$

where $\Delta f_i = f_i - f_{i+1}$ is the centroid frequency difference between two successive depth levels, Δz_i is the distance between these two receivers, α_{oi} is the average attenuation coefficient between the two levels, and σ_i^2 the variance at ith receiver.

The generalized R/T coefficients method for vertically layered media (Apsel, 1979) is used to model the seismic response. Attenuation in this synthetic model is introduced through the complex velocity [see equation (2.26)]. The full wavefield is calculated at 220 receivers. Figure 4.4a shows the model. The frequency band of the source is 10 Hz – 2010 Hz. This frequency band is much broader than the real VSP, but it is used here to illustrate the range of typical crosswell data for which this algorithm was initially developed. I select a time window that isolates the first arrival. Figure 4.4d is a plot of the centroid frequency picked from the data. The centroid frequency decreases from 370 Hz to 280 Hz over a range of nearly 1000 feet. After smoothing the data and computing equation (4.14), I obtain an estimate of the attenuation coefficient α_o. Then using the definition $Q = \pi / (\alpha_o v)$, we get the estimated Q-values shown in Figure 4.4c. The reconstructed Q-value (dotted line) fits the original synthetic model (solid line) very well. The deviations of the inversion result near interfaces are caused by the interference of reflections in the estimation of the frequency shift near interfaces. Therefore, the thicker the layer, the better the inversion result. However, even for a relatively thin layer, the layer around the depth of 1770 feet, I obtain a satisfactory result.

4.4 SEISMIC ATTENUATION TOMOGRAPHY

The ideal VSP test done in previous section shows the frequency shift can be used for seismic attenuation estimation. In this section I apply this method to attenuation tomography. I first solve some practical problems related to attenuation tomography. Then, I present four examples for synthetic data and field data.

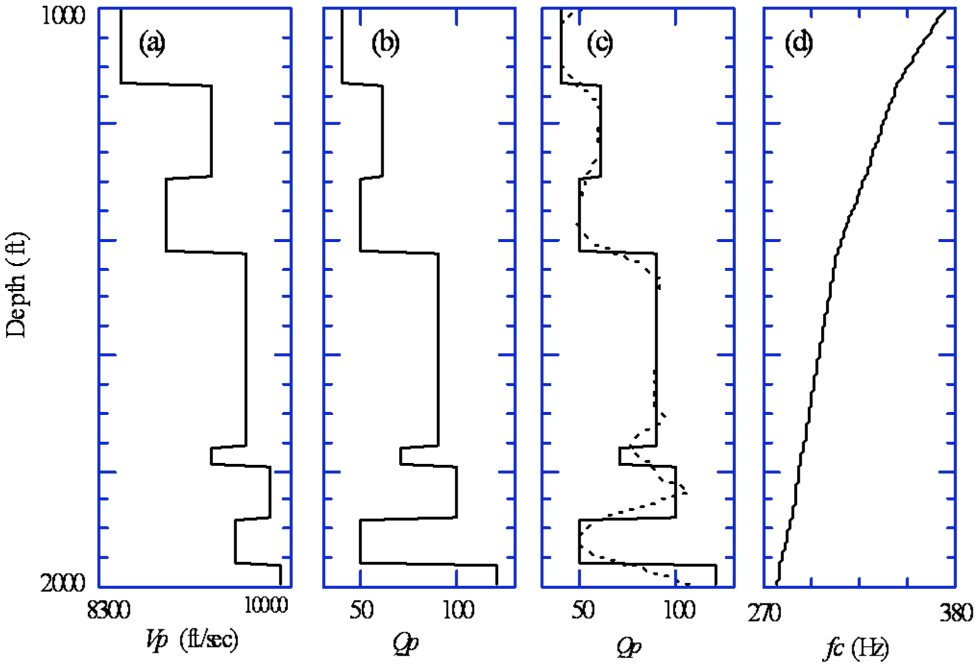

(a) Given velocity.

(b) Given Q-value.

(c) Reconstructed Q-value (dashed line) and the given Q-value (solid line).

(d) Centroid frequency picks from the synthetic VSP data.

Figure 4.4 A synthetic test of the frequency shift method using the zero offset VSP geometry. The model shown in (a) and (b) are used to calculate the VSP. Curve (d) is a plot of the centroid frequencies, which are used to obtain the reconstructed Q-values shown in (c).

4.4.1 PRACTICAL CONSIDERATIONS

Equation (4.11) is the basic formula for attenuation tomography. It can be written in a discrete form:

$$\sum_j \alpha_{oj}^i l_j^i = \frac{f_S - f_R^i}{\sigma_s^2} . \tag{4.15}$$

Here, the index i represents the i^{th} ray and j the j^{th} pixel of the medium; l_j^i is the ray length within the jth pixel. In practice we can measure f_R from recorded seismograms, but may not directly measure the source centroid frequency f_S and the variance σ_s^2. For the constant Q-model described by equation (4.2) and Gaussian spectrum given by equation (4.9) the source spectrum $S(f)$ and receiver spectrum $R(f)$ exhibit the same variance σ_s^2. Therefore, we may choose the average of variances σ_R^2 at the receivers as the estimate of the source variance σ_s^2. While the source spectral frequency f_S is also unknown, I include it along with the matrix of unknown attenuation values. Then, I simultaneously invert for both the attenuation coefficients α_j^i and the source frequency f_S as follows. Let

$$f_S = \bar{f}_S + \Delta f\,, \tag{4.16}$$

where $\bar{f}_S = \max\{f_R^i\}$ is an initial estimation of f_S, and Δf is a static correction. Then

$$\frac{f_S - f_R^i}{\sigma_s^2} = \frac{\bar{f}_S + \Delta f - f_R^i}{\sigma_s^2} = \frac{\bar{f}_S - f_R^i}{\sigma_s^2} + \frac{\Delta f}{\sigma_s^2}\,. \tag{4.17}$$

Equation (4.15) can now be written as

$$\sum_j \alpha_j^i l_j^i - \frac{\Delta f}{\sigma_s^2} = \frac{\bar{f}_S - f_R^i}{\sigma_s^2}\,, \tag{4.18}$$

where α_j^i and Δf are the unknowns to be determined.

In order to obtain more stable and precise measurement of the centroid frequency, we need do some data processing. The main purpose of data processing is to extract the direct wave and reduce the interference due to scattering. To do this I first pick and align the direct wave. Next, I mix traces to reduce interference due to scattering, and perform FFT on the direct arrival isolated by a short time window. The central frequency f_R and variance σ_s^2 are then calculated by equations (4.7) and (4.8). If we treat $(\bar{f}_S - f_R^i)/\sigma_s^2$ as "data", α_j^i as "unknown", and add one more term $-\Delta f / \sigma_s^2$ to the system, then we only need to slightly modify the algorithms and programs for travel time tomography to do the attenuation tomography.

In most situations, the medium is heterogeneous in both velocity and attenuation. I first use the travel time to estimate the velocity distribution and the ray paths, then use the frequency shift data and these ray paths to estimate attenuation. Finally, because the *Q* model underlies the development of the theory, I estimate the *Q* distribution by combining the velocity and attenuation tomograms. However, the image of the attenuation factor can be used as the final result.

4.4.2 NUMERICAL TESTS

I here give two synthetic crosswell attenuation tomography examples. The first one is 1-D layered geological structures. The original model is shown in Figure 5a. The generalized R/T coefficients method for vertically layered media (Apsel, 1979) is used for the seismic modeling. The attenuation in this model is introduced by using a complex velocity [see equation (2.26)]. I placed 51 sources in one well and 51 receivers in another well with a well offset of 400 feet, and calculate a complete synthetic crosswell survey. Figures 4.5b and 4.5c give a common source gather in time domain and frequency domain, respectively. Figure 4.5c clearly shows that the spectral shifts downwards as the source-receiver offset increases. Figure 4.6 is the reconstruction of *Q*-values. I plot the original profile and reconstructed profile together to make a closer comparison. We can see that the tomography, based on the line integral given by equation (4.11), is capable of imaging the Q distribution.

The second synthetic example has two abnormal structures. Figure 4.7a gives the original model. I also place 51 sources in a open borehole and 51 receivers in the formation. Both source interval and receiver interval are 2 feet. Ricker wavelet [equation (2.27)] with peak frequency of 1000 Hz is used as source function. Figure 4.7b shows the inversion result. The reconstructed Q-values is quite close to the given ones.

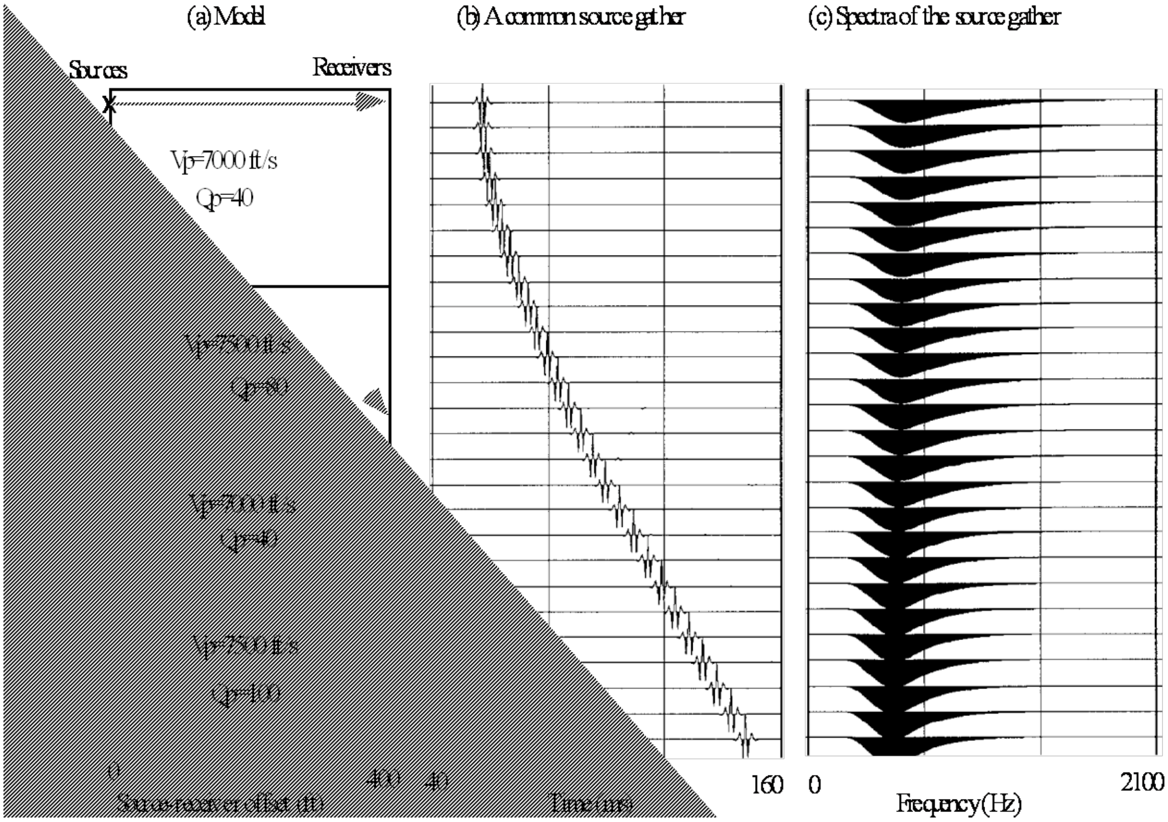

Figure 4.5 The synthetic forward modeling for crosswell attenuation tomography. A layered model (a) of crosswell profiling is calculated. A point source with Ricker wavelet is used. We show a common source

gather in time and frequency domains in (b) and (c), respectively. The spectral downshift can be seen in (c).

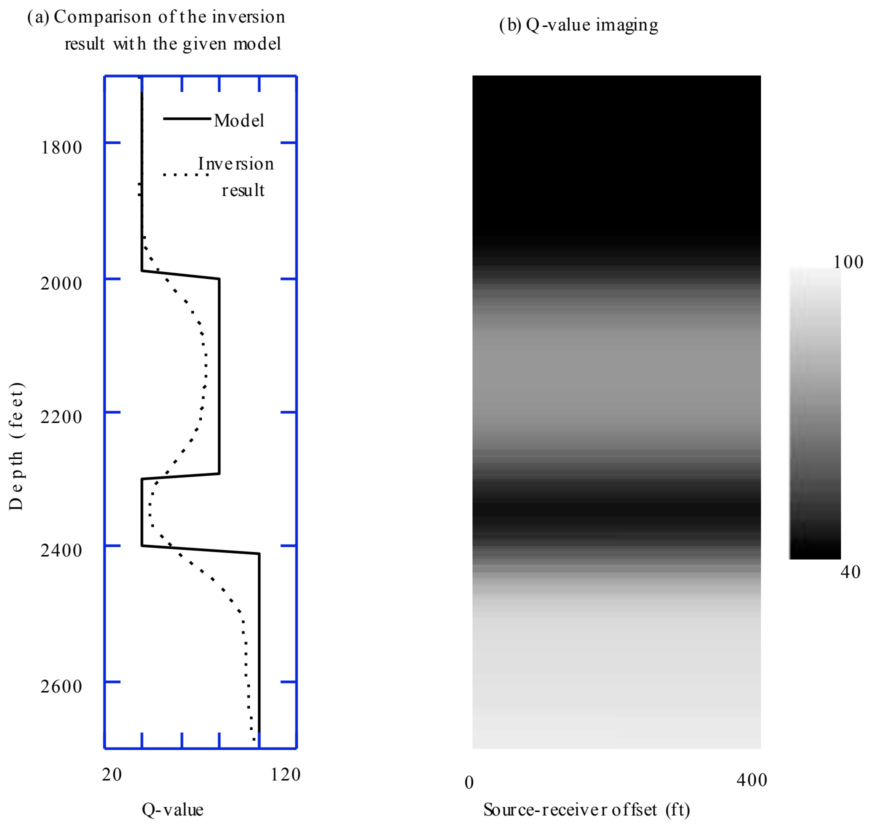

Figure 4.6 The tomographic inversion result of the 1-D synthetic test. The dotted line in (a) is the profile of the 1-D imaging (b). The comparison in (a) shows the inversion is pretty close to the given model.

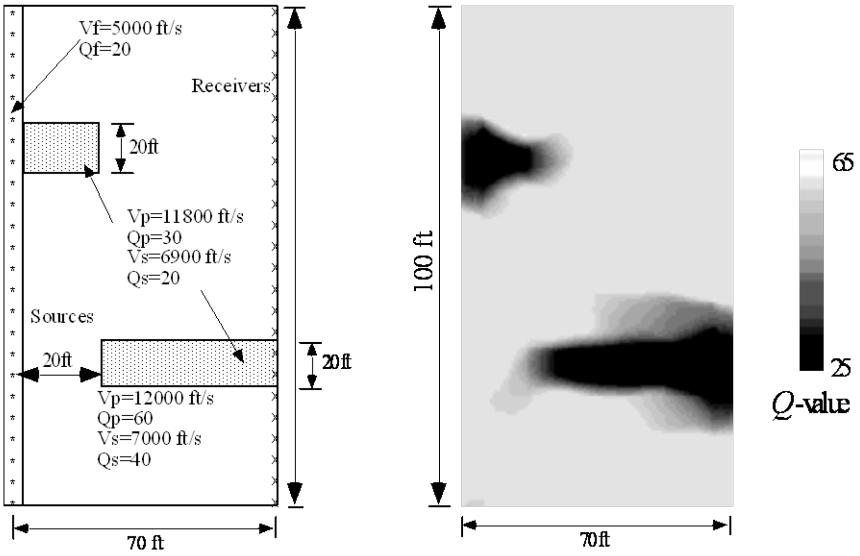

(a) (b)

Figure 4.7 Synthetic test on 2-D attenuation tomography. (a) is the original model. There are two low *Q*-value areas in this model. (b) is the reconstructed *Q*-value distribution.

It seems that the finite difference or finite element method could be a good choice for this 2-D forward modeling. In fact, the grid dispersion in these numerical methods would be a problem with this attenuation simulation. In the frequency shift method, the wave dispersion information is used to estimate attenuation. Therefore, the grid dispersion in the numerical methods would introduce numerical error in the simulation.

For this test, I use the forward modeling method described in Chapter 3. Since this method is a semi-analytical approach, there is no grid dispersion in the computing.

4.4.3 Field data: one dimensional geological structure

For field data, I first choose a data set collected at BP's Devine test site where the lithology is layer cake, and the geological structure is approximately one dimensional. A linear sweep from 200Hz to 2000Hz was used as the source spectrum. Figure 4.8 shows the travel time and centroid frequency picks from this field data set. It can be seen from these picks that the high centroid frequency correlates to the fast travel time. This correlation indicates that the high velocity formation in this area has low attenuation. I first use travel time tomography to reconstruct the velocity structure and obtain ray paths. Then, I use the ray paths and centroid frequencies to inverse the attenuation structure. A 1-D layered model is assumed for this inversion problem. Figure 4.9 shows the velocity and attenuation reconstructions. For the attenuation tomography, the starting model is a homogeneous model which is calculated using the average of centroid frequency shift data. The initial source frequency $\bar{f}_s$ is 1750 Hz. After inversion the final source frequency f_S is 1520 Hz. The attenuation coefficient α_o and velocity v are converted to Q-values using equation (4.3). The lithology and the sonic log are also shown in Figure 4.9 for comparison. They exhibit an excellent geometric agreement with the inversion results. As what we expect, Figure 4.9 shows that shale and sand have lower Q-value and slower velocity, and limestone has higher Q-value and faster velocity.

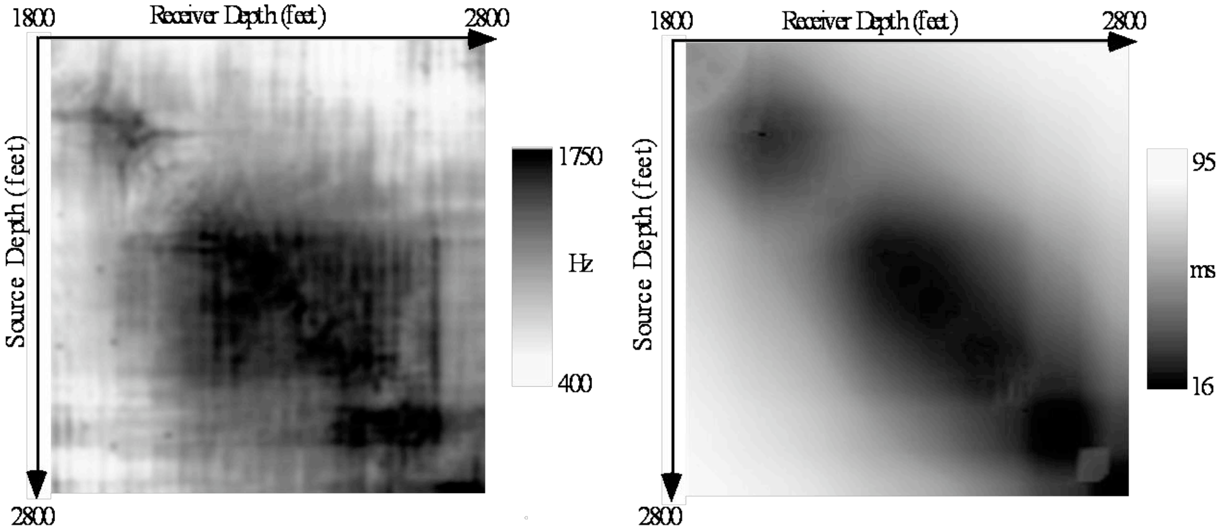

(a) A chart of centroid frequency picks

(b) A chart of travel time picks

Figure 4.8 The data picked from the Devine survey for the attenuation tomography. The travel time of the direct *P*-wave is shown in (b), which is used to obtain a velocity model and ray paths. With these ray paths and the centroid frequency shown in (a) of the *P*-wave, we can perform the attenuation tomography. A horizontal line in (a) or (b) represents a common source gather, and a vertical line represents a common receiver gather. From these picks we can see a good correlation between travel time and centroid frequency. The high frequency (dark color), corresponds to the high *Q*-value formation and correlates to the fast travel time (dark color), which corresponds to the high velocity formation.

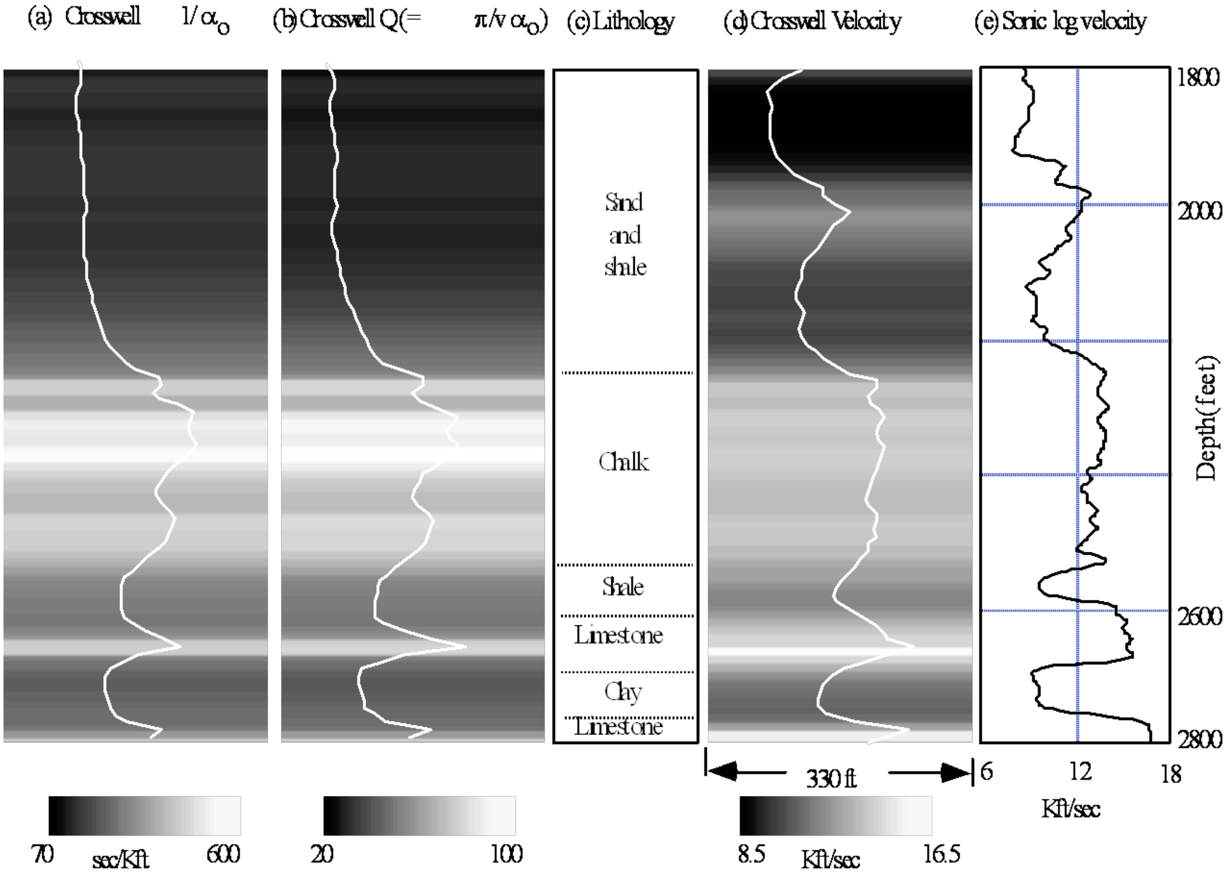

Figure 4.9 Attenuation and velocity tomography for the Devine survey. We first calculate the velocity (v) and attenuation coefficient (α_o), then convert them to Q-value. In order to make a closer comparison we plot the

profile curves within the tomograms. It can be seen that Q-value, velocities and lithology exhibit a good correlation.

4.4.4 Field data: two dimensional geological structure

The second field data example is more complex one (see Figure 4.10). It is also a crosswell seismic survey. The data was collected from an oil field in West Texas. The geological structures between two wells are complicated. A reef structure (indicated by letter B in Figure 4.10) is a reservoir. The source-receiver offset at the surface is 620 feet (note that both source and receiver wells are deviated). There are 203 sources and 203 receivers with interval of 5 feet. The source well penetrated the carbonate reef target, but the receiver well missed this target. One purpose of this crosswell survey is to image the reef structure, and to see where the reef ends.

Synthetic test (see Figure 4.7) shows that the attenuation tomography based on the frequency shift is capable to image a complex structure. I here try to use both velocity tomography and attenuation tomography to image the reef structure, and hope they provide complementary information about the structure.

I use a 2-D model for the tomographic inversion. The starting model for the inversion is homogeneous. I first perform travel time tomography to obtain the velocity structure and ray paths. Then, I use the ray paths and the centroid frequency picks for the attenuation tomography. The centroid frequency picks of this data range from 600 Hz to

1000 Hz. The maximum frequency 1000 Hz is chosen as the initial source frequency $\bar{f}_s$. The final source frequency f_S is 850 Hz. Figure 4.10 shows the 2-D *P*-wave velocity and attenuation tomograms which reveal a consistent image of the lateral variations of the carbonate reef buildup. If we look the tomograms more carefully, however, we may find that the reef exhibits a larger extension toward the receiver well in the attenuation tomogram.

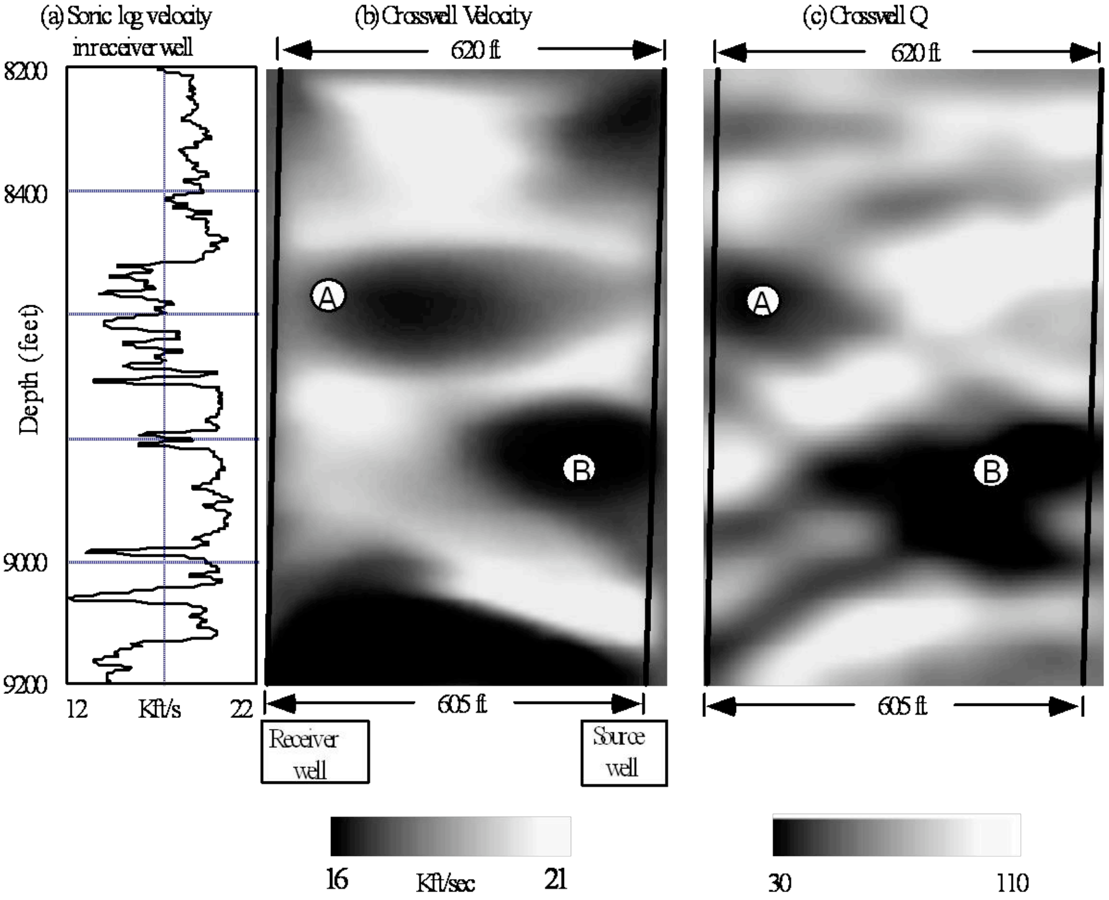

Figure 4.10 The attenuation and velocity tomography for the west Texas survey. The geological structure in this area is complex. The main features are two low-velocity/low-Q zones indicated by "A" and "B", respectively. Area B is interpreted as a carbonate mound or reef.

4.5 CONCLUSIONS

Frequency-dependent attenuation causes a change in the amplitude distribution of a wave's frequency spectrum. For a constant Q-model and a Gaussian spectrum this change is simple: the difference in centroid frequency between the incident (input) and transmitted (output) waves is proportional to the integrated attenuation multiplied by a scaling factor. Spectra other than Gaussian can be handled by changing the scale factor. This fact results in a simple formula that can be used for attenuation tomography. Although the method is sensitive to small frequency changes, it is best on data with a broad frequency band. The crosswell geometry with a high frequency downhole source provides a good opportunity to use this method. Field data tests in 1-D and 2-D cases show that the attenuation tomograms have a good correlation with lithology and the velocity tomogram. The source frequency static correction introduced in this method makes the attenuation estimation more robust and stable. In Chapter 5, the frequency shift method will be used for sonic log analysis.

Chapter 5

Acoustic Attenuation Logging in Complicated Boreholes

Many efforts have been made to estimate the seismic attenuation from sonic logs. Existing methods include amplitude ratio, spectral ratio, partition coefficients, and full waveform inversion (Paillet and Cheng, 1991, Page 138). In this chapter I propose another acoustic attenuation logging method, which is based on the centroid frequency shift introduced in Chapter 4. The centroid frequency shift method was applied to crosswell seismic attenuation (Section 4.4; Quan & Harris, 1993). In crosswell profiling, this method measures the spectral centroid difference between incident and transmitted waves, and uses this difference to estimate the attenuation. For full waveform logging, I take the advantage of multiple receivers and measure the spectral centroid difference between two or more receivers for attenuation estimation.

The geometrical spreading is a fundamental property of waves. It is also very important for the attenuation estimation. When estimating intrinsic attenuation of the formation from waveform sonic logs, we must correct for the geometrical spreading. The geometrical spreading factor, in general, is frequency-dependent (Paillet and Cheng, 1991, Page 144; Quan, et al., 1994). In this chapter, I propose an empirical formula to describe the frequency-dependent geometrical spreading of the *P* wave in a borehole.

In order to understand the attenuation properties of the P wave in complex boreholes and provide a guide to in situ measurement, I used the generalized reflection and transmission coefficients method (Chapters 2 and 3; Chen, et al., 1996) to simulate waves in boreholes. Then, I applied the centroid frequency shift method to synthetic data for attenuation estimation. After the synthetic test, I also applied the frequency shift method to field data for acoustic attenuation logging.

The same synthetic log data are also used to study the P wave geometrical spreading in complex boreholes. For a monopole source in a simple open borehole, the geometrical spreading factor is $1/z$, which is the same as previous work (Roever et al., 1974; Winbow, 1980). For a borehole with an invaded zone, this study reveals that the geometrical spreading factor is more complicated than the simple $1/z$ factor.

5.1 FREQUENCY SHIFT PHENOMENON IN REAL SONIC LOGS

The frequency shift is not only observed in crosswell seismic data (Chapter 4), but also in full waveform acoustic logs. Figure 5.1 demonstrates the configuration of a fluid-filled borehole with a mud cake and an invaded zone (see Section 5.3 for more explanation). There is a sonic tool in the center of the borehole, which consists of a source and a receiver array. Acoustic waves recorded at the receivers are micro-seismograms or full waveform acoustic logs. A waveform log data set collected from Well 1202 in the McElroy field is used to test the frequency shift. Figure 5.2 shows a record at depth of 3009 feet. Travel times in Figure 5.2a increases with increasing source-receiver offset (indicated by Line A). The spectra in Figure 5.2b, however, decreases with the increasing offset (indicated by Line B). Line B clearly shows the central frequency shift.

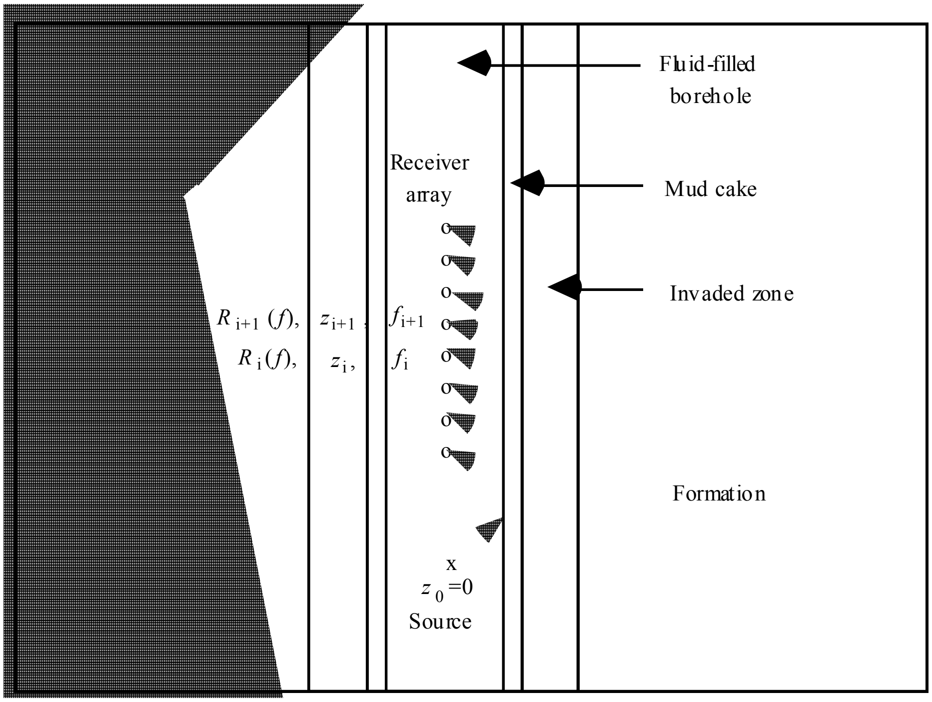

Figure 5.1 Acoustic logging configuration. $R_{i+1}(f)$ is the signal spectrum at the i^{th} receiver, z_i is receiver depth and f_i is the centroid frequency of $R_{i+1}(f)$ defined in equation (5.5). $|z_i - z_o|$ is source-receiver offset.

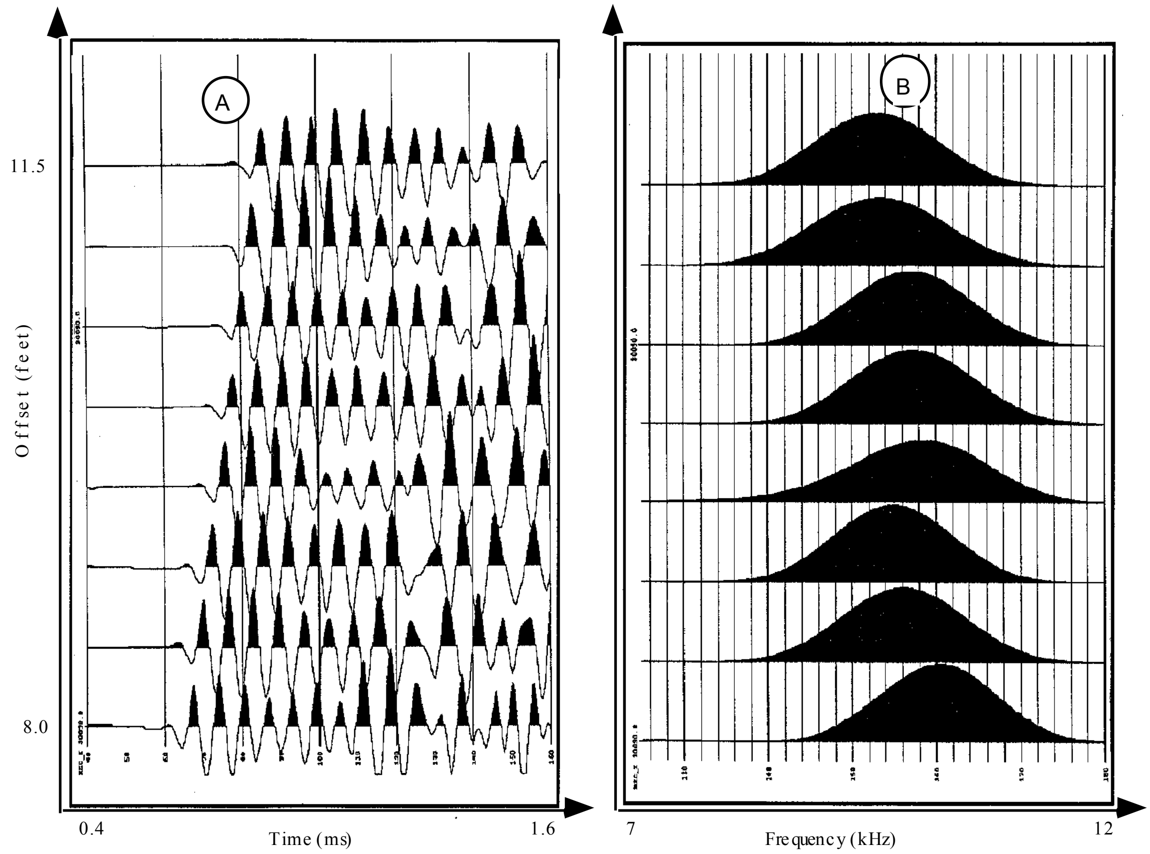

(a) Microseismograms

(b) Spectrum of the first arrival

Figure 5.2 An example of frequency shift from a real waveform acoustic log. Line A in (a) indicates the travel time of the *P* wave. The travel time *increases* with the increasing source-receiver offset. Line B in (b) shows the spectral peak. The spectral peak *decreases* with the increasing offset, i.e., the spectrum experiences a downshift as the wave propagates.

Assume that the intrinsic attenuation is proportional to frequency (see Chapter 4). As a body wave propagates, the high frequency component is more attenuated than the low frequency. As a result, the spectral centroid of the wave moves to low frequency direction. I derived a formula that relates the amount of the frequency shift and the attenuation coefficient for body waves [see equation (4.14)]. We can not directly apply that formula for borehole waves before we understand the borehole effects on the frequency shift. In the following sections, I use numerical simulation to study this problem. The forward modeling is done using the generalized reflection and transmission coefficients method introduced in Chapter 2.

5.2 ATTENUATION LOGGING USING THE CENTROID FREQUENCY SHIFT METHOD

The first arrival in full waveform sonic logs is *P* wave refracted from borehole wall. We can separate it from later arrivals using a Hanning window. This first arrival is used to estimate *P* wave attenuation coefficient. The magnitude of recorded wave spectrum $R_{i+1}(f)$ at $r = 0$ and $z = z_{i+1}$ is written as (see Figure 5.1)

$$R_{i+1}(f) = \frac{R_i(f)}{G_i} G_{i+1} \exp\,[-\alpha_{oi} f (z_{i+1} - z_i)]\,, \tag{5.1}$$

where *G* represents geometrical spreading, and

$$\alpha_{oi} = \pi / (v_i Q_i) \tag{5.2}$$

is the intrinsic attenuation coefficient. In general, the velocity v_i and attenuation coefficient α_{oi} vary with depth z_i. Here, I only consider models with radial variation and no vertical variation involved. The subscript "i" indicates the i^{th} receiver in a receiver array. As noted by some authors (e.g., Paillet and Cheng, 1991, Page 144), the geometrical spreading of this refracted wave is highly frequency dependent. But how the geometrical spreading depends on frequency is not clear. In this study, I propose an empirical formula,

$$G_{i+1} = G(f, z_{i+1}) \approx \frac{\exp(-\alpha_g f z_{i+1})}{z_{i+1}^{p}}, \tag{5.3}$$

to describe the frequency dependent geometrical spreading, where α_g is an attenuation coefficient related to frequency-dependent geometrical spreading, and p is the power of "true" geometric spreading factor. Combining Equations (5.1) and (5.3) we have

$$R_{i+1}(f) = \left(\frac{z_i}{z_{i+1}}\right)^p R_i(f) \exp\left[-f(\alpha_g + \alpha_{oi})(z_{i+1} - z_i)\right]. \tag{5.4}$$

I will empirically determine α_g and p from numerical simulation for a given borehole structure. The frequency shift method (Chapter 4; Quan and Harris, 1993) is used to estimate the intrinsic attenuation coefficient α_o. In this method I define the spectral centroid of $R_i(f)$ to be

$$f_i = \frac{\int_0^\infty f R_i(f)\,df}{\int_0^\infty R_i(f)\,df}, \tag{5.5}$$

and its variance to be

$$\sigma_i^2 = \frac{\int_0^\infty (f - f_i)^2 R_i(f)\,df}{\int_0^\infty R_i(f)\,df}. \tag{5.6}$$

Then, the intrinsic attenuation coefficient α_{oi} at depth z_i can be obtained from following equation:

$$\alpha_{oi} = \frac{1}{\sigma_i^2}\frac{\Delta f_i}{\Delta z_i} - \alpha_g, \tag{5.7}$$

where $\Delta f_i = f_i - f_{i+1}$ is the frequency down-shift between two successive receivers, and $\Delta z_i = z_{i+1} - z_i$ is the distance between two receivers. If the geometrical spreading attenuation α_g is known, equation (5.7) can be used to estimate the intrinsic attenuation α_{oi}. In numerical simulation, Intrinsic attenuation α_{oi} is known. Then, if equation (5.3) correctly describes the geometrical spreading, for a given model we can estimate α_g from

$$\alpha_g = \frac{1}{\sigma_i^2}\frac{\Delta f_i}{\Delta z_i} - \alpha_{oi}. \tag{5.8}$$

I here investigate three typical boreholes by numerical simulation.

Let us first consider a simple open borehole whose model parameters are shown in Figure 5.3a in which Q_p=40. The synthetic micro-seismograms in a common source gather for this model are shown in Figure 5.3b. The source function used in this and later examples is given by equation (2.25),

$$F(\omega) = \frac{1}{\omega^2} \frac{8\alpha\omega_o(\alpha - i\omega)}{[(\alpha - i\omega)^2 + \omega_o^2]^2},$$

with $\omega_o = 2\pi \times 14$ KHz and $\alpha = 0.5\omega_o/\pi$. I use a short time window to extract the *P* wave (first arrival) and use equation (5.5) to calculate the spectral centroid (the curve for Qp=40 in Figure 5.4). For the purpose of reducing the effect of the window length and the contamination of later wave trains, we only use the seismograms with source to receiver separation greater than 3.5m for this and the later examples. Changing the Qp value in Figure 5.3a to Qp = 80 and Qp =120, I obtain two other curves in Figure 5.4. Figure 5.4 shows that different slopes of the centroid frequency curves correspond to different Qp values. Using equation (5.8) and the data shown in Figure 5.4, I obtain the estimated α_g=1.3x10^{-6} sec/m (or $\alpha_g = \pi/(vQ_g)$ with Q_g = 450) for this given borehole model.

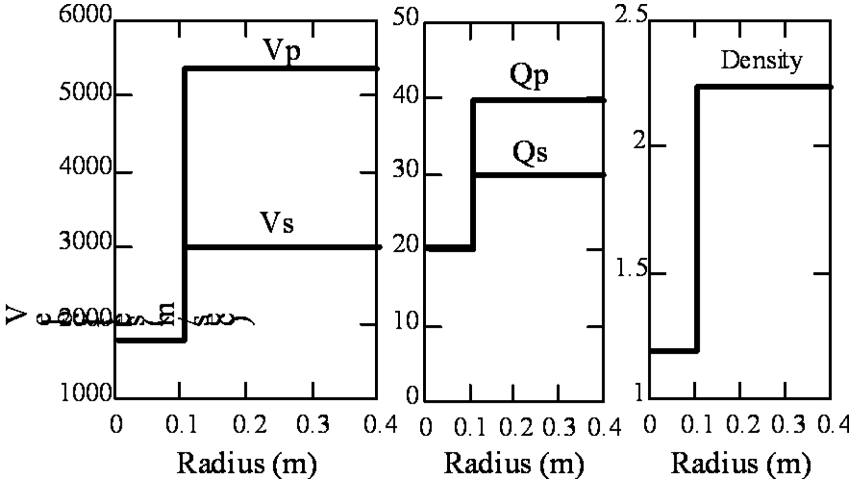

Figure 5.3a A simple borehole model.

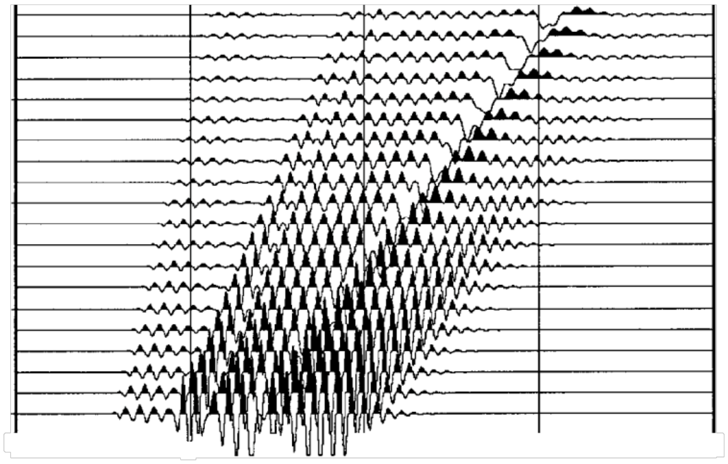

Figure 5.3b Micro-seismograms calculated for the simple borehole.

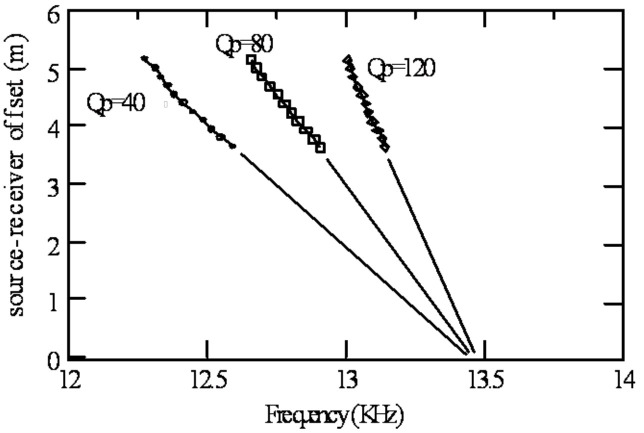

Figure 5.4. Centroid frequency picks corresponding to Q_p=40, Q_p=80 and Q_p=120 for simple open borehole.

If the geometrical spreading attenuation α_g is known, equation (5.7) can be used to estimate intrinsic attenuation α_o. Table 5.1 gives test results on the estimation for $Q_p = \pi / (v_p \alpha_o)$ with and without correction α_g. It can be seen that the estimated $\hat{Q}_p$'s are systematically smaller than the given Q_p's, if we ignore the effect of frequency-dependent spreading (i.e., set $\alpha_g = 0$). Since it is possible to find a common correction value of α_g=1.3x10^{-6} sec/m for all cases of Q_p=40, 80 and 120, I may conclude that equation 5.3 is an adequate description of the frequency-dependent geometrical spreading for this simple open borehole model. The frequency shift method does not depend on the "true" geometrical spreading $1/z^p$ (this is one of the advantages of this method, see Chapter 4). I will use another method to determine the power p in $1/z^p$ in next section.

Table 5.1 Estimation of Q_p for a simple open borehole

Given Q_p	40	80	120
Estimated $\hat{Q}_p$ (α_g=0)	37	69	95
Estimated $\hat{Q}_p$ (α_g=1.3x10^{-6} s/m)	40	82	120

This simulation shows the central frequency shift method can be used to calculate acoustic attenuation logs for a simple open borehole. Even we ignore the frequency-dependent geometrical spreading (i.e., set α_g=0), the estimated $\hat{Q}_p$ is still satisfactory. The value of α_g depends on the structure of a borehole. For a real borehole, it is difficult to know its exact value. Since α_g is very small, we may simply choose α_g=0 for a simple open borehole, and estimate attenuation using equation (5.7).

Next, let us investigate two types of complicated boreholes: the borehole with a damaged zone and the borehole with a flushed zone, respectively. During drilling of a well the hydrostatic pressure of the mud column is usually greater than the pore pressure of the formations. This prevents the well from blowing out. The pressure differential, however, forces the mud filtrate into the permeable formation, forming a mud cake on the borehole wall and an invaded zone near the borehole wall. The extent or depth of the invaded zone depends on many parameters, such as the type of the drilling mud, the formation porosity, the formation permeability, the pressure differential, and the time since the formation was first drilled. The invasion depth is usually 15 to 30 inches, but can be as shallow as a couple of inches or as deep as 10 feet. If the velocity of an invaded zone is greater than the uncontaminated formation, it is referred to as the flushed zone; if the velocity of an invaded zone is slower the uncontaminated formation, it is referred as damaged zone (Baker, 1984).

Figure 5.5a shows a model which consists of a fluid-filled borehole, a mud cake, a damaged zone, and an unperturbed formation. Since the modeling algorithm can efficiently handle an arbitrary number of radial layers, I use ten thin layers to describe the damaged zone. In this model the *P* wave quality factor Q_p is linearly changed from 35 to

40. Figure 5.5b is the micro-seismograms in a common source gather calculated for this model. I also keep the velocity and density fixed and only change the Q_p of the damaged zone in Figure 5.5a to be 75-80 and 115-120, respectively, to calculate two other synthetic data sets. Figure 5.6 gives the centroid frequency picks for this damaged zone model corresponding to different Q_p values.

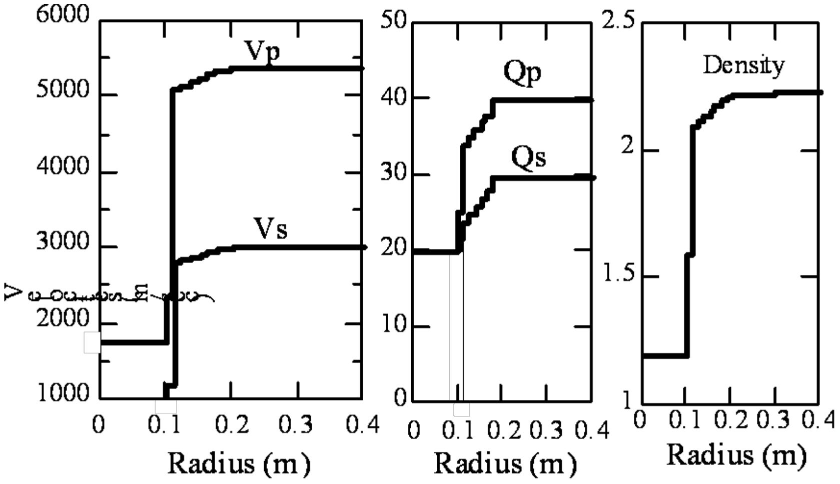

Figure 5.5a. A damaged zone model. The borehole is filled with fluid. On the borehole wall (radius *r*=.1 m), there is a thin mud cake. The velocity of the damaged zone gradually increases until reach the formation velocity. The damaged zone is described by thin layers.

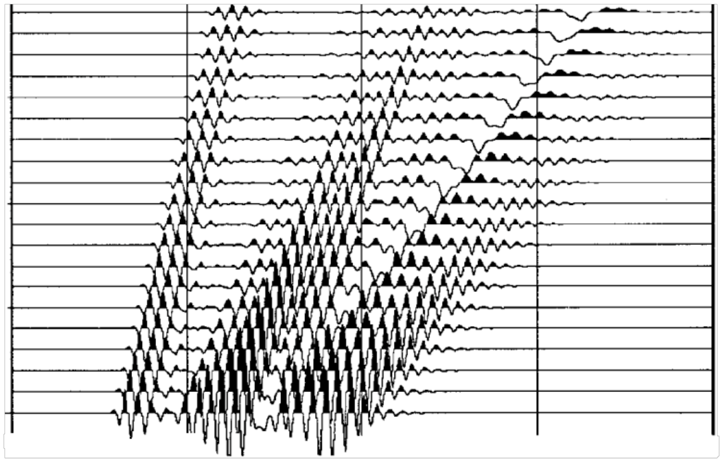

Figure 5.5b Micro-seismograms recorded in a borehole with a damaged zone. The amplitude of the *P* wave decays significantly slower than that for the simple borehole, which indicates that its geometrical spreading is slower than a simple borehole.

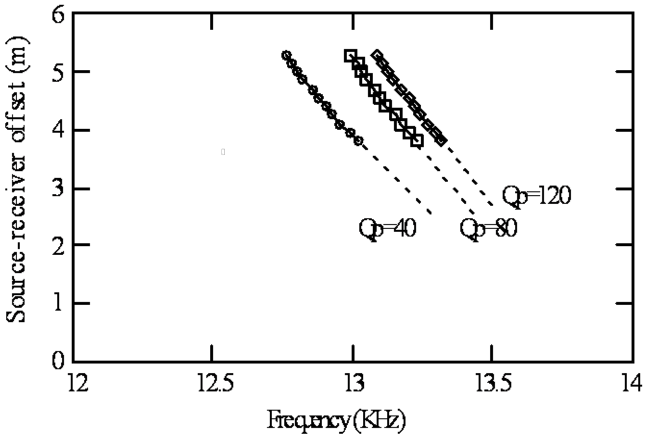

Figure 5.6 Centroid frequency picks corresponding to Q_p=40, Q_p=80 and Q_p=120 for the borehole with damaged zone.

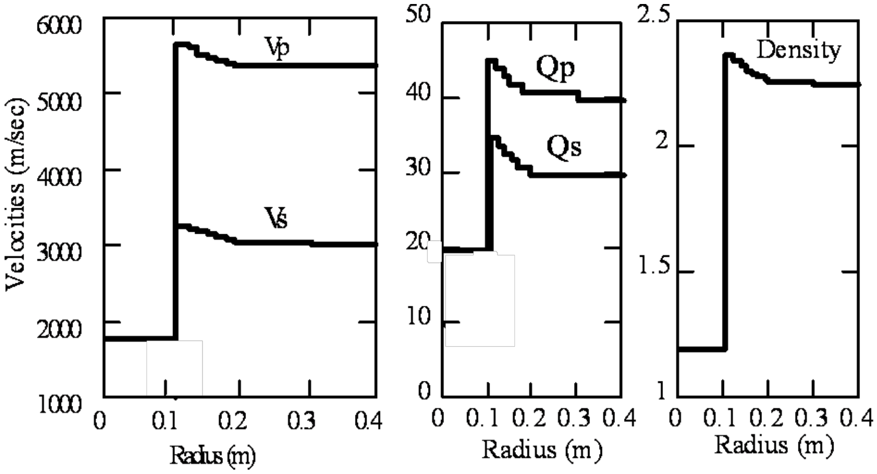

Figure 5.7a A flushed zone model. The velocity of the flushed zone gradually decreases until reach the formation velocity. The flushed zone is described by thin layers.

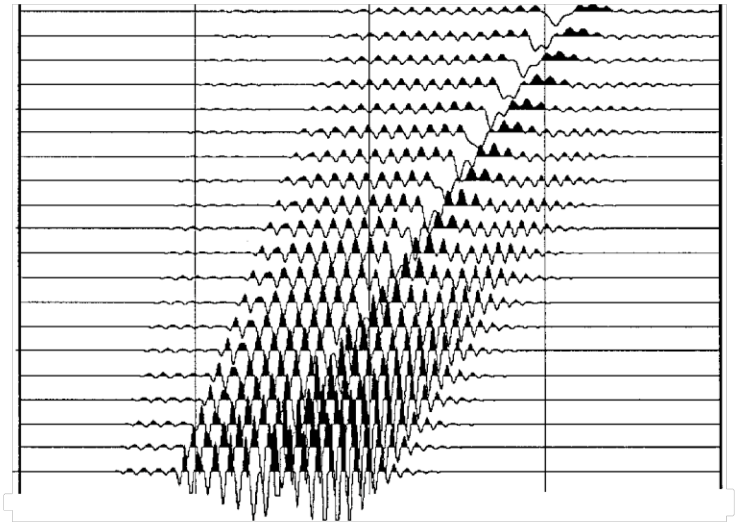

Figure 5.7b Micro-seismograms recorded in a borehole with a flushed zone. The amplitude of *P* wave decays significantly faster than that for the simple borehole, which indicates that its geometrical spreading effect is greater than a simple borehole.

Figure 5.8 Centroid frequency picks corresponding to Q_p=40, Q_p=80 and Q_p=120 for the borehole with *flushed* zone.

Another typical invaded zone is the flushed zone. Figure 5.7a shows such a model. Figure 5.7b is the micro-seismograms in a common source gather for this model in which Q_p = 45–40. Similarly, I calculate seismograms for Q_p = 85–80 and 125–120 as two other synthetic data sets. Figure 5.8 gives the centroid frequency picks for this *flushed* zone model corresponding to different Q_p values.

Applying equation (5.7) to the centroid frequency picks in Figures 5.6 (the damaged zone model) and Figure 5.8 (the flushed zone model), I obtain the estimated $\hat{Q}_p$'s which are shown in Table 5.2. It can be seen that the estimated $\hat{Q}_p$'s are far smaller than the given Q_p 's for these two types of models. These experiments show that the geometrical spreading in a borehole with the invaded zone is more complex than in a simple borehole. The frequency-dependent term $\exp(-\alpha_g f z_{i+1})$ in equation (5.3) is too simple to describe the complicated geometrical spreading, since it is not possible to find a common correction α_g to recover all the estimated $\hat{Q}_p$'s to the predicted values. Because of the complicated geometrical spreading, we have difficulty to used the frequency shift method calculating attenuation logs for boreholes with invaded zones.

Table 5.2 Estimation of Q_p for open boreholes with invaded zones

Given Q_p	40	80	120
Estimated $\hat{Q}_p$ (damaged zone, α_g=0)	15	17	19
Estimated $\hat{Q}_p$ (flushed zone, α_g=0)	25	36	58

5.3 APPARENT GEOMETRICAL SPREADING OF THE *P* WAVE IN COMPLICATED BOREHOLES

The simulation tests in the previous section show that the frequency-dependent geometrical spreading is complicated in boreholes with invaded zones. It is difficult to determine the details of its frequency-dependent property. In this section I assume an *apparent* geometrical spreading factor expressed by $1/z^p$. This assumption means that the effect of the frequency-dependent term exp($-\alpha_g f z$) will be included into $1/z^p$ by selecting a proper power *p*. For a monopole source in a simple borehole, the geometrical spreading factor is $1/z$ for the *P* wave (Roever et al., 1974; Winbow, 1980). With the more efficient algorithm, I investigate the effect of complex invaded zones on the *P* wave geometrical spreading, i.e., to determine the power *p* for the complicated boreholes. Ignoring α_g and rearranging equation (5.4) yield

$$p = \frac{1}{\log\left[\frac{z_{i+1}}{z_i}\right]}\left\{\log\left[\frac{R_i(f)}{R_{i+1}(f)}\right] - \alpha_{oi} f (z_{i+1} - z_i)\right\}. \tag{5.9}$$

I use equation (5.9) to estimate *p* from given model parameters and the synthetic micro-seismograms (Figures 5.3b, 5.5b and 5.7b) calculated in previous section.

Three types of borehole models shown in Figures 5.3a (simple borehole), 5.5a (borehole with damaged zone), 5.7a (borehole with flushed zone) are used for this apparent geometrical spreading study. For each model, three *P* wave *Q*-values (Q_p=40, 80 and 120) are used to calculate three synthetic data sets. I use a Hanning window to extract the *P* wave (first arrival) and perform FFT to obtain the spectrum $R_i(f)$. The peak spectrum amplitude $R_i(f_{peak})$ and the given model parameters are plugged into equation (5.9) to calculate the power *p* in the geometrical spreading factor $1/z^p$. With multiple data sets (corresponding to Q_p=40, 80 and 120) and multiple source–receiver pairs, we calculate several values of *p*'s by equation (5.9), and average these values to obtain the estimated power *p* in $1/z^p$. The estimated results for three different borehole models are summarized in Table 5.3.

Table 5.3 Estimation of *p* in the apparent geometrical spreading factor *1/zp*

borehole types	Simple	Damaged zone	Flushed zone
Estimated *p*	1	0.5	1.21

For the simple open borehole model, I obtain p=1, which is the same as what was obtained by Roever et al. (1974) and Winbow (1980). It can be seen from Figure 5.3b that the invaded zone exhibits a significant effect on the wave trains. The amplitude of the P wave becomes relatively higher when the invaded zone is present. Due to the convergent effect of an increasing velocity zone (invaded zone) on the refracted wave (P wave), the apparent geometrical spreading is slower than that for a simple borehole. The estimated power of geometrical spreading is p=0.5 for this particular damaged zone model. The flushed zone also has significant influence on the wave trains. It is clearly shown in Figure 5.7b that the geometrical spreading for this flushed zone model is greater than that for a simple borehole model, because of the divergent effect of the decreasing velocity zone (flushed zone) on the refracted wave. The estimated power of geometrical spreading factor is p =1.21 for this particular flushed zone. These three different borehole models exhibit different geometrical spreading factors, $1/z^p$, for the P wave. In summary, p=1 for a simple borehole model; p <1 for a damaged zone model; and p>1 for a flushed zone model.

The amplitude decay method has been used to measure attenuation coefficient α_o from acoustic logs (e.g., Cheng et al., 1982). Equation (5.9) can be rewritten as

$$\alpha_{oi} = \frac{1}{f(z_{i+1} - z_i)} \log \left[\frac{R_i(f) z_i^p}{R_{i+1}(f) z_{i+1}^p}\right]. \tag{5.10}$$

If the geometrical spreading factor $1/z^p$ is known, equation (5.10) can be used for attenuation estimation. All previous work on attenuation logging used p=1, which was obtained using the simple borehole model, for the geometrical spreading correction. From the study above we know that the invaded zones have strong effects on geometrical spreading. To understand how the invaded zones affect the attenuation estimation based on equation (5.10), let us compare the estimated Q_p values using the geometrical spreading correction $1/z$ with those using the correction $1/z^{0.5}$ for damaged zone model and the correction $1/z^{1.21}$ for flushed zone model. The peak spectrum amplitude $R_i(f_{peak})$ obtained from the micro-seismograms are used as data for equation (5.10) to estimate the P wave attenuation Q_p. Tables 5.4–5.6 show the estimated results of Q_p values for the simple open borehole model, damaged zone model and the flushed zone model, respectively. It can be seen from Tables 5.4–5.6 that the estimation of attenuation using the amplitude decay method is very sensitive to the errors in geometrical spreading correction. This study reveals that for boreholes with invaded zones we may not simply use $1/z$ as the geometrical correction, though it is correct for the simple borehole, otherwise the attenuation could not be correctly estimated.

Table 5.4 Estimation of geometrical spreading $1/z^p$ and intrinsic attenuation $1/Q$ for the simple open borehole

Given Q_p	40	80	120
$1/z$	40	81	122

Table 5.5 Estimation of geometrical spreading $1/z^p$ and intrinsic attenuation $1/Q$ for the damaged zone model

Given Q_p	35–40	75–80	115–120
$1/z$	90	< 0	< 0
$1/z^{0.5}$	39	80	129

Table 5.6 Estimation of geometrical spreading $1/z^p$ and intrinsic attenuation $1/Q$ for the flushed zone model

Given Q_p	40	80	120
$1/z$	31	52	67
$1/z^{1.21}$	40	80	118

5.4 AN EXAMPLE OF FIELD DATA

The full waveform acoustic log measured at McElroy Well #1202 is used as a test on the attenuation log by the centroid frequency shift method. The data set is collected at each 6 inches in the borehole using a standard sonic tool which consists of a source and a receiver array. The source receiver offsets are 8 – 11 feet. I assume that the borehole has no invaded zones, and apply equation (5.7) to this sonic log data set. Figure 5.9a is the calculated *P* wave *Q* log ($Q=\pi/v\alpha_o$, where α_o is the attenuation coefficient). Figure 5.9b is the waveform log (micro-seismogram) recorded at the first channel of the receiver array. The slower travel time in Figure 5.9b means lower *P* wave velocity at that depth; and faster travel time means higher *P* wave velocity at that depth. Therefore, Figure

5.9b, in fact, shows the velocity structure of the borehole. Although Figure 5.9a is only a preliminary test on *Q*-log, it exhibits a overall good correlation with velocity structure shown in Figure 5.9b, i.e., high *Q*-value corresponds to high velocity (or fast travel time) and low *Q*-value corresponds to low velocity (or slow travel time). The inconsistency around depth of 2750 feet may means that the rock at that depth has some special properties.

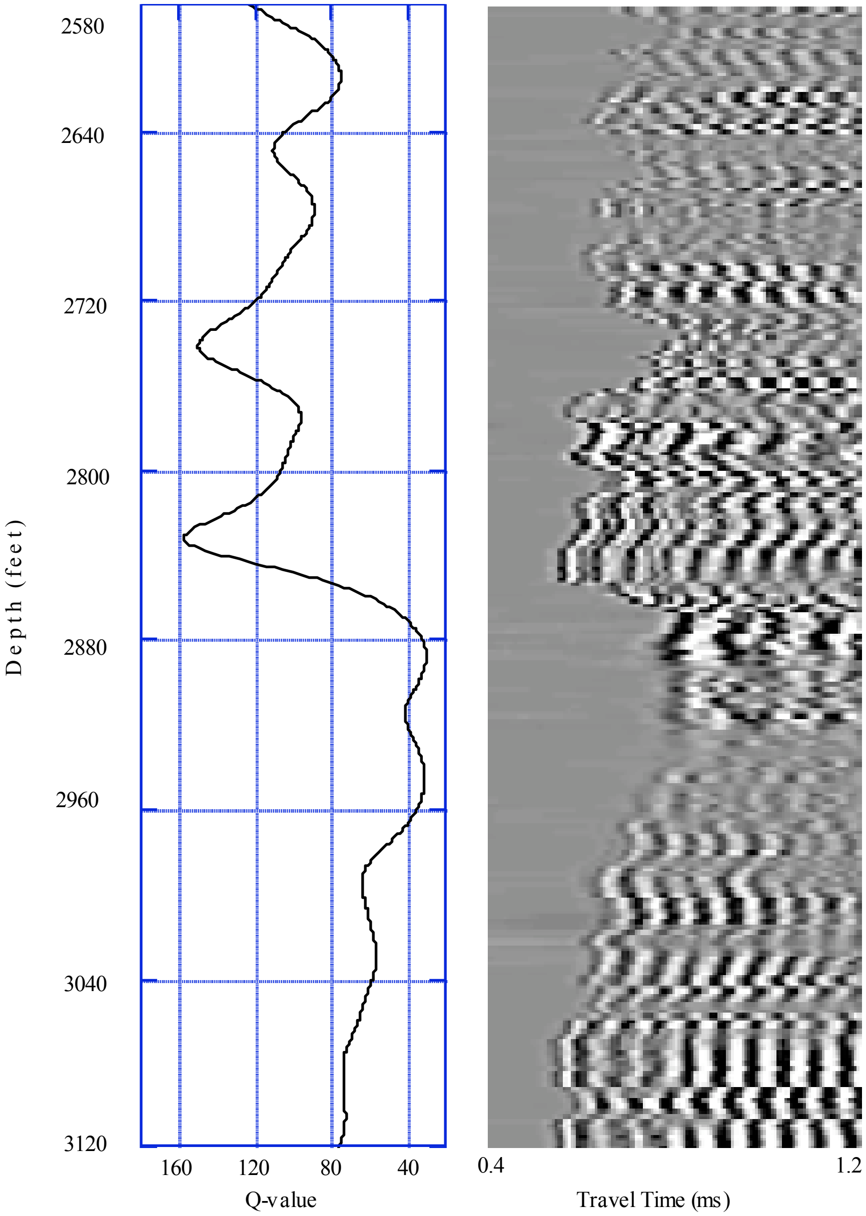

(a) *P* wave *Q*-log (b) Waveform log

Figure 5.9 (a) A Q_p log for McElroy Well #1202, obtained by the frequency shift method. (b) The waveform log for comparison. At each depth, only the first trace recorded in receiver array is shown.

5.5 CONCLUSIONS

The generalized reflection and transmission coefficients method is applied to numerically investigate seismic wave attenuation in the simple open borehole and complicated boreholes with invaded zones. In order to measure the intrinsic attenuation we need to remove the geometrical spreading effect which is complex and highly frequency-dependent. If we use the frequency shift method to estimate intrinsic attenuation for a simple open borehole, we can introduce a frequency-dependent geometrical spreading factor, $\exp(-\alpha_g f z)$, to do the correction (but only for open hole).

It is difficult to determine the details of the frequency-dependent geometrical spreading for the complicated boreholes. I introduce an *apparent* geometrical spreading factor expressed by $1/z^p$, which may approximately include the effect of the frequency-dependent term $\exp(-\alpha_g f z)$ if we select a proper power p. Simulation tests show that the power $p=1$ for a simple borehole, $p<1$ for a damaged zone model, and $p>1$ for a flushed zone model. How large the power p deviates from 1 depends on the structure of the invaded zones, such as the velocity contrast and the invaded depth. For the specific borehole models investigated in this chapter, $p=0.5$ for the invaded zone model and $p=1.21$ for the flushed zone model.

Normal Modes in Radially Layered Media and Application to Attenuation Estimation

The *P* wave in acoustic full waveform logs can be used to estimate *P* wave attenuation (see Chapter 5). But it is difficult to estimate *S* wave attenuation from the *S* wave in acoustic logs. The *S* wave is immediately followed by tube waves. It is difficult or impossible to separate the *S* wave train from acoustic logs. An alternative way to estimate *S* wave attenuation is to use tube waves, or normal modes. In this chapter, the generalized reflection and transmission coefficients method introduced in Chapter 2 is further developed to systematically determine normal modes in radially multi-layered media. This approach can simultaneously determine both phase velocities and corresponding eigen functions for a borehole with an arbitrary number of radial layers. Therefore, it can simulate tube waves for the cased borehole and the invaded borehole. A formula which describes the attenuation property of each mode in absorptive media is derived. We can use this formula to estimate the *S* wave attenuation from tube waves, especially the pseudo-Rayleigh wave.

6.1 INTRODUCTION

The dispersion relation, which gives the phase velocities of normal modes, is very important for studying guided waves in acoustic logging. It has been studied by many authors, e.g., Biot (1952), Cheng and Toksöz (1981). In this chapter the generalized reflection and transmission (R/T) coefficients method is further developed to systematically and simultaneously determine the phase velocities and eigen functions of normal modes in radially multi-layered media. These normal modes are known as the Stoneley wave and pseudo Rayleigh waves. Chen (1993) used the generalized R/T coefficients method to compute normal modes in horizontal layers.

If we know the relationship between the *Q*-value of a normal mode and the *Q*-value of the formation, we may estimate the formation *Q*-value from that mode using this relation. Cheng et al. (1982) gave a formula describing the attenuation of tube waves for a simple open borehole. In this chapter, a more general formula to calculate the attenuation of each normal mode for a cased borehole and other complicated boreholes is derived from the new dispersion relation. Additionally, I use a numerical example demonstrating how to estimate the *S* wave attenuation from tube waves.

6.2 NORMAL MODES IN RADIALLY LAYERED MEDIA

The normal modes are the non-trivial solutions of the source-free elastodynamic equation under given boundary conditions. Starting from this point, we can derive an effective algorithm to determine the phase velocities and the corresponding eigen functions of the normal modes in radially layered media. Figure 2.1 shows such a radially multi-layered model. In the acoustic logging problem, these normal modes are known as tube waves or guided waves. In the *source-free* case, the elastodynamic equation can be written as

$$\rho \ddot{\mathbf{u}}(\mathbf{x},t) = (\lambda + 2\mu)\nabla\nabla \cdot \mathbf{u}(\mathbf{x},t) - \mu \nabla \times \nabla \times \mathbf{u}(\mathbf{x},t), \qquad (6.1)$$

namely, set the source function **f** in equation (2.1) to zero**.** Then, similar to the formulation given in Chapter 2, we can obtain the radial and vertical components of the displacements ($\hat{u}_k^{(j)}$ and $\hat{w}_k^{(j)}$) and the stresses ($\hat{\sigma}_k^{(j)}$ and $\hat{\tau}_k^{(j)}$). For the first layer (i.e., *j*=1, the liquid layer), the displacement and the stress are

$$\begin{bmatrix} \hat{u}_k^{(1)}(r) \\ \hat{\sigma}_k^{(1)}(r) \end{bmatrix} = \begin{bmatrix} e_{11}^{(1)}(r) & e_{12}^{(1)}(r) \\ e_{21}^{(1)}(r) & e_{22}^{(1)}(r) \end{bmatrix} \begin{bmatrix} c_{p-}^{(1)} \\ c_{p+}^{(1)} \end{bmatrix}, \tag{6.2a}$$

where the explicit expressions of the elements $\{e_{nm}^{(1)}\}$ are given in the Appendix A-4. Note that the source term in (6.2a) is zero in this case. For *j*= 2, ..., *N*, the expressions for displacements and stresses in a solid layer are

$$\begin{bmatrix} \hat{u}^{(j)}(r) \\ \hat{w}^{(j)}(r) \\ \hat{\sigma}^{(j)}(r) \\ \hat{\tau}^{(j)}(r) \end{bmatrix} = \begin{bmatrix} e_{11}^{(j)}(r) & e_{12}^{(j)}(r) & e_{13}^{(j)}(r) & e_{14}^{(j)}(r) \\ e_{21}^{(j)}(r) & e_{22}^{(j)}(r) & e_{23}^{(j)}(r) & e_{24}^{(j)}(r) \\ e_{31}^{(j)}(r) & e_{32}^{(j)}(r) & e_{33}^{(j)}(r) & e_{34}^{(j)}(r) \\ e_{41}^{(j)}(r) & e_{42}^{(j)}(r) & e_{43}^{(j)}(r) & e_{44}^{(j)}(r) \end{bmatrix} \begin{bmatrix} c_{p_-}^{(j)} \\ c_{s_-}^{(j)} \\ c_{p_+}^{(j)} \\ c_{s_+}^{(j)} \end{bmatrix}. \tag{6.2b}$$

where the explicit expressions of the elements $\{e_{nm}^{(j)}\}$ are given in the Appendix A-4. In the outer most layer, i.e., *j*=*N*+1, there are only out going waves. Therefore, the displacements and stresses in the outer most layer are

$$\begin{bmatrix} \hat{u}^{(N+1)}(r) \\ \hat{w}^{(N+1)}(r) \\ \hat{\sigma}^{(N+1)}(r) \\ \hat{\tau}^{(N+1)}(r) \end{bmatrix} = \begin{bmatrix} e_{13}^{(N+1)}(r) & e_{14}^{(N+1)}(r) \\ e_{23}^{(N+1)}(r) & e_{24}^{(N+1)}(r) \\ e_{33}^{(N+1)}(r) & e_{34}^{(N+1)}(r) \\ e_{43}^{(N+1)}(r) & e_{44}^{(N+1)}(r) \end{bmatrix} \begin{bmatrix} c_{p_+}^{(N+1)} \\ c_{s_+}^{(N+1)} \end{bmatrix}, \tag{6.2c}$$

where, signs "+" and "-" refer to outgoing and incoming waves, respectively. Unknown coefficients, $c_{p\pm}^{(j)}$ and $c_{s\pm}^{(j)}$), can be determined by imposing the boundary conditions at interfaces. Since the source function is zero in this case, choosing $c_{p\pm}^{(j)} = c_{s\pm}^{(j)} = 0$ would give a solution, but it is only a trivial solution. What we look for are non-trivial solutions under the given boundary conditions. These non-trivial solutions are called normal modes. In this chapter, I apply the generalized reflection and transmission (R/T) coefficients method to find these normal modes.

The generalized R/T matrices, $\overset{?}{\mathbf{R}}_{+-}^{(j)}$ and $\overset{?}{\mathbf{T}}_{+}^{(j)}$, are introduced in Section 2.3 to determine coefficients $c_{p\pm}^{(j)}$ and $c_{s\pm}^{(j)}$. Matrices $\overset{?}{\mathbf{R}}_{+-}^{(j)}$ and $\overset{?}{\mathbf{T}}_{+}^{(j)}$ are determined by a recursive relation [equation (2.16) with initial condition (2.17)]. In this source-free case, we can not use equation (2.18) to determine $c_{p\pm}^{(j)}$ and $c_{s\pm}^{(j)}$. from the generalized R/T matrices, since the source term $s_+=0$. Let us now derive the formula for the source-free case, i.e., the solution of normal modes.

Coefficients $c_{p\pm}^{(j)}$ and $c_{s\pm}^{(j)}$ for each layer can be related by the generalized R/T matrices as follows,

$$\begin{cases} \mathbf{c}_{+}^{(j+1)} = \overset{?}{\mathbf{T}}_{+}^{(j)}\mathbf{c}_{+}^{(j)} \\ \mathbf{c}_{-}^{(j)} = \overset{?}{\mathbf{R}}_{+-}^{(j)}\mathbf{c}_{+}^{(j)} \end{cases} \qquad \text{for } j = 2, 3, ..., N; \tag{6.3a}$$

and

$$\begin{cases} \mathbf{c}_{+}^{(2)} = \overset{?}{\mathbf{T}}_{+}^{(1)}c_{+}^{(1)} \\ c_{-}^{(1)} = \overset{?}{R}_{+-}^{(1)}c_{+}^{(1)} \end{cases}, \tag{6.3b}$$

where $\mathbf{c}_{\pm}^{(j)} = [c_{p\pm}^{(j)}, c_{s\pm}^{(j)}]^{\mathrm{T}}$ for j=2, 3, ..., N+1, and $c_{\pm}^{(1)} = c_{p\pm}^{(1)}$. If the first layer is a fluid-filled borehole (the acoustic logging problem), $\overset{?}{\mathbf{R}}_{+-}^{(1)}$ becomes a scalar $\overset{?}{R}_{+-}^{(1)}$. The non-singular condition at r=0, i.e., the incoming wave in the borehole is represented by the zero order Bessel function J_o [see equation (2.7)], implies

$$c^{(1)}_{p+} = c^{(1)}_{p-} e^{i v^{(1)}_{\alpha} r^{(1)}} . \qquad (6.4)$$

It can be seen that once the coefficient $c^{(1)}_{p+}$ in the fluid-filled layer is determined, then all other coefficients can be calculated through equation (6.2). Therefore, let us determine $c^{(1)}_{p+}$ first. Substituting (6.4) into the second equation in (6.3b), we obtain

$$(1 - e^{i v^{(1)}_{\alpha} r^{(1)}} \overset{?}{R}{}^{(1)}_{+-}) c^{(1)}_{p+} = 0 .$$

In order to obtain a non-trivial solution we must have $c^{(1)}_{p+} \neq 0$, which leads to

$$1 - e^{i v^{(1)}_{\alpha} r^{(1)}} \overset{?}{R}{}^{(1)}_{+-} = 0 . \qquad (6.5)$$

For a given angular frequency ω, only certain wave numbers k_n, n=1, 2, ..., $K(\omega)$, which are roots of equation (6.5), satisfy equation (6.5). These roots constitute the normal modes for given boundary conditions. The phase velocities v_n of these modes are calculated by the relation

$$v_n = \frac{\omega}{k_n}, \qquad n=1, 2, ..., K(\omega), \qquad (6.6a)$$

and the group velocities c_n are obtained through the relation

$$c_n = \frac{\partial \omega}{\partial k_n}, \qquad n=1, 2, ..., K(\omega) . \qquad (6.6b)$$

Therefore, equation (6.5) is a dispersion relation whose roots give phase velocities and group velocities of normal modes for a given frequency. This dispersion relation is very simple and can be easily solved.

Once we obtain the phase velocity of a normal mode, we can calculate its eigen function. According to equation (6.4), $c_{p+}^{(1)}$ can be any non-zero value. Without any loss of generality, I set $c_{p+}^{(1)}(v_n) = 1$. Then, all other coefficients are obtained using the generalized R/T matrices through the following relations:

$$c_{p-}^{(1)}(v_n) = \hat{R}_{+-}^{(1)}(v_n)\ ,$$

and

$$\begin{cases} \mathbf{c}_{+}^{(j+1)}(v_n) = \hat{\mathbf{T}}_{+}^{(j)}(v_n)\hat{\mathbf{T}}_{+}^{(j-1)}(v_n)\ldots\hat{\mathbf{T}}_{+}^{(1)}(v_n) \\ \mathbf{c}_{-}^{(j+1)}(v_n) = \hat{\mathbf{R}}_{+-}^{(j+1)}(v_n)\mathbf{c}_{+}^{(j+1)}(v_n) \end{cases}, \quad j=1, 2, \ldots, N. \tag{6.7}$$

Substituting these coefficients into equation (6.2), we obtain corresponding eigen functions. Dispersion relation (6.5) along with equations (6.6) and (6.7) are very important for studying normal modes. In the next section, I apply this dispersion relation to seismic attenuation estimation.

6.3 *Q*-VALUES OF NORMAL MODES

In the previous section, I only consider the lossless case, i.e., the *Q*-value for all waves is infinite. The *Q*-value in real media is finite, i.e., there exists attenuation. For an absorptive medium, the attenuation can be introduced via the complex velocity

$$\hat{v}(\omega) = v(\omega)[1 - \frac{i}{2Q}] \tag{6.8}$$

The real part of the velocity represents the wave propagation speed; and the imaginary part of the velocity causes the exponential decay of the amplitude as the wave propagates. Once the real *P* and *S* velocities (α_j, β_j) for each layer are replaced by the complex velocities $(\tilde{\alpha}_j, \tilde{\beta}_j)$, the corresponding phase velocities are complex too (i.e., roots of equation (6.5) become complex numbers). Assume that the complex phase velocity of the n^{th} mode is described by equation (6.8), i.e.,

$$\tilde{v}_n(\omega) = v_n(\omega)[1 - \frac{i}{2Q_n}], \tag{6.9}$$

where $v_n(\omega)$ is the real phase velocity. Then, the dispersion equation (6.5) can be written in terms of complex velocities $\tilde{\mathbf{v}}_\mathbf{p}$ and $\tilde{\mathbf{v}}_\mathbf{s}$:

$$1 - \Delta[\tilde{v}_n(\omega), \tilde{\mathbf{v}}_\mathbf{p}, \tilde{\mathbf{v}}_\mathbf{s}] = 0, \tag{6.10}$$

where

$$\Delta[\tilde{v}_n(\omega), \tilde{\mathbf{v}}_\mathbf{p}, \tilde{\mathbf{v}}_\mathbf{s}] = e^{i v_\alpha^{(1)} r^{(1)}} \tilde{R}_{+-}^{(1)}[\tilde{v}_n(\omega), \tilde{\mathbf{v}}_\mathbf{p}, \tilde{\mathbf{v}}_\mathbf{s}],$$

$$\tilde{\mathbf{v}}_\mathbf{p} = (\tilde{\alpha}_1, \tilde{\alpha}_2, \ldots, \tilde{\alpha}_{N+1})$$

and

$$\tilde{\mathbf{v}}_\mathbf{s} = (\tilde{\beta}_1, \tilde{\beta}_2, \ldots, \tilde{\beta}_{N+1})$$

are complex *P* and *S* velocities of all layers. Considering $1/Q$ is small (usually less than 0.1), we can expand $\Delta[\tilde{v}_n(\omega), \tilde{\mathbf{v}}_\mathbf{p}, \tilde{\mathbf{v}}_\mathbf{s}]$ about $1/Q$ as

$$
\begin{aligned}
\Delta[\tilde{v}_n(\omega), \tilde{\mathbf{v}}_\mathbf{p}, \tilde{\mathbf{v}}_\mathbf{s}] = {} & \Delta[v_n(\omega), \mathbf{v}_\mathbf{p}, \mathbf{v}_\mathbf{s}] \\
& + \sum_{j=1}^{N+1} \frac{\partial\Delta[\tilde{v}_n(\omega), \tilde{\mathbf{v}}_\mathbf{p}, \tilde{\mathbf{v}}_\mathbf{s}]}{\partial\alpha_j}\Delta\alpha_j \\
& + \sum_{j=1}^{N+1} \frac{\partial\Delta[\tilde{v}_n(\omega), \tilde{\mathbf{v}}_\mathbf{p}, \tilde{\mathbf{v}}_\mathbf{s}]}{\partial\beta_j}\Delta\beta_j \\
& + \frac{\partial\Delta[\tilde{v}_n(\omega), \tilde{\mathbf{v}}_\mathbf{p}, \tilde{\mathbf{v}}_\mathbf{s}]}{\partial v_n}\Delta v_n + O\left(\frac{1}{Q^2}\right)
\end{aligned}
\tag{6.11}
$$

where $\Delta\alpha_j = \tilde{\alpha}_j - \alpha_j = -i\alpha_j / 2Q_{p_j}$, $\Delta\beta_j = -i\beta_j / 2Q_{S_j}$ and $\Delta v_n = -iv_n / 2Q_n$. Since v_n is the phase velocity of lossless case corresponding to real velocities ($\mathbf{v}_p$, $\mathbf{v}_s$), we have

$$
1 - \Delta(\mathbf{v}_\mathbf{p}, \mathbf{v}_\mathbf{s}, v_n) = 0\,. \tag{6.12}
$$

Substituting equation (6.11) into equation (6.10), neglecting the term $1/Q^2$ and other higher order terms, and using equation (6.12), we obtain the formula

$$
\begin{aligned}
\frac{1}{Q_n(\omega)} \cong -\sum_{j=1}^{N+1} & \left\{ \frac{\partial\Delta[\tilde{v}_n(\omega), \tilde{\mathbf{v}}_\mathbf{p}, \tilde{\mathbf{v}}_\mathbf{s}]}{\partial\alpha_j} \frac{\alpha_j}{v_n} \frac{1}{Q_{p_j}} + \right. \\
& \left. \frac{\partial\Delta[\tilde{v}_n(\omega), \tilde{\mathbf{v}}_\mathbf{p}, \tilde{\mathbf{v}}_\mathbf{s}]}{\partial\beta_j} \frac{\beta_j}{v_n} \frac{1}{Q_{S_j}} \right\} \Big/ \frac{\partial\Delta[\tilde{v}_n(\omega), \tilde{\mathbf{v}}_\mathbf{p}, \tilde{\mathbf{v}}_\mathbf{s}]}{\partial v_n}\,,
\end{aligned}
\tag{6.13}
$$

which gives the relationship between the Q-value of the n^{th} normal mode and the Q-values of P and S waves in all layers. Noticing that

$$
-\frac{\partial\Delta[\tilde{v}_n, \tilde{\mathbf{v}}_\mathbf{p}, \tilde{\mathbf{v}}_\mathbf{s}]}{\partial\alpha_j} \Bigg/ \frac{\partial\Delta[\tilde{v}_n, \tilde{\mathbf{v}}_\mathbf{p}, \tilde{\mathbf{v}}_\mathbf{s}]}{\partial v_n} = \frac{\partial v_n}{\partial\alpha_j}
$$

and

$$-\frac{\partial \Delta[\tilde{v}_n, \tilde{\mathbf{v}}_{\mathbf{p}}, \tilde{\mathbf{v}}_{\mathbf{s}}]}{\partial \beta_j} \Big/ \frac{\partial \Delta[\tilde{v}_n, \tilde{\mathbf{v}}_{\mathbf{p}}, \tilde{\mathbf{v}}_{\mathbf{s}}]}{\partial v_n} = \frac{\partial v_n}{\partial \beta_j} \ ,$$

we can write equation (6.13) in an alternative form:

$$\frac{1}{Q_n} \cong \sum_{j=1}^{N+1} \{ \frac{\partial v_n}{\partial \alpha_j} \frac{\alpha_j}{v_n} \frac{1}{Q_{P_j}} + \frac{\partial v_n}{\partial \beta_j} \frac{\beta_j}{v_n} \frac{1}{Q_{S_j}} \} . \tag{6.14}$$

For a simple fluid-filled open borehole, equation (6.14) becomes

$$\frac{1}{Q_n} \cong \frac{\partial v_n}{\partial \alpha_1} \frac{1}{Q_{P_1}} + \frac{\partial v_n}{\partial \alpha_2} \frac{1}{Q_{P_2}} + \frac{\partial v_n}{\partial \beta_2} \frac{\beta_2}{v_n} \frac{1}{Q_{S_2}} \ , \tag{6.15}$$

which is the same as the formula in Cheng et al. (1982). It should be emphasized that equation (6.15) is only a special case of equation (6.14). The method developed in this Chapter is a more general approach than Cheng et al. (1982). Equation (6.14) can be applied to a radially layered medium with an arbitrary number of layers. The formula in Cheng et al. (1982) is only for a simple open borehole.

Coefficients $(\partial v_n / \partial \alpha_j)(\alpha_j / v_n)$ and $(\partial v_n / \partial \beta_j)(\beta_j / v_n)$ in equations (6.14) are called partition coefficients which describe how sensitive the *Q*-value of a normal mode is to the *P* wave *Q*-value and *S* wave *Q*-value, respectively. If the partition coefficients are known, equation (6.14) is used to estimate the formation *Q*-value from normal modes or tube waves.

6.4 NUMERICAL EXAMPLES

In this section, the dispersion relation [equation (6.5)], tube wave attenuation [equation (6.14)], and the attenuation estimation from the pseudo-Rayleigh wave are tested for three typical radially layered models: the simple open borehole, the borehole with a damaged zone, and the borehole with a flushed zone. Table 6.1 shows parameters of these three models.

6.4.1 Normal Modes

Let $d(f,k) = |1 - \Delta(f,k)|$. A plot of $d(f,k)$ is helpful to see what is the root distribution, and what the normal mode looks like in the $f-k$ domain. Figures 6.1-6.3 show plots for the three models given in Table 6.1. In these plots, M1, M2, ..., etc. indicate zeros or roots of $d(f, k)$, i.e., the normal modes. M1 is the Stoneley wave, and M2, M3, ..., etc. are pseudo-Rayleigh waves. R1, R2, ..., etc. are resonances (Schmitt and Bouchon, 1985). These resonances are only local minimums, not roots. The coordinates (f, k) corresponding to modes M1, M2, ..., etc. can be used to calculate phase velocities of these modes using equation (6.6a). In the next example, I use the phase velocity of the fundamental pseudo-Rayleigh wave (M2) to find its Q-value.

Table 6.1 Model parameters

	Fluid	Casing or Invaded zone	Formation
Simple Borehole	r=12cm α=1.5km/s ρ=1.0	——	α=4.9km/s β=2.8km/s ρ=2.4
Cased Borehole	r=10cm α=1.5km/s ρ=1.0	r=11.5cm α=6.1km/s β=3.4km/s ρ=7.8	α=4.9km/s β=2.8km/s ρ=2.4

Invaded Borehole	*r*=12cm α=1.5km/s ρ=1.0	*r*=19cm α=3.8km/s β=2.5km/s ρ=2.2	α=4.9km/s β=2.8km/s ρ=2.4

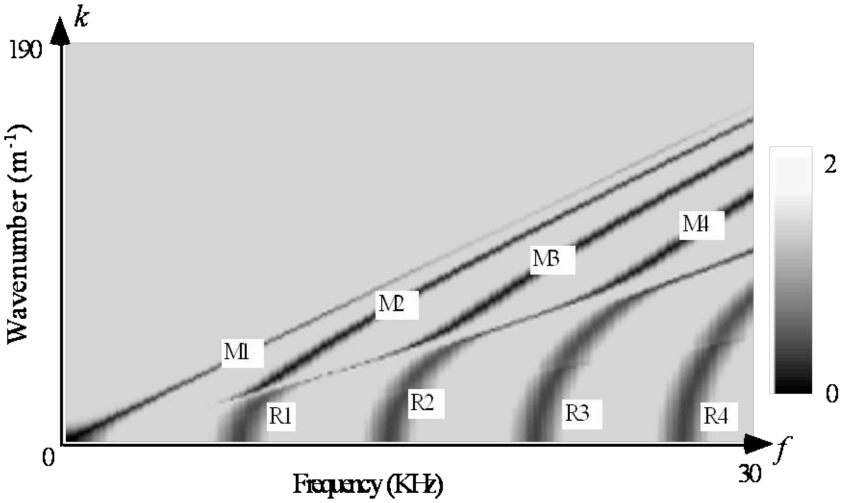

Figure 6.1 A plot of the function $d(f,k)=|1-\Delta(f,k)|$ for the *simple* open borehole.

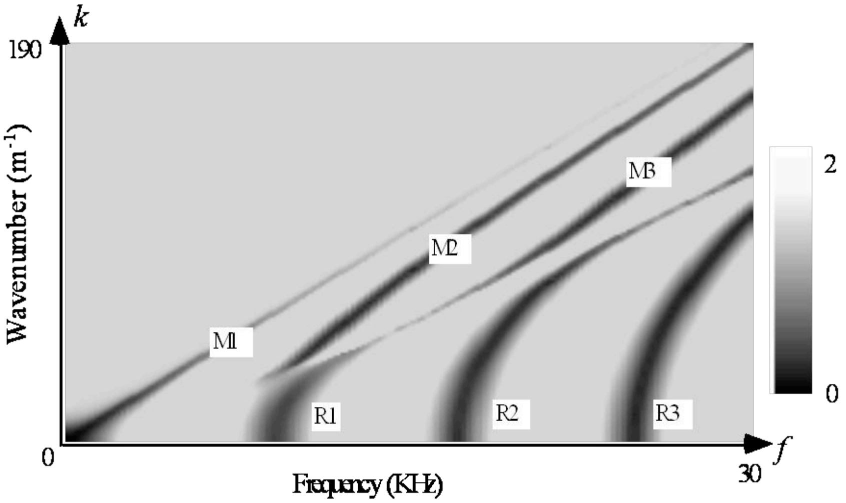

Figure 6.2 A plot of the function $d(f,k)=|1-\Delta(f,k)|$ for the *cased* borehole.

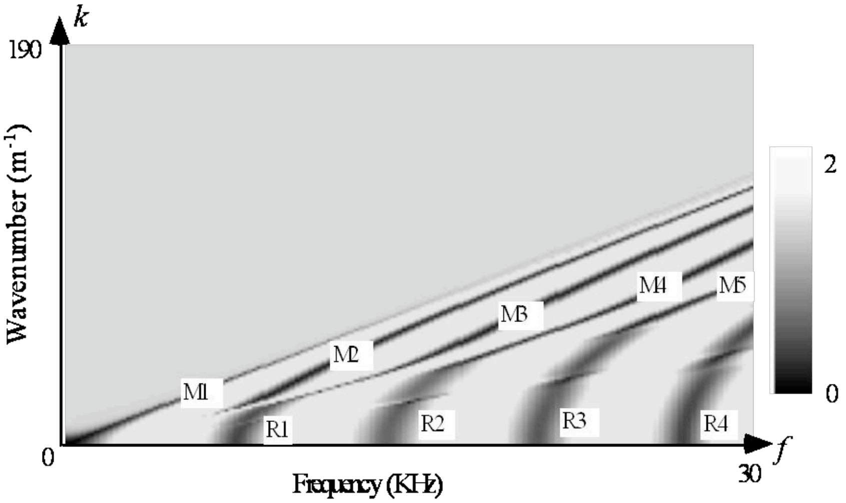

Figure 6.3 A plot of function $d(f,k)=|1-\Delta(f,k)|$ for the borehole with an *invaded* zone.

6.4.2 Attenuation of the Pseudo-Rayleigh Wave (MODE M2)

The dependence of *Q*-value of mode M2 on the *Q*-value of the *S* wave in the formation is shown in Figure 6.4 by the partition coefficient $(\partial v_2 / \partial \beta)(\beta / v_2)$ [see equation (6.14)]. It can be seen that this coefficient is sensitive to Q_S at the cutoff frequency. This provides an opportunity to calculate Q_s from Q_2 using equation (6.14). Similarly, we can calculate the partition coefficients for the formation *P* wave and the fluid *P* wave. The partition coefficient for the formation *P* wave is negligible at all frequencies, which means that Q_2 is almost independent of Q_p. Therefore, it is impossible to estimate Q_p from Q_2. This independence of Q_p, however, makes the estimation of Q_s from equation (6.14) more accurate, due to $(\partial v_2 / \partial \alpha)(\alpha / v_2) \approx 0$. The next test shows how to estimate Q_S from Q_2 near the cutoff frequency for the simple borehole.

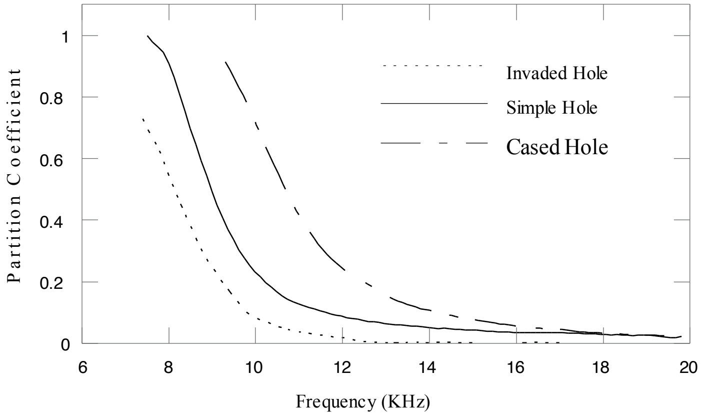

Figure 6.4 Attenuation partition coefficients for the three borehole models.

6.4.3 Attenuation Estimation from the Pseudo-Rayleigh Wave

A linear sweep with the frequency band of 0.1-29 KHz is used as the source to calculate a synthetic excitation log (Medlin & Schmitt, 1992) for the simple borehole model given in Table 6.1. Figure 6.5 shows the excitation log which is the borehole response to a source with a flat spectrum. Around f=9.5 KHz there is a peak on the excitation log. This frequency is close to the cutoff frequency of the fundamental pseudo-Rayleigh wave. Then, I run a short sweep of 1.2 ms long with a frequency band of 9-9.5 KHz. This gives an enhanced pseudo-Rayleigh wave shown in Figure 6.6. Using the amplitude ratio method [equation (5.10) with p=1], I find that the estimated Q_{PR} =130. The given S wave Q_S is 80, and Q-values of other waves are infinite. Figure 6.4 shows that the partition coefficient is about 0.45 for this case. Then, I get the estimated Q_S=60. The pseudo-Rayleigh wave is dominant in Figure 6.6. But other waves, e.g., the Stoneley wave, direct P and S waves are also in it, though they are weak. This is one of the possible reasons why the estimated Q_S is smaller than the given value.

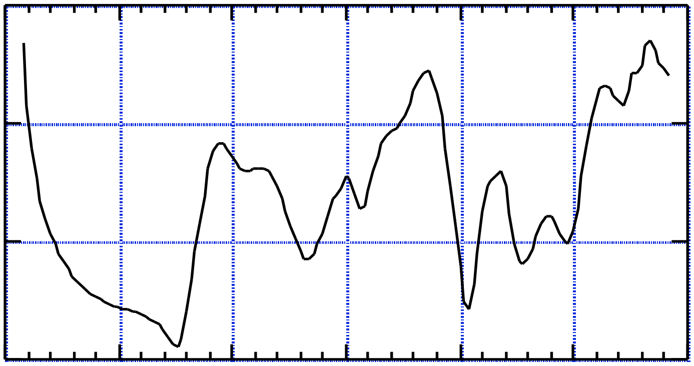

Figure 6.5 Excitation log for the simple borehole.

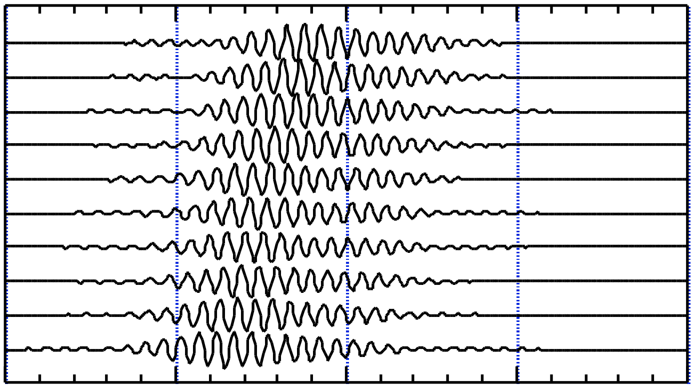

Figure 6.6 The enhanced fundamental mode of the pseudo-Rayleigh wave near the cutoff frequency (9.5 KHz) for the simple borehole model.

6.5 CONCLUSIONS

A new method based on the generalized reflection and transmission coefficients is developed to determine the dispersion relation of normal modes in radially layered media. In the acoustic logging problem, the normal modes are called tube waves. The algorithm of this method is very efficient, and it can be applied to a borehole model that has an arbitrary number of radial layers. With this dispersion relation, we can simultaneously compute the phase/group velocities and eigen functions of these normal modes. Also, a formula that describes the relationship between the attenuation of a mode and the attenuation of *P* and *S* waves is derived from the this dispersion relation. Thus, normal modes, especially the pseudo-Rayleigh wave, can be used to estimate the *S* wave attenuation according to this formula.

References

Aki, K, and Richards, P., G., 1980, *Quantitative Seismology, Theory and Methods*: W.H. Freeman and Co., San Francisco.

Apsel, R., 1979, Dynamic Green's functions for layered media and applications to boundary-value problems: Ph.D. Thesis, University of California at San Diego.

Baker, L., J., 1984, The effect of the invaded zone on the full wavetrain acoustic logging: Geophysics, **49**, Pages 789 - 809.

Best, A. I., McCann, C., and Sothcott, J., 1994, The relationships between the velocities, attenuations, and petrophysical properties of reservoir sedimentary rocks: Geophys. Prosp., **42**, Pages 151-178.

Biot, M. A., 1952, Propagation of elastic waves in a cylindrical bore containing a fluid: J. Appl. Physics, **23**, 997-1005.

Bouchon, M., 1993, A numerical simulation of the acoustic and elastic wavefields radiated by a source on a fluid-filled borehole embedded in layered medium: Geophysics, **58**, No. 4, 475-481.

Bouchon, M. and Aki, K., 1977, Discrete wavenumber presentation of seismic-source wave fields: Bull. Seism. Soc. Am, **67**, 259-277.

Bracewell, R., 1986, The Fourier Transform and Its Applications: McGraw-Jill Publishing Company.

Brzostowski, M. & McMechan, G., 1992, 3-D tomographic imaging of near-surface seismic velocity and attenuation: Geophysics, **57**, No. 3, 396-403.

Chen, S. T., 1993, A single well profiling tool an tube-wave suppression, Expanded Abstracts of the 63th SEG meeting.
\
Chen, S. T., M. A. Miller and L. J. Zimmerman, 1994, Single-well profiling tool with a variable downhole source/receiver spacer: Expanded Abstracts of the 64th SEG meeting.

Chen, X., 1991, Seismogram synthesis for multi-layered media with irregular interfaces by the global generalized reflection/transmission matrices method: Ph.D. Thesis, University of Southern California.

Chen, X., Quan, Y. and Harris, M. J., 1996, Seismogram synthesis for radially layered media using the generalized reflection/transmission coefficients method - theory and applications to acoustic logging: Geophysics, 61, No 4

Chen, X., Quan, Y. and Harris, M. J., 1994, Seismogram synthesis for radially layered media using the generalized reflection/transmission coefficients method: Expanded Abstracts of the 64th SEG annual meeting.

Chen, X., 1993, A systematic and efficient method of computing normal modes for multi-layered half-space: Geophys. J. International, **115**, 391-409.

Cheng, C. H., , M. N. and Willis, M. E., 1982, Determination of In situ attenuation from full waveform acoustic logs: J. Geophys. Res., **87**, No. B7, 5477 - 5484.

Cheng, C. H. and , M. N., 1981, Elastic wave propagation in a fluid-filled borehole and synthetic acoustic logs: Geophysics, **46**, No. 7, 1042-1053.

Dines, K. & Kak, A., 1979, Ultrasonic attenuation tomography of soft tissues: Ultrasonic Imaging, **1**, No 1, 16-33.

Dong, W., Bouchon, M. and , M. N., 1995, Borehole seismic-source radiation in layered isotropic and anisotropic media: Boundary element modeling: Geophysics, **60**, No. 3.

Hauge, P., 1981, Measurements of attenuation from vertical seismic profiles: Geophysics, **46**, 1548-1558.

Kennett, B. L. N, 1983, Seismic wave propagation in stratified media: Cambridge University Press, New York.

Kjartansson, E., 1979, Constant *Q* Ð wave propagation and attenuation: J. Geophys. Res., **84**, 4137Ð4748.

Johnston, D. H., 1981, Attenuation: A state-of-art summary: Seismic Wave Attenuation, Edited by M. N. and D. H. Johnston, Geophysics reprint series, No. 2.

Luco, J. E. and Apsel, R. J., 1983, On the Green's function for a layered half-space, Part I: Bull. Seism. Soc. Am., **73**, 909-929.

Medlin, W. L., Schmitt, D. P., 1992, Acoustic logging based on wellbore resonance: SPE 24686, the 67th Annual SPE Technical. Conference.

Narayana, P. A. and Ophir, J., 1983, A closed form for the measurement of attenuation in nonlinearly dispersive media: Ultrasonic Imaging, **5**, 17-21.

Paillet, L. and Cheng, C. H., 1991, *Acoustic Waves in Boreholes*: CRC Press, Inc.

Pai, D. M., Ahmad, J. and Kennedy W. D., 1993, Two-dimensional induction log modeling using a coupled-mode, multiple-reflection series method: Geophysics, **58**, No. 4, 466-474.

Parker, K., Lerner, R. & Waag, R., 1988, Comparison of techniques for *in vivo* attenuation measurements: IEEE Transactions on Biomedical engineering, **35,** No. 12, 1064-1067.

Quan, Y, Harris, J. M. & Chen, X. F., 1994, Acoustic attenuation logs using center frequency shift method: 64th Ann. Internat. Mtg., Soc. Expl. Geophys., Expanded Abstracts, 8-11.

Quan, Y. and Harris, J. M., 1993, Seismic attenuation tomography based on centroid frequency shift: Expanded Abstracts of the 63rd SEG annual meeting.

Randall, C. J., Scheibner, D. J. and Wu, P. T., 1991, Multipole borehole acoustic waveform synthetic logs with beds and borehole washouts: Geophysics, **56**, 1757-1769.
Roever, W. L., Rosenbaum, J. H., and Vining, T. F., 1974, Acoustic waves from an impulsive source in a fluid-filled borehole: J. Acoust. Soc. Am., **55**, 1144-1157.

Schmitt, D. P. and Bouchon, 1985, Full wave acoustic logging: synthetic microseismograms and frequency-wavenumber analysis: Geophysics **50**, No. 11, 1756-1778.

Stephen, T. A., Cardo-Casas, F., and Cheng, C. H., 1985, Finite difference synthetic acoustic lo : Geophysics, **50**, 1588Ð16o., Ed., 1981, Seismic Wave Attenuation: Geophysics reprint series, No 2.

Tsang, L. and Rader, D., 1979, Numerical evaluation of the transient acoustic waveform due to a point source in a fluid-filled borehole: Geophysics, **44**, No. 10, 1706-1720.

Tubman, K. M., Cheng, C. H. and, M. N., 1984, Synthetic full waveform acoustic logs in cased boreholes: Geophysics, **49**, 1051-1059.

White, J., E., 1962, Elastic waves along a cylindrical bore,: Geophysics, **27**, 372.

Winbow, G. A., 1980, How to separate compressional and shear arrivals in a sonic log: 50th Ann. Internat. Mtg., Soc. Expl. Geophys., Expanded Abstracts, 16-20.

Yao, Z. and Zheng, T., 1985, The generalized reflection-transmission coefficient method in acoustic well logging, Acta Geophysics Sinica (in Chinese), **28**, 510-518.

Zucca, J. J., Hutchings, L. J. and Kasameyer, P. W., 1994, Seismic velocity and attenuation structure of the Geysers geothermal field, California: Geothermics, **23**, 111-126.

Appendix A

A-1 *S* WAVE POTENTIAL IN RADIALLY SYMMETRIC MEDIA

The displacement vector $\mathbf{u}$ can be represented by the *P* wave potential ϕ and the *S* wave potential $\mathbf{\Psi}$:

$$\begin{aligned}\mathbf{u} &= \nabla\phi + \nabla\times\mathbf{\Psi} \\ &= \mathbf{e}_r[\frac{\partial\phi}{\partial r} - \frac{\partial\Psi_\theta}{\partial r}] + \mathbf{e}_\theta[\frac{\partial\Psi_r}{\partial z} - \frac{\partial\Psi_z}{\partial r}] + \mathbf{e}_z[\frac{\partial\phi}{\partial z} + \frac{1}{r}\frac{\partial}{\partial r}(r\Psi_\theta)] \ ,\end{aligned} \qquad \text{(A-1.1)}$$

where $\phi = \phi(r,z)$ and $\mathbf{\Psi} = \mathbf{\Psi}(r,z)$ are independent of θ . Since there is no *SH* wave, the displacement in $\mathbf{e}_\theta$ direction is zero. It can be seen from (A-1.1) that displacements in $\mathbf{e}_r$ and $\mathbf{e}_z$ directions are independent of Ψ_r and Ψ_z in this radially symmetric case. Therefore, we may choose $\Psi_r = \Psi_z = 0$. letting $\Psi_\theta = \psi$, we can write the *S* wave potential as

$$\mathbf{\Psi} = \mathbf{e}_\theta\psi(r,z) . \qquad \text{(A-1.2)}$$

A-2 ELASTODYNAMIC EQUATION IN TERMS OF POTENTIALS

The elastodynamic equation for isotropic media is

$$\rho\ddot{\mathbf{u}}(\mathbf{x},t) = \mathbf{f} + (\lambda + 2\mu)\nabla\nabla\cdot\mathbf{u}(\mathbf{x},t) - \mu\nabla\times\nabla\times\mathbf{u}(\mathbf{x},t), \tag{2.1 again}$$

A point explosion source $\Phi(t)$ is located at r=0 and z=0, which satisfies

$$\mathbf{f} = -\nabla[\Phi(t)\frac{\delta(r)\delta(z)}{\pi r}], \tag{A-2.1}$$

where relationship $\delta(x)\delta(y)\delta(z) = \delta(r)\delta(z)/\pi r$ (Bracewell, 1986, Page 85) is used. The displacement $\mathbf{u}$ can be represented in terms of potentials, i.e.,

$$\mathbf{u}(r,z,t) = \nabla\phi + \nabla\times\mathbf{\Psi}, \tag{2.2 again}$$

where ϕ and $\mathbf{\Psi}$ are P wave and S wave potentials, respectively. Substituting equations (2.2) into the elastodynamic equation (2.1), we obtain

$$(\lambda + 2\mu)\nabla^2\phi - \rho\ddot{\phi} = \Phi\frac{\delta(r)\delta(z)}{\pi r}, \tag{A-2.2a}$$

$$\mu\nabla^2\mathbf{\Psi} - \rho\ddot{\mathbf{\Psi}} = 0. \tag{A-2.2b}$$

Here, vector identities:

$$\nabla^2\mathbf{\Psi} \equiv \nabla(\nabla\cdot\mathbf{\Psi}) - \nabla\times(\nabla\times\mathbf{\Psi}),$$

$$\nabla\cdot(\nabla\times\mathbf{\Psi}) \equiv \mathbf{0},$$

$$\nabla \times (\nabla \phi) \equiv \mathbf{0},$$

and condition

$$\nabla \cdot \boldsymbol{\Psi} = \mathbf{0}$$

are used. For a radially symmetrical problem, there are only *P* and *SV* waves, i.e., $\boldsymbol{\Psi} = \mathbf{e}_{\theta} \psi(r, z)$ (see Appendix A-1). Using the expression of differential operator ∇^2 for a vector:

$$(\nabla^2 \boldsymbol{\Psi})_{\theta} = \nabla^2 \psi - \frac{1}{r^2} \psi ,$$

we obtain equation (2.3):

$$(\lambda + 2\mu)\nabla^2 \phi - \rho \ddot{\phi} = \Phi \frac{\delta(r)\delta(z)}{\pi r},$$

$$\mu(\nabla^2 \psi - \frac{\psi}{r^2}) - \rho \ddot{\psi} = 0 .$$

A-3 GENERAL SOLUTION IN A FLUID-FILLED BOREHOLE

In a fluid-filled borehole with a point source at *r*=0, *z*=0, there is only *P* wave. The *P* wave potential $\tilde{\phi}^{(1)}(r)$ satisfies

$$\nabla^2 \tilde{\phi}^{(1)} + \nu_{\alpha}^{(1)2} \tilde{\phi}^{(1)} = F(\omega) \frac{\delta(r)}{\rho \pi r} \qquad \text{(A-3.1)}$$

where $\nu_{\alpha}^{(1)2} = \omega^2 / \alpha^{(1)2} - k^2$. The formal solution of equation (A-3.1) is

$$\hat{\phi}^{(1)}(r, k, \omega) = cJ_o(\nu_\alpha^{(1)} r) + s_+ H_o^{(1)}(\nu_\alpha^{(1)} r) \qquad \text{(A-3.2)}$$

The first term $cJ_o(\nu_\alpha^{(1)} r)$ represents the incoming wave. Constant c is determined by the boundary conditions. Everywhere within the borehole $\nabla^2 J_o + \nu_\alpha^{(1)2} J_o = 0$, even at r=0, since $J_o(0) = 1$, The second term $s_+ H_o^{(1)}(\nu_\alpha^{(1)} r)$ is outgoing wave generated by the point source. It remains to determine the constant s_+. Substituting (A-3.2) and integrating both sides over a small area $\pi\varepsilon^2$, we have

$$s_+ \int_0^{2\pi} \int_0^{\varepsilon} (\nabla^2 H_0^{(1)} + \nu_\alpha^{(1)2} H_0^{(1)}) r d\theta dr = F(\omega)\frac{1}{\rho}. \qquad \text{(A-3.3)}$$

Since

$$H_o^{(1)}(x) \approx i\frac{2}{\pi}\ln\frac{x}{2} \qquad \text{for } x \to 0,$$

integrating equation (A-3.3) gives

$$4 s_+ i = F(\omega)\frac{1}{\rho} \qquad \text{for } \varepsilon \to 0, \qquad \text{(A-3.4)}$$

where Green's Theorem

$$\int_S (u\nabla^2 G - G\nabla^2 u)\, dS = \oint_L \left(u\frac{\partial G}{\partial n} - G\frac{\partial u}{\partial n}\right) dL \qquad \text{(A-3.5)}$$

with $u = 1$ is used. From (A-3.4) we obtain

$$s_{+} = -F(\omega)\frac{i}{4\rho}\,. \qquad \text{(A-3.6)}$$

A-4 EXPLICIT EXPRESSIONS OF ELEMENTS $\boxed{\{e_{nm}^{(j)}\}}$

For $j > 1$ the explicit expressions of elements $\{e_{nm}^{(j)}\}$ defined in equation (8a) are

$$e_{11}^{(j)} = -\nu_{\alpha}^{(j)}\overline{H}_{1}^{(2)}(\nu_{\alpha}^{(j)}r)e^{i\nu_{\alpha}^{(j)}(r^{(j)}-r)},$$

$$e_{12}^{(j)} = -ik\overline{H}_{1}^{(2)}(\nu_{\beta}^{(j)}r)e^{i\nu_{\beta}^{(j)}(r^{(j)}-r)},$$

$$e_{13}^{(j)} = -\nu_{\alpha}^{(j)}\overline{H}_{1}^{(1)}(\nu_{\alpha}^{(j)}r)e^{i\nu_{\alpha}^{(j)}(r-r^{(j-1)})},$$

$$e_{14}^{(j)} = -ik\overline{H}_{1}^{(1)}(\nu_{\beta}^{(j)}r)e^{i\nu_{\beta}^{(j)}(r-r^{(j-1)})},$$

$$e_{21}^{(j)} = ik\overline{H}_{o}^{(2)}(\nu_{\alpha}^{(j)}r)e^{i\nu_{\alpha}^{(j)}(r^{(j)}-r)},$$

$$e_{22}^{(j)} = \nu_{\beta}^{(j)}\overline{H}_{o}^{(2)}(\nu_{\beta}^{(j)}r)e^{i\nu_{\beta}^{(j)}(r^{(j)}-r)},$$

$$e_{23}^{(j)} = ik\overline{H}_{o}^{(1)}(\nu_{\alpha}^{(j)}r)e^{i\nu_{\alpha}^{(j)}(r-r^{(j-1)})},$$

$$e_{24}^{(j)} = \nu_{\beta}^{(j)}\overline{H}_{o}^{(1)}(\nu_{\beta}^{(j)}r)e^{i\nu_{\beta}^{(j)}(r-r^{(j-1)})},$$

$$e_{31}^{(j)} = 2\mu^{(j)}[\Omega^{(j)}\overline{H}_{o}^{(2)}(\nu_{\alpha}^{(j)}r) + \nu_{\alpha}^{(j)}\overline{H}_{1}^{(2)}(\nu_{\alpha}^{(j)}r)/r]e^{i\nu_{\alpha}^{(j)}(r^{(j)}-r)},$$

$$e_{32}^{(j)} = -ik\mu^{(j)}\nu_{\beta}^{(j)}[\overline{H}_{o}^{(2)}(\nu_{\beta}^{(j)}r) - \overline{H}_{2}^{(2)}(\nu_{\beta}^{(j)}r)]e^{i\nu_{\beta}^{(j)}(r^{(j)}-r)},$$

$$e_{33}^{(j)} = 2\mu^{(j)}[\Omega^{(j)}\overline{H}_{o}^{(1)}(\nu_{\alpha}^{(j)}r) + \nu_{\alpha}^{(j)}\overline{H}_{1}^{(1)}(\nu_{\alpha}^{(j)}r)/r]e^{i\nu_{\alpha}^{(j)}(r-r^{(j-1)})},$$

$$e_{34}^{(j)} = -ik\mu^{(j)}\nu_{\beta}^{(j)}[\overline{H}_{o}^{(1)}(\nu_{\beta}^{(j)}r) - \overline{H}_{2}^{(1)}(\nu_{\beta}^{(j)}r)]e^{i\nu_{\beta}^{(j)}(r-r^{(j-1)})},$$

$$e_{41}^{(j)} = -2ik\mu^{(j)}\nu_{\alpha}^{(j)}\overline{H}_{1}^{(2)}(\nu_{\alpha}^{(j)}r)e^{i\nu_{\alpha}^{(j)}(r^{(j)}-r)},$$

$$e_{42}^{(j)} = 2\mu^{(j)}\Omega^{(j)}\overline{H}_{1}^{(2)}(\nu_{\beta}^{(j)}r)e^{i\nu_{\beta}^{(j)}(r^{(j)}-r)},$$

$$e_{43}^{(j)} = -2ik\mu^{(j)}\nu_{\alpha}^{(j)}\overline{H}_{1}^{(1)}(\nu_{\alpha}^{(j)}r)e^{i\nu_{\alpha}^{(j)}(r-r^{(j-1)})},$$

$$e_{44}^{(j)} = 2\mu^{(j)}\Omega^{(j)}\overline{H}_{1}^{(1)}(\nu_{\beta}^{(j)}r)e^{i\nu_{\beta}^{(j)}(r-r^{(j-1)})},$$

where, $\Omega^{(j)} = k^{2} - \frac{1}{2}k_{\beta}^{(j)^{2}}$ and $r^{(j-1)} < r < r^{(j)}$.

For *j*=1, the expressions of elements $\{e_{nm}^{(j)}\}$ defined in equation (8b) are

$$e_{11}^{(1)} = -\nu_{\alpha}^{(1)}\overline{H}_{1}^{(2)}(\nu_{\alpha}^{(1)}r)e^{i\nu_{\alpha}^{(1)}(r^{(1)}-r)},$$

$$e_{12}^{(1)} = -\nu_{\alpha}^{(1)}\overline{H}_{1}^{(1)}(\nu_{\alpha}^{(1)}r)e^{i\nu_{\alpha}^{(1)}r},$$

$$e_{21}^{(1)} = -\lambda^{(1)} k_{\alpha}^{(1)^2} \overline{H}_0^{(2)}(\nu_{\alpha}^{(1)} r) e^{i\nu_{\alpha}^{(1)}(r^{(1)} - r)},$$

$$e_{22}^{(1)} = -\lambda^{(1)} k_{\alpha}^{(1)^2} \overline{H}_0^{(1)}(\nu_{\alpha}^{(1)} r) e^{i\nu_{\alpha}^{(1)} r}.$$

A-5 DERIVATION OF THE MODIFIED R/T MATRIX

Let us define

$$\mathbf{E}_{11}^{(j)}(r) = \begin{bmatrix} e_{11}^{(j)}(r) & e_{12}^{(j)}(r) \\ e_{21}^{(j)}(r) & e_{22}^{(j)}(r) \end{bmatrix},$$

$$\mathbf{E}_{12}^{(j)}(r) = \begin{bmatrix} e_{13}^{(j)}(r) & e_{14}^{(j)}(r) \\ e_{23}^{(j)}(r) & e_{24}^{(j)}(r) \end{bmatrix},$$

$$\mathbf{E}_{21}^{(j)}(r) = \begin{bmatrix} e_{31}^{(j)}(r) & e_{32}^{(j)}(r) \\ e_{41}^{(j)}(r) & e_{42}^{(j)}(r) \end{bmatrix},$$

$$\mathbf{E}_{22}^{(j)}(r) = \begin{bmatrix} e_{33}^{(j)}(r) & e_{34}^{(j)}(r) \\ e_{43}^{(j)}(r) & e_{44}^{(j)}(r) \end{bmatrix}.$$

and

$$\mathbf{c}_{\pm}^{(j)} = \begin{bmatrix} c_{p\pm}^{(j)} \\ c_{s\pm}^{(j)} \end{bmatrix}.$$

Then, the boundary conditions, equation (2.11), can be rewritten as

$$\begin{aligned}
\mathbf{E}_{11}^{(j)}(r^{(j)})\,\mathbf{c}_{-}^{(j)} + \mathbf{E}_{12}^{(j)}(r^{(j)})\mathbf{c}_{+}^{(j)} &= \mathbf{E}_{11}^{(j+1)}(r^{(j)})\mathbf{c}_{-}^{(j+1)} + \mathbf{E}_{12}^{(j+1)}(r^{(j)})\mathbf{c}_{+}^{(j+1)} \\
\mathbf{E}_{21}^{(j)}(r^{(j)})\,\mathbf{c}_{-}^{(j)} + \mathbf{E}_{22}^{(j)}(r^{(j)})\mathbf{c}_{+}^{(j)} &= \mathbf{E}_{21}^{(j+1)}(r^{(j)})\,\mathbf{c}_{-}^{(j+1)} + \mathbf{E}_{22}^{(j+1)}(r^{(j)})\mathbf{c}_{+}^{(j+1)}
\end{aligned}. \tag{A-5.1}$$

Rearranging the left side and right side of equation (A-5.1), we have

$$\begin{bmatrix} \mathbf{E}_{11}^{(j)}(r^{(j)}) & -\mathbf{E}_{12}^{(j+1)}(r^{(j)}) \\ \mathbf{E}_{21}^{(j)}(r^{(j)}) & -\mathbf{E}_{22}^{(j+1)}(r^{(j)}) \end{bmatrix} \begin{bmatrix} \mathbf{c}_{-}^{(j)} \\ \mathbf{c}_{+}^{(j+1)} \end{bmatrix} = \begin{bmatrix} -\mathbf{E}_{12}^{(j+1)}(r^{(j)}) & \mathbf{E}_{11}^{(j)}(r^{(j)}) \\ -\mathbf{E}_{22}^{(j+1)}(r^{(j)}) & \mathbf{E}_{21}^{(j)}(r^{(j)}) \end{bmatrix} \begin{bmatrix} \mathbf{c}_{+}^{(j)} \\ \mathbf{c}_{-}^{(j+1)} \end{bmatrix} \tag{A-5.2}$$

or rewrite it as

$$\begin{bmatrix} \mathbf{c}_{-}^{(j)} \\ \mathbf{c}_{+}^{(j+1)} \end{bmatrix} = \begin{bmatrix} \mathbf{E}_{11}^{(j)}(r^{(j)}) & -\mathbf{E}_{12}^{(j+1)}(r^{(j)}) \\ \mathbf{E}_{21}^{(j)}(r^{(j)}) & -\mathbf{E}_{22}^{(j+1)}(r^{(j)}) \end{bmatrix}^{-1} \begin{bmatrix} -\mathbf{E}_{12}^{(j+1)}(r^{(j)}) & \mathbf{E}_{11}^{(j)}(r^{(j)}) \\ -\mathbf{E}_{22}^{(j+1)}(r^{(j)}) & \mathbf{E}_{21}^{(j)}(r^{(j)}) \end{bmatrix} \begin{bmatrix} \mathbf{c}_{+}^{(j)} \\ \mathbf{c}_{-}^{(j+1)} \end{bmatrix}. \tag{A-5.3}$$

Comparing (A-5.3) with equation (2.12a) (the definition of modified R/T matrix):

$$\begin{bmatrix} \mathbf{c}_{-}^{(j)} \\ \mathbf{c}_{+}^{(j+1)} \end{bmatrix} = \begin{bmatrix} \mathbf{R}_{+-}^{(j)} & \mathbf{T}_{-}^{(j)} \\ \mathbf{T}_{+}^{(j)} & \mathbf{R}_{-+}^{(j)} \end{bmatrix} \begin{bmatrix} \mathbf{c}_{+}^{(j)} \\ \mathbf{c}_{-}^{(j+1)} \end{bmatrix},$$

we obtain

$$\begin{bmatrix} \mathbf{R}_{+-}^{(j)} & \mathbf{T}_{-}^{(j)} \\ \mathbf{T}_{+}^{(j)} & \mathbf{R}_{-+}^{(j)} \end{bmatrix} = \begin{bmatrix} \mathbf{E}_{11}^{(j)}(r^{(j)}) & -\mathbf{E}_{12}^{(j+1)}(r^{(j)}) \\ \mathbf{E}_{21}^{(j)}(r^{(j)}) & -\mathbf{E}_{22}^{(j+1)}(r^{(j)}) \end{bmatrix}^{-1} \begin{bmatrix} -\mathbf{E}_{12}^{(j+1)}(r^{(j)}) & \mathbf{E}_{11}^{(j)}(r^{(j)}) \\ -\mathbf{E}_{22}^{(j+1)}(r^{(j)}) & \mathbf{E}_{21}^{(j)}(r^{(j)}) \end{bmatrix}. \tag{A-5.4}$$

A-6 DERIVATION OF THE GENERALIZED R/T MATRICES

Substituting equation (2.15):

$$\begin{cases} \mathbf{c}_{+}^{(j+1)} = \overset{?}{\mathbf{T}}{}_{+}^{(j)}\mathbf{c}_{+}^{(j)} \\ \mathbf{c}_{-}^{(j)} = \overset{?}{\mathbf{R}}{}_{+-}^{(j)}\mathbf{c}_{+}^{(j)} \end{cases}$$

into equation (2.12):

$$\begin{cases} \mathbf{c}_{-}^{(j)} = \mathbf{R}_{+-}^{(j)}\mathbf{c}_{+}^{(j)} + \mathbf{T}_{-}^{(j)}\mathbf{c}_{-}^{(j+1)} \\ \mathbf{c}_{+}^{(j+1)} = \mathbf{T}_{+}^{(j)}\mathbf{c}_{+}^{(j)} + \mathbf{R}_{-+}^{(j)}\mathbf{c}_{-}^{(j+1)} \end{cases},$$

we obtain

$$\begin{cases} \mathbf{c}_{-}^{(j)} = \mathbf{R}_{+-}^{(j)}\mathbf{c}_{+}^{(j)} + \mathbf{T}_{-}^{(j)}\overset{?}{\mathbf{R}}{}_{+-}^{(j+1)}\mathbf{c}_{+}^{(j+1)} \\ \mathbf{c}_{+}^{(j+1)} = \mathbf{T}_{+}^{(j)}\mathbf{c}_{+}^{(j)} + \mathbf{R}_{-+}^{(j)}\overset{?}{\mathbf{R}}{}_{+-}^{(j+1)}\mathbf{c}_{+}^{(j+1)} \end{cases}. \tag{A-6.1}$$

Substituting the first equation in (2.15) into the second equation in (A-6.1) and rearranging it as

$$\begin{cases} \mathbf{c}_{+}^{(j+1)} = [\mathbf{I} - \mathbf{R}_{-+}^{(j)}\overset{?}{\mathbf{R}}{}_{+-}^{(j+1)}]^{-1}\mathbf{T}_{+}^{(j)}\mathbf{c}_{+}^{(j)} \\ \mathbf{c}_{-}^{(j)} = (\mathbf{R}_{+-}^{(j)} + \mathbf{T}_{-}^{(j)}\overset{?}{\mathbf{R}}{}_{+-}^{(j+1)}\overset{?}{\mathbf{T}}{}_{+}^{(j)})\mathbf{c}_{+}^{(j)} \end{cases}. \tag{A-6.2}$$

Comparing equation (A-6.2) with equation (2.15), we obtain

$$\begin{cases} \overset{?}{\mathbf{T}}{}_{+}^{(j)} = [\mathbf{I} - \mathbf{R}_{-+}^{(j)}\overset{?}{\mathbf{R}}{}_{+-}^{(j+1)}]^{-1}\mathbf{T}_{+}^{(j)} \\ \overset{?}{\mathbf{R}}{}_{+-}^{(j)} = \mathbf{R}_{+-}^{(j)} + \mathbf{T}_{-}^{(j)}\overset{?}{\mathbf{R}}{}_{+-}^{(j+1)}\overset{?}{\mathbf{T}}{}_{+}^{(j)} \end{cases}. \tag{2.16 again}$$

Appendix B

B-1 EXPLICIT EXPRESSIONS OF COEFFICIENT MATRICES

For j>1 the elements E_{pq} in equation (3.9) are:

$$E_{11}^{(j)}(r;l,n) = -\gamma_n^{(j)} H_1^{(2)}(\gamma_n^{(j)} r) a_p^{(j)}(l,n),$$

$$E_{12}^{(j)}(r;l,n) = -ik_l H_1^{(2)}(\nu_n^{(j)} r) a_s^{(j)}(l,n),$$

$$E_{13}^{(j)}(r;l,n) = -\gamma_n^{(j)} H_1^{(1)}(\gamma_n^{(j)} r) a_p^{(j)}(l,n),$$

$$E_{14}^{(j)}(r;l,n) = -ik_l H_1^{(1)}(\nu_n^{(j)} r) a_s^{(j)}(l,n),$$

$$E_{21}^{(j)}(r;l,n) = ik_l H_o^{(2)}(\gamma_n^{(j)} r) a_p^{(j)}(l,n),$$

$$E_{22}^{(j)}(r;l,n) = \nu_n^{(j)} H_o^{(2)}(\nu_n^{(j)} r) a_s^{(j)}(l,n),$$

$$E_{23}^{(j)}(r;l,n) = ik_l H_o^{(1)}(\gamma_n^{(j)} r) a_p^{(j)}(l,n),$$

$$E_{22}^{(j)}(r;l,n) = \nu_n^{(j)} H_o^{(1)}(\nu_n^{(j)} r) a_s^{(j)}(l,n),$$

$$E_{31}^{(j)}(r;l,n) = \sum_{m=1}^{2N+1} \{[2k_m^2 H_o^{(2)}(\gamma_n^{(j)} r) + \frac{2\gamma_n^{(j)}}{r} H_1^{(2)}(\gamma_n^{(j)} r)]\mu_{lm}^{(j)} a_p^{(j)}(m,,n)] \\ - \omega^2 H_o^{(2)}(\gamma_n^{(j)} r)\rho_{lm}^{(j)} a_p^{(j)}(m,n)\},$$

$$E_{32}^{(j)}(r;l,n) = \sum_{m=1}^{2N+1} [-i2k_m \nu_n^{(j)} \overset{?}{H}_1^{(2)}(\nu_n^{(j)} r)\mu_{lm}^{(j)} a_s^{(j)}(m,n)],$$

$$E_{33}^{(j)}(r;l,n) = \sum_{m=1}^{2N+1} \{[2k_m^2 H_o^{(1)}(\gamma_n^{(j)} r) + \frac{2\gamma_n^{(j)}}{r} H_1^{(2)}(\gamma_n^{(j)} r)]\mu_{lm}^{(j)} a_p^{(j)}(m,,n)] \\ - \omega^2 H_o^{(1)}(\gamma_n^{(j)} r)\rho_{lm}^{(j)} a_p^{(j)}(m,n)\},$$

$$E_{34}^{(j)}(r;l,n) = \sum_{m=1}^{2N+1} [-i2k_m \nu_n^{(j)} \overset{?}{H}_1^{(1)}(\nu_n^{(j)} r)\mu_{lm}^{(j)} a_s^{(j)}(m,n)],$$

$$E_{41}^{(j)}(r;l,n) = \sum_{m=1}^{2N+1} [-i2k_m \gamma_n^{(j)} H_1^{(2)}(\gamma_n^{(j)} r)\mu_{lm}^{(j)} a_p^{(j)}(m,n)],$$

$$E_{42}^{(j)}(r;l,n) = \sum_{m=1}^{2N+1} [2k_m^2 \mu_{lm}^{(j)} - \omega^2 \rho_{lm}^{(j)}] H_1^{(2)}(\nu_n^{(j)} r) a_s^{(j)}(m,n),$$

$$E_{43}^{(j)}(r;l,n) = \sum_{m=1}^{2N+1} [-i2k_m \gamma_n^{(j)} H_1^{(1)}(\gamma_n^{(j)} r)\mu_{lm}^{(j)} a_p^{(j)}(m,n)],$$

$$E_{44}^{(j)}(r;l,n) = \sum_{m=1}^{2N+1} [2k_m^2 \mu_{lm}^{(j)} - \omega^2 \rho_{lm}^{(j)}] H_1^{(1)}(\nu_n^{(j)} r) a_s^{(j)}(m,n),$$

where $\mu_{lm}^{(j)} = \int_{-L/2}^{+L/2} \mu^{(j)}(z) \exp[i(k_l - k_m)z]dz$.

For *j*=1 the elements E_{pq} in equation (3.10) are:

$$E_{11}^{(1)}(r;l,n) = -\gamma_n^{(1)} H_1^{(2)}(\gamma_n^{(1)} r)\, a_p^{(1)}(l,n),$$

$$E_{12}^{(1)}(r;l,n) = -\gamma_n^{(1)} H_1^{(1)}(\gamma_n^{(1)} r)\, a_p^{(1)}(l,n)\ ,$$

$$E_{21}^{(1)}(r;l,n) = ik_l H_o^{(2)}(\gamma_n^{(1)} r)\, a_p^{(1)}(l,n),$$

$$E_{22}^{(j)}(r;l,n) = ik_l H_o^{(1)}(\gamma_n^{(j)} r)\, a_p^{(j)}(l,n)\ ,$$

$$E_{31}^{(1)}(r;l,n) = -\lambda^{(1)}(k_\alpha^{(1)})^2 H_o^{(2)}(\gamma_n^{(1)} r)\, a_p^{(1)}(l,n),$$

$$E_{32}^{(1)}(r;l,n) = -\lambda^{(1)}(k_\alpha^{(1)})^2 H_o^{(1)}(\gamma_n^{(1)} r)\, a_p^{(1)}(l,n).$$

B-2 DERIVATION OF THE MODIFIED R/T MATRICES

The boundary conditions, equation (3.13), can be rewritten as

$$\begin{array}{l} \mathbf{D}_{11}^{(j)}(r^{(j)})\ \mathbf{c}_-^{(j)} + \mathbf{D}_{12}^{(j)}(r^{(j)})\mathbf{C}_+^{(j)} = \mathbf{D}_{11}^{(j+1)}(r^{(j)})\mathbf{C}_-^{(j+1)} + \mathbf{D}_{12}^{(j+1)}(r^{(j)})\mathbf{C}_+^{(j+1)} \\ \mathbf{D}_{21}^{(j)}(r^{(j)})\ \mathbf{c}_-^{(j)} + \mathbf{D}_{22}^{(j)}(r^{(j)})\mathbf{C}_+^{(j)} = \mathbf{D}_{21}^{(j+1)}(r^{(j)})\ \mathbf{C}_-^{(j+1)} + \mathbf{D}_{22}^{(j+1)}(r^{(j)})\mathbf{C}_+^{(j+1)} \end{array}. \quad \text{(B-2.1)}$$

Rearranging the left side and right side of equation (B-2.1), we have

$$\begin{array}{l} \mathbf{D}_{11}^{(j)}(r^{(j)})\ \mathbf{c}_-^{(j)} - \mathbf{D}_{12}^{(j+1)}(r^{(j)})\mathbf{C}_+^{(j+1)} = -\mathbf{D}_{12}^{(j)}(r^{(j)})\mathbf{C}_+^{(j)} + \mathbf{D}_{11}^{(j+1)}(r^{(j)})\mathbf{C}_-^{(j+1)} \\ \mathbf{D}_{21}^{(j)}(r^{(j)})\ \mathbf{c}_-^{(j)} - \mathbf{D}_{22}^{(j+1)}(r^{(j)})\mathbf{C}_+^{(j+1)} = -\mathbf{D}_{22}^{(j)}(r^{(j)})\mathbf{C}_+^{(j)} + \mathbf{D}_{21}^{(j+1)}(r^{(j)})\ \mathbf{C}_-^{(j+1)} \end{array}. \quad \text{(B-2.2)}$$

or rewrite it as

$$\begin{bmatrix} \mathbf{D}_{11}^{(j)}(r^{(j)}) & -\mathbf{D}_{12}^{(j+1)}(r^{(j)}) \\ \mathbf{D}_{21}^{(j)}(r^{(j)}) & -\mathbf{D}_{22}^{(j+1)}(r^{(j)}) \end{bmatrix} \begin{bmatrix} \mathbf{C}_{-}^{(j)} \\ \mathbf{C}_{+}^{(j+1)} \end{bmatrix} = \begin{bmatrix} -\mathbf{D}_{12}^{(j+1)}(r^{(j)}) & \mathbf{D}_{11}^{(j)}(r^{(j)}) \\ -\mathbf{D}_{22}^{(j+1)}(r^{(j)}) & \mathbf{D}_{21}^{(j)}(r^{(j)}) \end{bmatrix} \begin{bmatrix} \mathbf{C}_{+}^{(j)} \\ \mathbf{C}_{-}^{(j+1)} \end{bmatrix}. \quad \text{(B-2.3)}$$

Multiplying $\begin{bmatrix} \mathbf{D}_{11}^{(j)}(r^{(j)}) & -\mathbf{D}_{12}^{(j+1)}(r^{(j)}) \\ \mathbf{D}_{21}^{(j)}(r^{(j)}) & -\mathbf{D}_{22}^{(j+1)}(r^{(j)}) \end{bmatrix}^{-1}$ on both sizes of (B-2.3), we obtain

$$\begin{bmatrix} \mathbf{C}_{-}^{(j)} \\ \mathbf{C}_{+}^{(j+1)} \end{bmatrix} = \begin{bmatrix} \mathbf{D}_{11}^{(j)}(r^{(j)}) & -\mathbf{D}_{12}^{(j+1)}(r^{(j)}) \\ \mathbf{D}_{21}^{(j)}(r^{(j)}) & -\mathbf{D}_{22}^{(j+1)}(r^{(j)}) \end{bmatrix}^{-1} \begin{bmatrix} -\mathbf{D}_{12}^{(j+1)}(r^{(j)}) & \mathbf{D}_{11}^{(j)}(r^{(j)}) \\ -\mathbf{D}_{22}^{(j+1)}(r^{(j)}) & \mathbf{D}_{21}^{(j)}(r^{(j)}) \end{bmatrix} \begin{bmatrix} \mathbf{C}_{+}^{(j)} \\ \mathbf{C}_{-}^{(j+1)} \end{bmatrix}. \qquad \text{(B-2.4)}$$

Comparing (B-2.4) with equation (3.11a) (the definition of modified R/T matrix):

$$\begin{bmatrix} \mathbf{C}_{-}^{(j)} \\ \mathbf{C}_{+}^{(j+1)} \end{bmatrix} = \begin{bmatrix} \mathbf{R}_{+-}^{(j)} & \mathbf{T}_{-}^{(j)} \\ \mathbf{T}_{+}^{(j)} & \mathbf{R}_{-+}^{(j)} \end{bmatrix} \begin{bmatrix} \mathbf{C}_{+}^{(j)} \\ \mathbf{C}_{-}^{(j+1)} \end{bmatrix},$$

we finally obtain equation (3.14)

$$\begin{bmatrix} \mathbf{R}_{+-}^{(j)} & \mathbf{T}_{-}^{(j)} \\ \mathbf{T}_{+}^{(j)} & \mathbf{R}_{-+}^{(j)} \end{bmatrix} = \begin{bmatrix} \mathbf{D}_{11}^{(j)}(r^{(j)}) & -\mathbf{D}_{12}^{(j+1)}(r^{(j)}) \\ \mathbf{D}_{21}^{(j)}(r^{(j)}) & -\mathbf{D}_{22}^{(j+1)}(r^{(j)}) \end{bmatrix}^{-1} \begin{bmatrix} -\mathbf{D}_{12}^{(j+1)}(r^{(j)}) & \mathbf{D}_{11}^{(j)}(r^{(j)}) \\ -\mathbf{D}_{22}^{(j+1)}(r^{(j)}) & \mathbf{D}_{21}^{(j)}(r^{(j)}) \end{bmatrix}.$$

$$= \begin{bmatrix} \mathbf{E}_{11}^{(j)} & \mathbf{E}_{12}^{(j)} & -\mathbf{E}_{13}^{(j+1)} & -\mathbf{E}_{14}^{(j+1)} \\ \mathbf{E}_{21}^{(j)} & \mathbf{E}_{22}^{(j)} & -\mathbf{E}_{23}^{(j+1)} & -\mathbf{E}_{24}^{(j+1)} \\ \mathbf{E}_{31}^{(j)} & \mathbf{E}_{32}^{(j)} & -\mathbf{E}_{33}^{(j+1)} & -\mathbf{E}_{34}^{(j+1)} \\ \mathbf{E}_{41}^{(j)} & \mathbf{E}_{42}^{(j)} & -\mathbf{E}_{43}^{(j+1)} & -\mathbf{E}_{44}^{(j+1)} \end{bmatrix}^{-1} \begin{bmatrix} -\mathbf{E}_{13}^{(j)} & -\mathbf{E}_{14}^{(j)} & \mathbf{E}_{11}^{(j+1)} & \mathbf{E}_{12}^{(j+1)} \\ -\mathbf{E}_{23}^{(j)} & -\mathbf{E}_{24}^{(j)} & \mathbf{E}_{21}^{(j+1)} & \mathbf{E}_{22}^{(j+1)} \\ -\mathbf{E}_{33}^{(j)} & -\mathbf{E}_{34}^{(j)} & \mathbf{E}_{31}^{(j+1)} & \mathbf{E}_{32}^{(j+1)} \\ -\mathbf{E}_{43}^{(j)} & -\mathbf{E}_{44}^{(j)} & \mathbf{E}_{41}^{(j+1)} & \mathbf{E}_{42}^{(j+1)} \end{bmatrix}_{r=r^{(j)}}$$

B-3 DERIVATION OF THE GENERALIZED R/T MATRIX

Substituting equation (3.17a):

$$\begin{cases} \mathbf{C}_{+}^{(j+1)} = \overset{?}{\mathbf{T}}{}_{+}^{(j)} \mathbf{C}_{+}^{(j)} \\ \mathbf{C}_{-}^{(j)} = \overset{?}{\mathbf{R}}{}_{+-}^{(j)} \mathbf{C}_{+}^{(j)} \end{cases}$$

into equation (3.11a):

$$\begin{cases} \mathbf{C}_{+}^{(j+1)} = \mathbf{T}_{+}^{(j)} \mathbf{C}_{+}^{(j)} + \mathbf{R}_{-+}^{(j)} \mathbf{C}_{-}^{(j+1)} \\ \mathbf{C}_{-}^{(j)} = \mathbf{R}_{+-}^{(j)} \mathbf{C}_{+}^{(j)} + \mathbf{T}_{-}^{(j)} \mathbf{C}_{-}^{(j+1)} \end{cases},$$

we obtain

$$\begin{cases} \mathbf{C}_{-}^{(j)} = \mathbf{R}_{+-}^{(j)} \mathbf{C}_{+}^{(j)} + \mathbf{T}_{-}^{(j)} \overset{?}{\mathbf{R}}{}_{+-}^{(j+1)} \mathbf{C}_{+}^{(j+1)} \\ \mathbf{C}_{+}^{(j+1)} = \mathbf{T}_{+}^{(j)} \mathbf{C}_{+}^{(j)} + \mathbf{R}_{-+}^{(j)} \overset{?}{\mathbf{R}}{}_{+-}^{(j+1)} \mathbf{C}_{+}^{(j+1)} \end{cases}. \tag{B-3.1}$$

Substituting the first equation in (2.17a) into the second equation in (B-3.1) and rearranging it as

$$\begin{cases} \mathbf{c}_{+}^{(j+1)} = [\mathbf{I} - \mathbf{R}_{-+}^{(j)} \overset{?}{\mathbf{R}}{}_{+-}^{(j+1)}]^{-1} \mathbf{T}_{+}^{(j)} \mathbf{c}_{+}^{(j)} \\ \mathbf{c}_{-}^{(j)} = (\mathbf{R}_{+-}^{(j)} + \mathbf{T}_{-}^{(j)} \overset{?}{\mathbf{R}}{}_{+-}^{(j+1)} \overset{?}{\mathbf{T}}{}_{+}^{(j)}) \mathbf{c}_{+}^{(j)} \end{cases}. \tag{B-3.2}$$

Comparing equation (B-3.2) with equation (2.17a), we obtain

$$\begin{cases} \overset{?}{\mathbf{T}}{}_{+}^{(j)} = [\mathbf{I} - \mathbf{R}_{-+}^{(j)} \overset{?}{\mathbf{R}}{}_{+-}^{(j+1)}]^{-1} \mathbf{T}_{+}^{(j)} \\ \overset{?}{\mathbf{R}}{}_{+-}^{(j)} = \mathbf{R}_{+-}^{(j)} + \mathbf{T}_{-}^{(j)} \overset{?}{\mathbf{R}}{}_{+-}^{(j+1)} \overset{?}{\mathbf{T}}{}_{+}^{(j)} \end{cases}. \tag{3.18 again}$$

Appendix C

Relationships between the Attenuation Coefficient and the Frequency Shift

C-1 GAUSSIAN SHAPE SPECTRUM

If the input amplitude spectrum *S(f)* is of Gaussian shape, i.e.,

$$S(f) = \exp\left[-\frac{(f-f_o)^2}{2\sigma_S^2}\right],$$

the centroid of *S(f)* is f_O. The output amplitude spectrum is

$$\begin{aligned} R(f) = S(f)\cdot H(f) &= \exp\left[-\frac{(f-f_o)^2}{2\sigma_S^2} - f\int_{ray}\alpha_o dl\right] \\ &= \exp\left[-\frac{f^2 - 2ff_R + f_R^2 + f_d}{2\sigma_S^2}\right] = A\cdot\exp\left[-\frac{(f-f_R)^2}{2\sigma_S^2}\right], \end{aligned}$$

where

$$f_R = (f_o - \sigma_S^2\int_{ray}\alpha_o dl),$$

$$f_d = 2 f_o \sigma_S^2 \int_{ray} \alpha_o dl - (\sigma_S^2 \int_{ray} \alpha_o dl)^2 ,$$

and

$$A = \exp [- \frac{f_d}{2 \sigma_S^2}] .$$

It can be seen that f_R is the centroid of *R(f)*, and *A* is the amplitude.

C-2 RECTANGULAR SHAPE SPECTRUM

If the spectrum *S(f)* is of rectangular shape with a width of *B*, then

$$f_S = \int_0^B f df \ / \ \int_0^B df = B / 2 ,$$

$$f_R = \frac{\int_0^B f e^{-fa_o L} df}{\int_0^B e^{-fa_o L} df} = \frac{a_o L}{1 - e^{-a_o LB}} [\frac{1}{(a_o L)^2} - \frac{Be^{-a_o LB}}{a_o L} (\frac{1}{a_o LB} + 1)] .$$

For simplicity, we write $\int_{ray} \alpha_o dl$ as $\alpha_o L$ for a homogeneous medium. If $\alpha_o LB << 1$, we have

$$\exp (- \alpha_o LB) \approx 1 - \alpha_o LB + \frac{1}{2} (\alpha_o LB)^2 - \frac{1}{6} (\alpha_o LB)^2$$

and

$$f_R \approx \frac{B}{2} - \frac{B^2}{12} \alpha_o L = f_S - \frac{B^2}{12} \alpha_o L ,$$

or write it as a tomographic equation

$$\int_{ray} a_o \, dl \approx 12\,(f_S - f_R)\,/\,B^2 .$$

C-3 TRIANGULAR SHAPE SPECTRUM

If *S(f)* is of right triangular shape with a side of *B* and $\alpha_o LB << 1$, we get

$$f_S = \frac{1}{3} B ,$$

$$f_R \approx \frac{B}{3} - \frac{B^2}{18} \alpha_o L = f_S - \frac{1}{18} \alpha_o L$$

and

$$\int_{ray} a_o \, dl \approx 18\,(f_S - f_R)\,/\,B^2 .$$